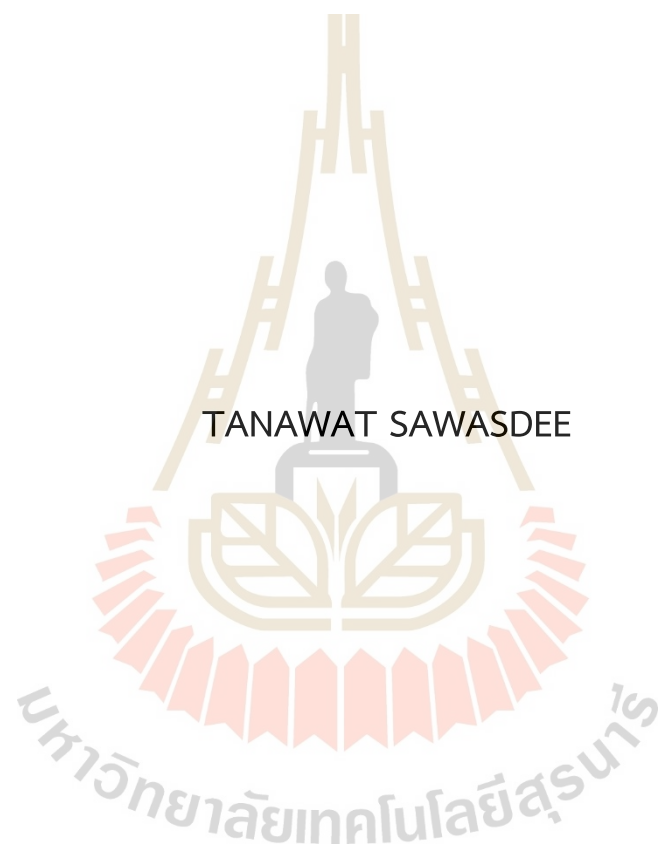


FIRST PRINCIPLES STUDY OF STRUCTURAL AND ELECTRONIC  
PROPERTIES, Li-ION MOBILITY AND METALS INTERCALATION OF  
TRANSITION METAL CARBIDES



A Thesis Submitted in Partial Fulfillment of the Requirements for the  
Degree of Doctor of Philosophy in Physics  
Suranaree University of Technology  
Academic Year 2021

การศึกษาคุณสมบัติเชิงโครงสร้างและอิเล็กทรอนิกส์ การเคลื่อนที่ของลิเธียม  
ไอออน และการแทรกชั้นด้วยโลหะในโลหะทรานซิชันคาร์ไบด์โดยวิธี  
เฟิร์สพริન્ซิเพิล



นายธนวัฏ สวัสดิ์

วิทยานิพนธ์นี้เป็นส่วนหนึ่งของการศึกษาตามหลักสูตรปริญญาวิทยาศาสตรดุษฎีบัณฑิต  
สาขาวิชาฟิสิกส์  
มหาวิทยาลัยเทคโนโลยีสุรนารี  
ปีการศึกษา 2564

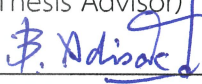
FIRST PRINCIPLES STUDY OF STRUCTURAL AND ELECTRONIC  
PROPERTIES, Li-ION MOBILITY AND METALS INTERCALATION OF  
TRANSITION METAL CARBIDES

Suranaree University of Technology has approved this thesis submitted in  
partial fulfillment of the requirements for the Degree of Doctor of Philosophy

Thesis Examining Committee

  
\_\_\_\_\_  
(Assoc. Prof. Dr. Panomsak Meemon)

Chairperson   
\_\_\_\_\_  
(Assoc. Prof. Dr. Sirichok Jungthawan)

Member (Thesis Advisor)   
\_\_\_\_\_  
(Assoc. Prof. Dr. Adisak Boonchun)

Member   
\_\_\_\_\_  
(Assoc. Prof. Dr. Pakpoom Reunchan)

Member   
\_\_\_\_\_  
(Asst. Prof. Dr. Suwit Suthirakun)

Member   
\_\_\_\_\_  
(Dr. Ittipon Fongkaew)

Member

  
\_\_\_\_\_  
(Assoc. Prof. Dr. Chatchai Jothityangkoon)  
Vice Rector for Academic Affairs  
and Quality Assurance

  
\_\_\_\_\_  
(Prof. Dr. Santi Maensiri)  
Dean of Institute of Science

ธนวิญ สุวดี : การศึกษาคุณสมบัติเชิงโครงสร้างและอิเล็กทรอนิกส์ การเคลื่อนที่ของลิเทียมไอออน และการแทรกชั้นด้วยโลหะในโลหะทรานซิชันคาร์ไบด์โดยวิธีเฟิร์สพริ้นซิเพิล (FIRST PRINCIPLES STUDY OF STRUCTURAL AND ELECTRONIC PROPERTIES, LI-ION MOBILITY AND METALS INTERCALATION OF TRANSITION METAL CARBIDES).  
อาจารย์ที่ปรึกษา : รองศาสตราจารย์ ดร.สิริโชค จิ่งถาวรรม, 165 หน้า

คำสำคัญ: วัสดุโครงสร้างสองมิติ, ลิเทียมไอออนแบตเตอรี่, โลหะทรานซิชันคาร์ไบด์

วิทยานิพนธ์นี้ศึกษาคุณสมบัติโครงสร้างของโลหะทรานซิชันคาร์ไบด์ (MXenes) เช่น  $M_2CT_2$  โดยที่  $M$  ประกอบด้วย Sc, Ti, V, Nb และ Cr และ  $T$  ประกอบด้วย O และ F โดยใช้วิธีการคำนวณแบบเฟิร์สพริ้นซิเพิล การศึกษานี้ให้ข้อมูลที่ครอบคลุมเกี่ยวกับคุณสมบัติเชิงโครงสร้างสำหรับโครงสร้างแบบเลเยอร์เดี่ยวและเลเยอร์คู่ของสารประกอบ  $M_2CT_2$  โดยจะเน้นไปที่คุณสมบัติทางอิเล็กทรอนิกส์ ความเสถียรของโครงสร้าง การแพร่กระจายและการเลือกของลิเทียมไอออน และการแพร่กระจายในโครงสร้างแบบชั้นคู่ร่วมกับการแทรกชั้นด้วยธาตุอื่น ๆ (co-intercalations) ในขั้นตอนแรกเราได้ศึกษาคุณสมบัติทางอิเล็กทรอนิกส์ของการปรับเปลี่ยนลักษณะโครงสร้างแบบชั้นเดี่ยวในวัสดุ  $M_2CT_2$  นอกจากนี้การเปลี่ยนแปลงของโครงสร้างที่เพิ่มเติมจากชั้นเดี่ยวอาจส่งผลต่อคุณสมบัติของ MXenes แบบหลายชั้น ซึ่งจากขั้นตอนนี้โครงสร้างที่มีความเสถียรสูงซึ่งได้มาจากการคำนวณพลังงานของระบบ เช่นสารประกอบ  $Ti_2CO_2$  ได้ถูกนำไปใช้เพื่อตรวจสอบเพิ่มเติมสำหรับการแพร่กระจายของลิเทียมอะตอมและการแทรกชั้นร่วมของโลหะอื่น ๆ ในการศึกษาเราใช้วิธี climbing image-nudged elastic band (CI-NEB) และ static potential energy (SPES) เพื่อทดสอบคุณสมบัติการแพร่กระจายของลิเทียมอะตอมในวัสดุ ซึ่งผลการคำนวณของการแพร่กระจายของธาตุลิเทียมในวัสดุ  $Ti_2CO_2$  แบบชั้นคู่มิค่าการขวางกั้นการแพร่ (diffusion barrier) ประมาณ 0.363 eV และพบว่ามีค่าต่ำมากที่ประมาณ 0.01 eV เมื่อระยะห่างระหว่างชั้น (interlayer spacing) มีค่าอยู่ในช่วงระหว่าง 3.40 Å และ 4.10 Å ซึ่งค่านี้มีความสัมพันธ์กับระยะห่างระหว่างชั้นของการแทรกชั้นร่วมกับโพแทสเซียมอะตอม โดยเราสามารถตีความได้ว่าที่ระยะห่างระหว่างชั้นที่มีค่าเหมาะสมค่าหนึ่ง ลิเทียมอะตอมจะถูกกละเลยจากแต่ละชั้นของ  $Ti_2CO_2$  นอกจากนี้ความรู้ที่จำเป็นสำหรับการทำความเข้าใจคุณลักษณะของลิเทียมไอออนแบตเตอรี่ในวัสดุ MXenes แบบชั้นคู่ จะถูกนำเสนอในลำดับสุดท้าย

สาขาวิชาฟิสิกส์  
ปีการศึกษา 2564

ลายมือชื่อนักศึกษา ธนวิญ สุวดี  
ลายมือชื่ออาจารย์ที่ปรึกษา สิริโชค จิ่งถาวรรม

TANAWAT SAWASDEE : FIRST PRINCIPLES STUDY OF STRUCTURAL AND ELECTRONIC PROPERTIES, Li-ION MOBILITY AND METALS INTERCALATION OF TRANSITION METAL CARBIDES. THESIS ADVISOR : ASSOC. PROF. SIRICHOK JUNGTHAWAN, Ph.D. 165 PP.

Keyword: 2D material, Li-ion battery, MXenes, Transition metal carbide

The properties of two-dimensional transition metal carbides (MXenes) of  $M_2CT_2$  (where  $M = \text{Sc, Ti, V, Nb, and Cr}$ ; and  $T = \text{O and F}$ ) have been studied utilizing first-principles calculations based on the density functional theory (DFT). Our calculation provides an extensive information of the structural properties of monolayer and bilayer  $M_2CT_2$  focusing characteristics, stability, diffusion and selectivity of Lithium-ion, and co-intercalation in bilayer  $M_2CT_2$ . The electronic properties of the distinct structural configurations of the monolayer  $M_2CT_2$  have been investigated. Altering the structural configurations in addition to the monolayer can affect the properties of the multilayer  $M_2CT_2$  MXenes. The energetically favorable monolayer and bilayer ( $\text{Ti}_2\text{CT}_2$  MXenes) have been further investigated for Li-ion diffusion and metal intercalations. The diffusion properties have been performed by using climbing image-nudged elastic band (CI-NEB) and static potential energy (SPES) methods. The Li-ion diffusion barrier for the intrinsic  $\text{Ti}_2\text{CO}_2$  bilayer is 0.363 eV and found to be significantly low ( $\sim 0.01$  eV) with interlayer spacings between 3.40 Å and 4.10 Å (corresponding to potassium co-intercalation). At a certain interlayer distance, Li atom is neglected by both  $\text{Ti}_2\text{CO}_2$  layers at the bilayer interface. The essential knowledge for comprehending the lithium-ion battery characteristics of the MXenes bilayer have been discussed.

School of Physics  
Academic Year 2021

Student's Signature \_\_\_\_\_  
Advisor's Signature \_\_\_\_\_

## ACKNOWLEDGEMENTS

Without the help and support of many people, I wouldn't be capable of completing my thesis. I would like to express my sincere gratitude to my supervisor, Assoc. Prof. Dr. Sirichok Jungthawan, for approving me for the research assistantship, his excellent scientific supervision, his essential assistance, educational direction, generosity, personal encouragement, and kind sympathy. He always inspires me to improve myself with his support and tolerance, as well as scientific concepts. Additionally, not just in terms of research procedures but also in aspects of many other life methodologies. Without his constant assistance, I would not have progressed as far as I have, and my thesis would not have been completed.

I would like to thank Assoc. Prof. Dr. Adisak Boonchun, Assoc. Prof. Dr. Pakpoom Reunchan, Asst. Prof. Dr. Panomsak Meemon and Asst. Prof. Dr. Suwit Suthirakun for serving as the thesis-examining committee. In addition, they took effort in reading and providing me with valuable comments.

I would like to thank to the Science Achievement Scholarship of Thailand (SAST, THAILAND) for providing me with a scholarship from undergrad to Doctoral degree. I would like to thank the Thailand Center of Excellence in Physics (ThEP) for financial support to our research group and I would like to thank Synchrotron Light Research Institute (Public Organization) for computation resources.

I would like to acknowledge with much appreciation the staffs at Suranaree University of Technology's School of Physics for their help and friendship, as well as my seniors in the condensed matter physics group, Dr. Ittipon Phongkeaw, Dr. Narasak Pandeck, and Mr. Thanundon Kongnok, for their kind counsel and camaraderie.

Finally, I most gratefully acknowledge my parents, sister, and brothers for their unwavering love, encouragement, and support throughout this education.

Tanawat Sawasdee

## CONTENTS

	Page
ABSTRACT IN THAI.....	I
ABSTRACT IN ENGLISH.....	II
ACKNOWLEDGEMENTS.....	III
CONTENTS.....	IV
LIST OF TABLES.....	VIII
LIST OF FIGURES.....	X
<b>CHAPTER</b>	
<b>I INTRODUCTION.....</b>	<b>1</b>
<b>II LITERATURE REVIEWS.....</b>	<b>3</b>
2.1 Transition metal carbides and nitrides (MXenes).....	3
2.1.1 Structure of layered MXenes.....	4
2.1.2 Surface functional groups.....	6
2.1.3 Synthesis and single-layer delamination of MXenes.....	6
2.2 Tunable properties of MXenes by structural modifications.....	8
2.2.1 Tuning atom type and n-ordering of the “M” transition metals.....	8
2.2.2 Tuning of the “X” atom.....	11
2.2.3 Tuning of the “T” surface functionals groups.....	12
2.2.4 External effects.....	16
2.3 Strong adsorption properties of MXenes.....	16
2.4 Li-ions applications.....	17
2.4.1 Reviews of MXenes as Li-ions applications.....	17
2.4.2 Key development of MXenes as electrode material for LIBs.....	20
2.4.3 Future research perspective for MXenes.....	23
2.5 Research Objectives.....	24
2.6 Scope and Limitations of the Study.....	24
2.7 Expectation Results.....	25

## CONTENTS (Continued)

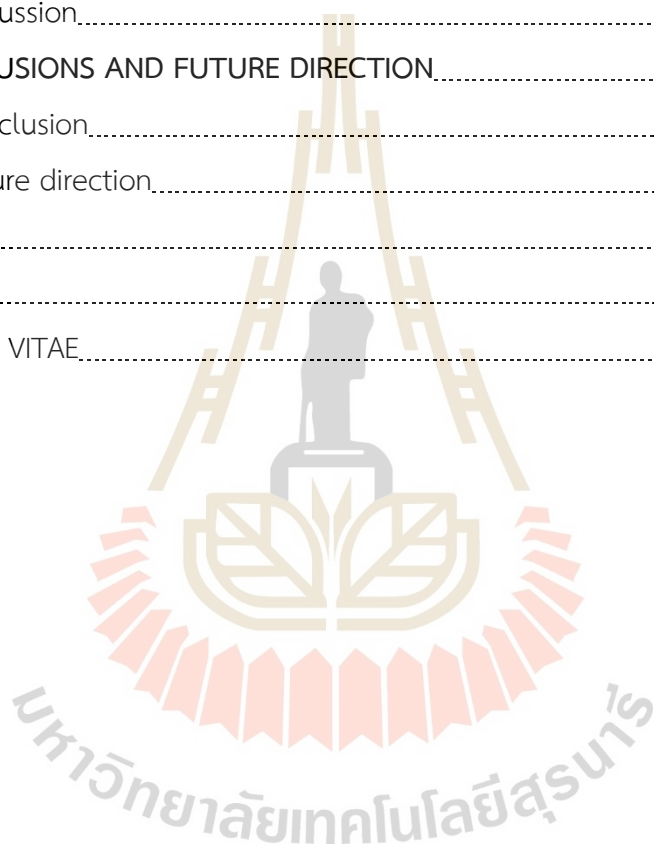
	Page
<b>III THEORETICAL BACKGROUND.....</b>	<b>26</b>
3.1 Many-body problem and Schrödinger equation.....	26
3.2 Density functional theory.....	28
3.2.1 Born-Oppenheimer Approximation.....	28
3.2.2 The Hohenberg-Kohn theorem.....	29
3.2.3 Kohn-Sham equations.....	30
3.2.4 The exchange-correlation energy.....	31
3.3 Projector augmented waves.....	33
3.4 Plane waves.....	34
3.5 Pseudo wavefunction and Pseudopotential.....	34
3.6 Van der Waals approximation.....	35
<b>IV RESEARCH METHODOLOGY.....</b>	<b>37</b>
4.1 Vienna ab initio simulation package (VASP).....	37
4.2 Structural optimization.....	38
4.2.1 Equation of state.....	38
4.3 Electronic properties.....	40
<b>V STRUCTURAL AND ELECTRONIC PROPERTIES OF <math>M_2CT_2</math> (<math>M = \text{Sc, Ti, V, Nb,}</math> AND <math>\text{Cr}</math>; <math>T = \text{O AND F}</math>) MONOLAYERS.....</b>	<b>42</b>
5.1 Structural properties.....	42
5.1.1 Computational details.....	43
5.1.2 Structural relaxation of the bare- $M_2C$ MXenes.....	44
5.1.3 Surface functional configurations and structural relaxations.....	47
5.2 Electronic properties and stability of the $M_2CT_2$ monolayer.....	54
5.2.1 Stability of the $T$ atoms on the $M_2C$ layer.....	54

## CONTENTS (Continued)

	Page
5.2.2 Effect of the layer thickness of the $M_2CT_2$ on the formation energy .....	58
5.2.3 Density of state.....	61
5.2.4 DOS plotting for different O-O length of $Ti_2CO_2$ and $CO_2$ .....	73
5.3 Discussion.....	78
<b>VI STUDIES ON THE STRUCTURAL CHARACTERISTICS OF <math>M_2CT_2</math> BILAYERS</b> .....	<b>81</b>
6.1 $X_{c,t,s}$ parameters for specifying bilayer structure.....	82
6.2 Bilayer stacking configurations.....	84
6.2.1 Energy profiles of relative sliding for the overlying layer.....	85
6.2.2 Translation and rotation vectors.....	88
6.2.3 Structural transformations of the bilayer.....	90
6.3 Formation and binding energies.....	95
6.4 Discussion.....	100
<b>VII STUDIES OF LI-ION AND CO-INTERCALATIONS IN MXENES</b> .....	<b>101</b>
7.1 Adsorption energy and voltage calculation for the Li-ions reaction.....	102
7.1.1 Results of the adsorption energy and the OCV calculations for Li-ions adsorption of the monolayer $Ti_2CO_2$ .....	102
7.1.2 Specific capacitance for Li-ions storage on $Ti_2CO_2$ .....	106
7.2 Diffusion properties of Li-ion and metals co-intercalation of bilayer MXenes.....	107
7.2.1 Li-ion mobility for MXenes monolayers.....	107
7.2.2 Li-ions intercalated bilayer MXenes.....	111
7.2.3 Diffusion rate and Selectivity of Li-ions intercalated bilayer MXenes.....	119

## CONTENTS (Continued)

	Page
7.2.4 Interlayer spacing induced by Co-intercalations of Li-ion in bilayer $Ti_2CO_2$ .....	124
7.3 Discussion.....	128
<b>VIII CONCLUSIONS AND FUTURE DIRECTION</b> .....	<b>130</b>
8.1 Conclusion.....	130
8.2 Future direction.....	132
REFERENCES.....	133
APPENDIX.....	145
CURRICULUM VITAE.....	149

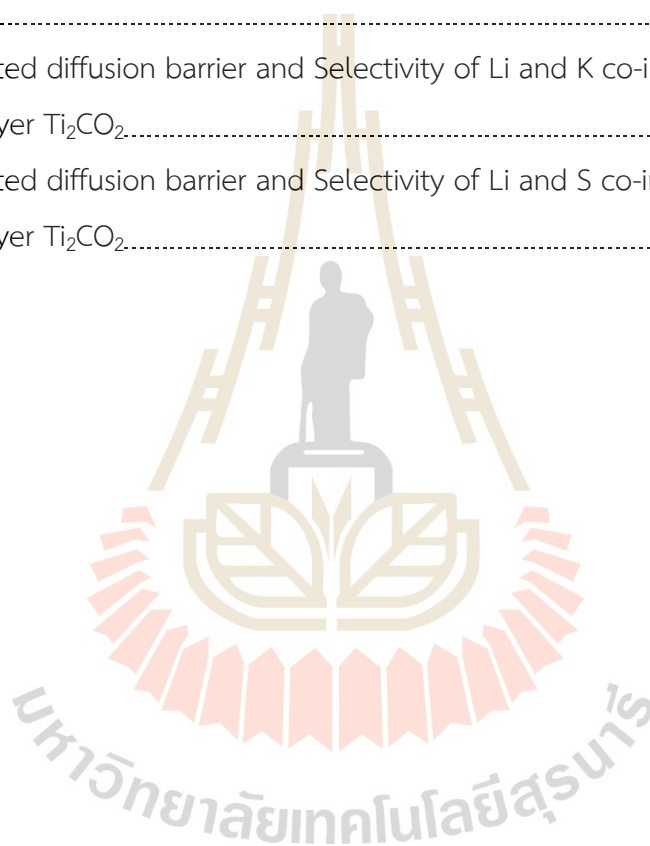


## LIST OF TABLES

Table	Page
2.1 Theoretical prediction for the LIBs and experimental information.....	19
5.1 The initial structural composition of bare- $M_2C$ MXenes.....	46
5.2 The calculation information of structural relaxations of the $M_2C$ compounds.....	46
5.3 The compositions of $T$ atom on both top and bottom surface of the $M_2C$ monolayer in the unit cell (where $M$ is Sc, Ti, V, Nb, Cr and $T$ is O, F).....	51
5.4 The structural relaxation of the $M_2CT_2$ monolayers where total energy, lattice parameter, and layer thickness are included.....	52
6.1 The combination of two single-layer of the $M_2CT_2$ bilayer (where $M$ is Sc, Ti, V, Nb, Cr and $T$ is O, F) in the unit cell from the combination of the $MM'$ , $M'O$ , and $OO$ monolayer models in which the “bold” letter indicate the closed interface types of both layers.....	84
6.2 Lowest formation energy of the bilayer structural configurations in each compound.....	98
7.1 The total energy and adsorption energy of the Li adsorption in the various sites for two Li adsorption layers.....	104
7.2 Correlation of Specific capacitance, numbers of the Li adatom, and the open circuit voltage.....	106
7.3 The relative energy and $x, y$ coordinates.....	110
7.4 The relative diffusion energy as a function of diffusion coordinate of the transition path I and II for the $Ti_2CO_2$ bilayer.....	112
7.5 Diffusion barrier information as a function of d-spacing along diffusion path I and path II.....	117

## LIST OF TABLES (Continued)

Table	Page
7.6 The relationship between the diffusion barriers and the selectivity of various temperatures, including 50 K, 100 K, 200 K, and 300 K, as a function of the d-spacing.....	122
7.7 Calculated diffusion barrier and Selectivity of Li and K co-intercalation atoms in bilayer $Ti_2CO_2$ .....	126
7.8 Calculated diffusion barrier and Selectivity of Li and S co-intercalation atoms in bilayer $Ti_2CO_2$ .....	126



## LIST OF FIGURES

Figure	Page
2.1 The structure of MAX phase bulk and MXenes monolayer (a), Monolayer of MXenes when selective etching A from MAX phases bulk (b), The periodic table and the compound elements of MAX phase bulk (Naguib et al., 2011).....	4
2.2 Three different structure including mono-M elements, a solid solution of at least two different M element, or ordered double-M elements, where one transition metal involve the outer layers and another fills middle layers can be made (Anasori et al., 2017).....	5
2.3 The structure for (a) $M_2X$ layer and (b) $M_3X_2$ layer arranging from the different $M$ and $X$ atomic compositions and the different possible positions of the functional atoms in which locate on the (c) A and B, and (d) C stacking sites of $M_2X$ layer and the (e) A, and (f) C and B stacking sites of $M_3X_2$ layer (Anasori et al., 2017).....	6
2.4 The timeline of synthesized MXenes (Alhabeab et al., 2017). ....	7
2.5 The symmetrically prediction of Li-ion mobility of MXenes that include the comparison for that of (A) $M_2C$ where $M$ is Ti, Hf, and Zr, (B)Ti, Ta and Mo, (C) $Ti_2C$ where the n-ordering vary by $n=1, 2$ and $3$ , (D) $Ti_2C$ with including functional atoms (F and O), (E) $Ti_2C$ comparing to that of $MoS_2$ and Graphene, (F, G, and H) applying the biaxial strain to $Ti_2C$ , $Ti_2CO_2$ , and $Ti_2CF_2$ , respectively (Zhang et al., 2017).....	10
2.6 Illustrations of (a) comparison of DOS between $Ti_3CNO_2$ and $Ti_3C_2O_2$ , and calculations of the charge density difference upon electron doping of $0.5e$ per supercell of (b) $Ti_3CNO_3$ and (c) $Ti_3C_2O_2$ (Jindata et al., 2021).....	11

## LIST OF FIGURES (Continued)

Figure	Page
2.7 (a) bare-Ti <sub>3</sub> C <sub>2</sub> surface and O functional atoms occupying on (b) the bottom surface, (c) the top surface, and (d) both bottom and top surface of Ti <sub>3</sub> C <sub>2</sub> of false color STEM image of a single Ti <sub>3</sub> C <sub>2</sub> T <sub>x</sub> sheet after heating 700 °C (Persson et al., 2017).....	13
2.8 The calculated DOS of bare-Ti <sub>2</sub> C, Ti <sub>3</sub> C <sub>2</sub> , Ti <sub>2</sub> CT <sub>2</sub> and Ti <sub>3</sub> C <sub>2</sub> T <sub>2</sub> , where T include F, O and OH (Bai et al., 2016).....	14
2.9 DOS of (a) bare-Sc <sub>2</sub> C, (b) the a-I model of Sc <sub>2</sub> CF <sub>2</sub> , (c) the a-I model of Sc <sub>2</sub> CO <sub>2</sub> , and (d)the a-II model of Sc <sub>2</sub> CO <sub>2</sub> (Khazaei et al., 2013).....	15
2.10 The comparison of the electronic structure by different of surface functional configurations of the O atom. model a-I present conductor with no energy gap whereas model a-II and a-III are semi-conductor with 2.965 eV and 3.118 eV, respectively (Guo et al., 2017).....	15
2.11 The specific capacity of exfoliated and delaminated of f-Ti <sub>3</sub> C <sub>2</sub> where inset shows SEM image of delaminated f-Ti <sub>3</sub> C <sub>2</sub> film (Mashtalir et al., 2013).....	22
2.12 Systematically calculation of the relation between theoretical gravimetric capacity and calculated voltage of Li <sub>2</sub> M <sub>2</sub> C(OH) <sub>2</sub> , Li <sub>2</sub> M <sub>2</sub> C(O) <sub>2</sub> , Li <sub>2</sub> M <sub>2</sub> C(F) <sub>2</sub> , Li <sub>2</sub> M <sub>2</sub> CH <sub>2</sub> , and Li <sub>2</sub> M <sub>2</sub> C <sub>2</sub> where M is early transition metals (Eames and Islam, 2014).....	22
2.13 Charge density difference after Li intercalation of (a) Ti <sub>2</sub> CH <sub>2</sub> and (b) Ti <sub>2</sub> CO <sub>2</sub> where red indicate decreasing of charge density, and dark blue indicate increasing of charge density (Eames and Islam, 2014).....	23
3.1 Illustration of the formally equivalent between the density functional theory (DFT) and the traditional quantum mechanics.....	31
3.2 Schematic illustrations of comparison of a wavefunction in the Coulomb potential of the nucleus (dashed blue) to the one in the pseudopotential (solid red) and above of the certain cutoff radius represents a radius that the real and the pseudo wavefunction and potentials match (Questaer, 2006).....	35

## LIST OF FIGURES (Continued)

Figure	Page
4.1 The self-consistent scheme used in the VASP code.....	38
4.2 The calculation procedure of DOS.....	41
5.1 MXenes family is indicated in the periodic table by the red, purple, and green regions, which represent the $M$ , $X$ , and $T$ atoms, respectively, and the frame of that color denotes the chosen atom in the research.....	43
5.2 The finding of an equilibrium structure of $Sc_2C$ , $Ti_2C$ , $V_2C$ , $Nb_2C$ , and $Cr_2C$ by fitting the calculations with the ROSE–Vinet’s equation of state where its plotting is represented by (a), (b), (c), (d), and (e), respectively.....	45
5.3 The preferable site of the $M_2C$ surfaces that include (a) $M$ , (b) $M'$ and (c) $O$ sites.....	48
5.4 Combinations of the $M$ , $M'$ and $O$ surface sites of the functional atoms forming $M_2CT_2$ structure that present (a) $MM$ , (b) $M'M'$ , (c) $OO$ , (d) $M'O$ , (e) $MM'$ and (f) $MO$ models.....	49
5.5 Comparisons formation energy between our calculation with the vdW interaction and the reference’s calculation without the vdW interactions of the $M'M'$ model of the $M_2CO_2$ MXenes (Khazaei et al., 2013).....	56
5.6 Formation energy of (a) $M_2CO_2$ and (b) $M_2CF_2$ monolayers with $M$ is Sc, Ti, V, Nb, and Cr transition metal.....	57
5.7 The plotting of the relation between layer thickness (d) and the formation energy of (a) $M_2CO_2$ and (b) $M_2CF_2$ .....	60
5.8 PDOS of $Sc_2CO_2$ with $MM$ , $MM'$ , $MO$ , $M'O$ , and $OO$ models rearranged according to formation energy value.....	62
5.9 PDOS of $Ti_2CO_2$ with $MM$ , $MM'$ , $MO$ , $M'O$ , and $OO$ models rearranged according to formation energy value.....	63

## LIST OF FIGURES (Continued)

Figure	Page
5.10 PDOS of $V_2CO_2$ with $MM$ , $MM'$ , $MO$ , $M'O$ , and $OO$ models rearranged according to formation energy value.....	64
5.11 PDOS of $Nb_2CO_2$ with $MM$ , $MM'$ , $MO$ , $M'O$ , and $OO$ models rearranged according to formation energy value.....	65
5.12 PDOS of $Cr_2CO_2$ with $MM$ , $MM'$ , $MO$ , $M'O$ , and $OO$ models rearranged according to formation energy value.....	66
5.13 PDOS of $Sc_2CF_2$ with $MM$ , $MM'$ , $MO$ , $M'O$ , and $OO$ models rearranged according to formation energy value.....	67
5.14 PDOS of $Ti_2CF_2$ with $MM$ , $MM'$ , $MO$ , $M'O$ , and $OO$ models rearranged according to formation energy value.....	68
5.15 PDOS of $V_2CF_2$ with $MM$ , $MM'$ , $MO$ , $M'O$ , and $OO$ models rearranged according to formation energy value.....	69
5.16 PDOS of $Nb_2CF_2$ with $MM$ , $MM'$ , $MO$ , $M'O$ , and $OO$ models rearranged according to formation energy value.....	70
5.17 PDOS of $Cr_2CF_2$ with $MM$ , $MM'$ , $MO$ , $M'O$ , and $OO$ models rearranged according to formation energy value.....	71
5.18 PDOS with different layer thickness of $Ti_2CO_2$ monolayer for the $M'M'$ model.....	75
5.19 PDOS with different layer thickness of $Ti_2CO_2$ monolayer for the $OO$ model.....	76
5.20 PDOS with different O-O length of $CO_2$ .....	77
5.21 The identical peak state, as indicated in the arrow pointing, of the O-p orbitals of both $M'M'$ and $OO$ models of $Ti_2CO_2$ monolayers and $CO_2$ .....	77
6.1 The $X_{c,t,s}$ parameter, which is used for simply identifying the bilayer system, for example, $X_{2,5,5}$ contain the $Ti_2CO_2$ compounds, “ $c = 2$ ”; layer-layer combined types of $M'M'-M'M'$ , “ $t = 5$ ”; and s5 stacking configurations, “ $s = 5$ ”.....	83

## LIST OF FIGURES (Continued)

Figure	Page
6.2 Top-down views of the overlying layer's translation of the MXenes bilayer along the fixed underlying layer with the (a) $M'M'-M'M'$ , (b) $M'O-M'O$ , and (c) $OO-OO$ bilayer's combined types of the $Ti_2CO_2$ .....	86
6.3 Energy profiles of the overlying layer's translation for the (a) $M'M'-M'M'$ , (b) $M'O-M'O$ , and (c) $OO-OO$ bilayer's combined types of the $Ti_2CO_2$ .....	87
6.4 Illustrations of the translation vectors in x and y coordinates include: (a) $d_i$ vector that begins from the underlying layer's $T_2$ atom to the overlying layer's $T_1$ atom, (b) possible high symmetric translation vectors composed of six directions (where $i = 1, 2, 3, 4, 5,$ and $6$ ), and (c) a reducible vector of the $d_i$ vector into d translation vector.....	89
6.5 Side view of in the $s_1, s_2, s_3, s_4, s_5,$ and $s_6$ stacking configurations of the $AM'-M'B$ bilayer's combined type.....	91
6.6 Top-down views of the $s_1, s_2, s_3, s_4, s_5,$ and $s_6$ stacking configurations.....	92
6.7 Simply implication for bilayer's stacking configuration transformation of (a) $AM'-M'B$ , (b) $AM'-OB$ , and (c) $AO-OB$ bilayer's combined types where light green border corresponds to the relative translation of (0, 0) coordinate of Figure 6.2.....	94
6.8 The symmetric structural transformations with $i = n+3$ and $j = n+2$ .....	94
6.9 Global estimation on the formation energy for the $M'M'-M'O, M'M'-OM', OM'-M'O, OM'-OM', M'O-OM', M'M'-OO, OM'-OO, M'O-OO,$ and $OO-OO$ combination types (violet, dark blue, blue, cyan, green, light green, yellow, orange, red, and pink colors, respectively), while the shading of the color of any layer-layer combination type in the plot indicates the various stacking configurations.....	96
6.10 Shifting of the global estimation on the formation energy where the lowest total energy in each compound had been shifted into 0 eV.....	97

## LIST OF FIGURES (Continued)

Figure	Page
7.1 The top views of (a) Li adsorption site for the 1st layer and (b) Li adsorption site for the 2nd layer of the monolayer $Ti_2CO_2$ .....	103
7.2 The schematics of the OCV calculations for the first and second layers of Li-ion adsorptions in the monolayer $Ti_2CO_2$ .....	104
7.3 The OCV and adsorption energy for Li-ions adsorption in the monolayer $Ti_2CO_2$ .....	105
7.4 The Li atom moves from the mi to the mt and then to the mi adsorption sites on the $Ti_2CO_2$ monolayer's surface.....	109
7.5 The relative energy along the diffusion path corresponds with Figure 7.4.....	109
7.6 The b-TS I (left red arrow) and b-TS II (right red arrow) sites are represented as the bilayer $Ti_2CO_2$ transition states for the diffusion path of path I and path II, respectively, while the b-IS site is indicated by a dark blue arrow.....	112
7.7 Relative diffusion energy (eV) as a function of diffusion coordinate (Å) for the diffusion path I and path II (red and blue lines, respectively) simulated by CI-NEB method.....	113
7.8 Relative energy of <i>b-IS</i> , <i>b-TS I</i> , and <i>b-TS II</i> Li's adsorption sites as a function of <i>d</i> -spacing (black, red, and blue lines, respectively).....	115
7.9 Relative diffusion barrier achieved by the differential energy between the transition state and the initial state at the same <i>d</i> -spacing for the diffusion path I and path II.....	115
7.10 The <i>z</i> -coordinate distance from the Li atom to both the underlying and overlying layers of <i>b-IS</i> , <i>b-TS I</i> , and <i>b-TS II</i> Li's adsorption sites as a function of the <i>d</i> -spacing.....	116
7.11 The general characteristic of the relative diffusion rate as a function of temperature.....	121

## LIST OF FIGURES (Continued)

Figure	Page
7.12 The relation between (a) the diffusion barrier (eV) of diffusion path II and (b) the selectivity of Li-ion diffusion over the Li-adsorption site equilibrium state at 50 K in the bilayer as a function of d-spacing (Å).....	123
7.13 The interlayer spacing induced by the various types of intercalations with the diffusion barrier of the diffusion path I and path II.....	125
7.14 Selectivity of Li and the co-intercalation of (a) K atom and (b) S atom as a function of the temperatures.....	127



# CHAPTER I

## INTRODUCTION

Throughout the past few decades, two-dimensional (2D) materials have attracted increasing attention due to their remarkable physical properties. Most of 2D materials have layered structure that show significantly different properties comparing to their bulk form. Among the 2D materials, Graphene and Transition metal dichalcogenides (TMDs) have been widely investigated in both theoretical and experimental researches (Novoselov *et al.*, 2004; Wang *et al.*, 2012; Mak *et al.*, 2010; Bertolazzi *et al.*, 2011). These layered materials have stacks of strongly bonded layers with weak vdW interlayer interactions allowing to exfoliation into 2D layers of atomically thin thickness (Novoselov *et al.*, 2005). Graphene is a monolayer counterpart of graphite having layered honeycomb structure. An electronic structure of graphene has a linear dispersion and charge carriers can be described as massless Dirac fermions (Geim and Novoselov, 2007). However, pristine graphene is limited its application due to zero energy gap. Hence, the remarkable properties of graphene have renewed in thin layer of TMDs which have sizeable band structure crossing from indirect in bulk form to direct gap in monolayer form (Kuc *et al.*, 2011). Interlayer spacing of TMDs makes them possible for intercalation by metal ions such as alkali metals. In 2014, potassium atoms were intercalated into interlayer vdW gap at the surface of bulk MoS<sub>2</sub> which was investigated by angle-resolved photoemission spectroscopy (ARPES) technique reported by Eknapakul and co-workers (Eknapakul *et al.*, 2014). It has been investigated that intercalation of alkali metals significantly alters electronic structure of TMDs. This approach has shown a potential for tuning the electronic structure of layered structure materials.

Recently, transition metal carbides and nitrides are almost the latest additions to the 2D materials having a graphene-like structure so called MXenes (Naguib *et al.*, 2011). MXenes exhibit ultra-large interlayer spacing in which Ti<sub>3</sub>C<sub>2</sub>-MXenes exhibit the original interlayer spacing of 0.977 nm which are greater than that of TMDs (~ 0.3 nm) (Luo *et al.*, 2017). Hence, the ultra-large interlayer spacing makes it easier to intercalate

ions and attracted huge attention for high-performance capacitors. Furthermore, MXenes family have environmental friendly, excellent biocompatibility and thermodynamically stable in water so that some of them have proper band structure to generate  $H_2$  from water by photocatalysis process (Khazaei *et al.*, 2017). Due to the unique properties of MXenes, a growing family has been becoming an important candidate for many applications such as electrode materials for energy storage devices such as alkali metals ion ( $Li^+$ ,  $K^+$ ,  $Na^+$ ) batteries, supercapacitors, ion capacitors, hydrogen storage, and hydrogen harvesting material from photocatalytic process (Anasori *et al.*, 2017; Peng *et al.*, 2019; Lashgari *et al.*, 2014; Zhao *et al.*, 2015; Sun *et al.*, 2018). Restriction in structural features, such as the arrangement of their surface functional of MXenes, can, however, be extended further. For this reason, the modification of its electronic property, ionic mobility along the surface and so on for many applications can then be achieved. Moreover, some of the structural configurations and their electronic properties have not been examined yet. As a result, the lack of different site combinations for the surface functional groups, which may be potential for various property, will be performed in this work. In addition, the structural properties, the electronic properties, and Li-ions application for these surface configurations for MXenes are focused. We hope that this work will provide more insight into MXene's structural and electronic properties and will be the guideline for some experimental research in the future.

## CHAPTER II

### LITERATURE REVIEWS

It is well known that MXenes have attracted a lot of interest as appropriate materials for a variety of specialized qualities in both experimental and theoretical research. However, the electrical and structural properties of MXenes are still not well understood in the scientific literature. In this chapter, we present brief reviews of the literature on 2D transition metal carbide and nitrides (MXenes), including structural and synthesis reports, reports on tuning intrinsic properties by modifying their structure, strong adsorption properties, and layered MXenes Li-ion batteries. This chapter also provides more insights into the electronic structure of the literature reviews.

#### 2.1 Transition metal carbides and nitrides (MXenes)

MXenes are made by selective etching of certain atomic layers from their bulk precursors, such as the MAX phase. The MAX phase is a very large family of ternary carbides and nitrides that consist of the chemical compositions of  $M_{n+1}AX_n$  e.g.,  $Ti_3AlC_2$  and  $Ti_2AlC$ . Because the bonding between  $M$  and  $A$  atoms is metallic, the separation of the  $M_{n+1}X_n$  layers by mechanical technique is not possible. Thus, wet etching, or chemical exfoliation of the MXenes synthesis process, such as etching with aqueous hydrofluoric acid (HF) or by *in situ* formation of HF through the hydrochloric acid (HCl) and fluoride reaction, is the most widely used method to fabricate them (Naguib *et al.*, 2014; Ghidui *et al.*, 2014; Srivastava *et al.*, 2016). During the chemical exfoliation, by removing “A” atom, the MAX phase is transformed into a multi-layered structure which will be provided as MXenes, as indicated in Figure 2.1.

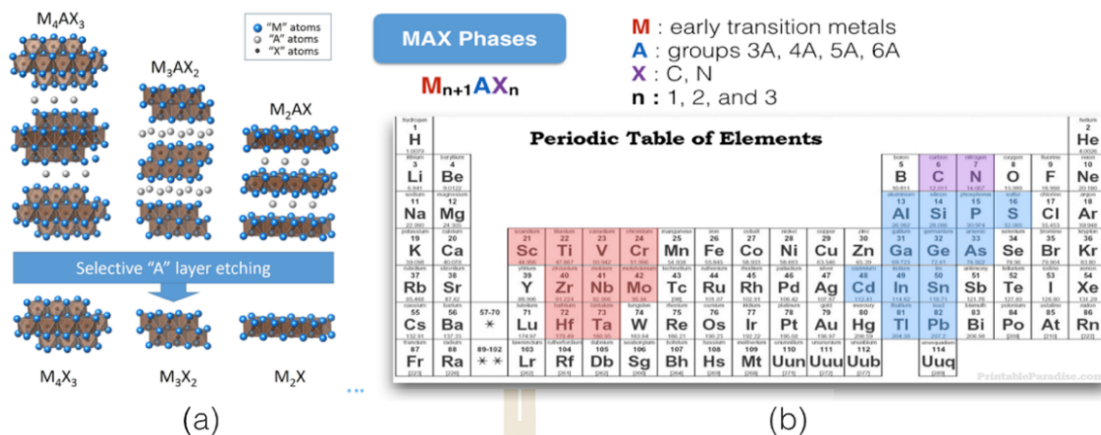


Figure 2.1 show the structure of MAX phase bulk and MXenes monolayer (a), Monolayer of MXenes when selective etching A from MAX phases bulk (b), The periodic table and the compound elements of MAX phase bulk (Naguib *et al.*, 2011).

### 2.1.1 Structure of layered MXenes

The chemical compositions of MXenes are given by the formula  $M_{n+1}X_n$ , which is later denoted as bare-MXenes, where  $n = 1, 2, \text{ or } 3$ , “M” represents an early transition metal, e.g., Sc, Ti, Zr, Hf, V, Nb, Ta, Cr, and Mo, and “X” represents carbon or nitrogen. At least three different formulas of MXenes, which are  $M_2X$ ,  $M_3X_2$  and  $M_4X_3$  can be made. Furthermore, three different forms of structures can be achieved, as shown in Figure 2.2, which include the following (Anasori *et al.*, 2017). “Mono-M elements” consist of only one element of M transition metal in the formulas, for example,  $Ti_2C$ ,  $Sc_3C_2$  and  $Nb_4C_3$ . “A solid solution” consists of at least two different elements of M transition metal in the formulas, for example  $(Mo, Ti)_3C_2$  and  $(Nb, Sc)_2C$ . “Ordered double-M elements” consist of one transition metal involve the outer layers and another fills middle layers, for example  $Mo_2TiC_2$  in which Ti locate at the middle layer and be covered by the perimeter Mo layers. Anasori had also presented the structural constructing of MXenes in the simple way to understand. The overall atomic structure of the  $M_2X$ ,  $M_3X_2$  and  $M_4X_3$  MXenes structure is combined with a hexagonal close-packed stacking that corresponds to the hexagonal building blocks of their precursors, such as the MAX phase. The X atoms are located inside the M close packed structure, performing the octahedral interstitial sites. The representation of capital

Roman and Greek letters may refer to the  $M$  and  $X$  positions in the structure, respectively. The  $\alpha$ ,  $\beta$ , and  $\gamma$  positions are vertically directed to the A, B, and C, respectively. Therefore, the arrangement of  $M_2X$  and  $M_3X_2$  is  $B\gamma A$  and  $B\gamma\beta C$  stacking composition, respectively, where the structure of layered  $M_2X$  and  $M_3X_2$  is shown in Figure 2.3. In addition, the arrangement of  $M_4X_3$  is  $B\gamma\beta C\alpha B$  stacking composition. For the double layer structural form,  $B\gamma A-A\gamma B$  for  $M_2X-M_2X$ ,  $B\gamma\beta C-C\beta\gamma B$  for  $M_3X_2-M_3X_2$ , and  $B\alpha C\beta\gamma B-B\gamma\beta C\alpha B$  for  $M_4X_3-M_4X_3$  ordering are presented.

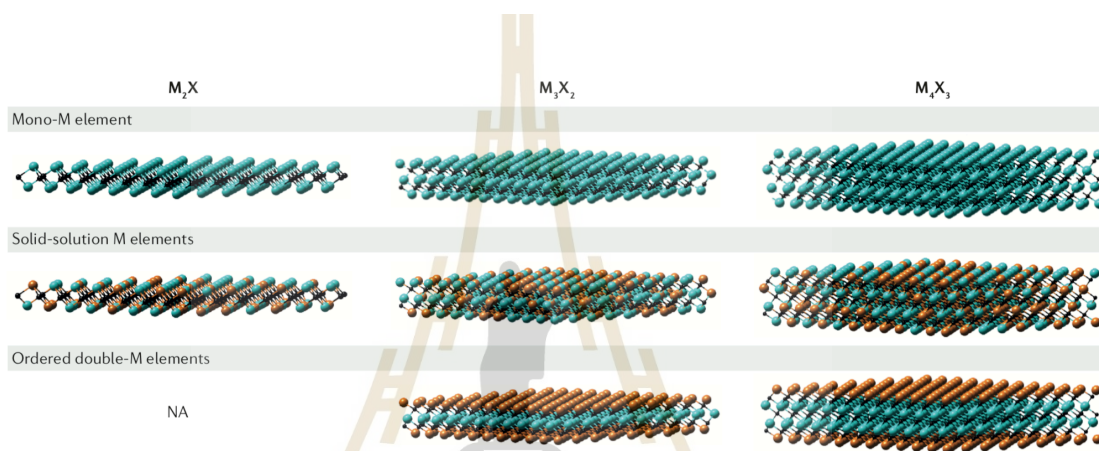
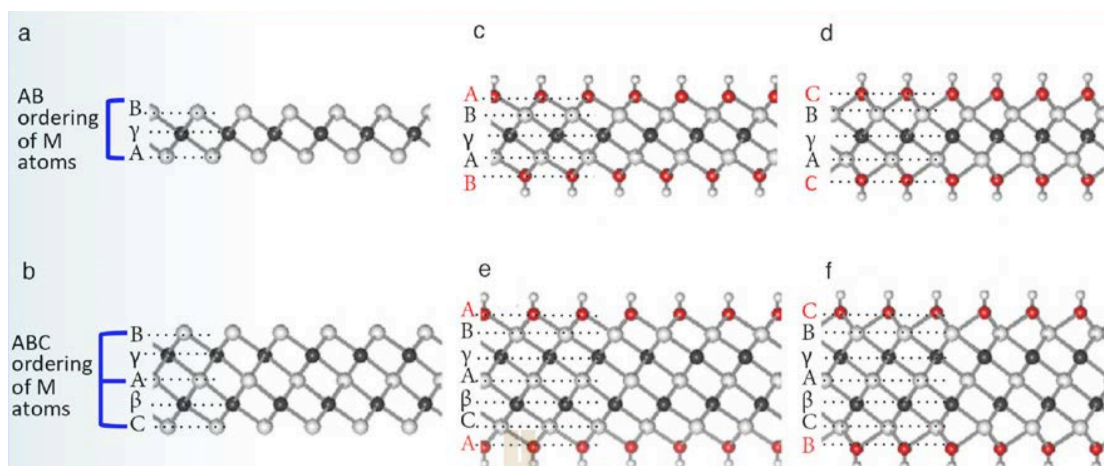


Figure 2.2 show three different structure including mono- $M$  elements, a solid solution of at least two different  $M$  element, or ordered double- $M$  elements, where one transition metal involve the outer layers and another fills middle layers can be made (Anasori *et al.*, 2017).



**Figure 2.3** present the structure for (a)  $M_2X$  layer and (b)  $M_3X_2$  layer arranging from the different  $M$  and  $X$  atomic compositions and the different possible positions of the functional atoms in which locate on the (c) A and B, and (d) C stacking sites of  $M_2X$  layer and the (e) A, and (f) C and B stacking sites of  $M_3X_2$  layer (Anasori *et al.*, 2017).

### 2.1.2 Surface functional groups

During the etching process, all MXenes samples, which synthesis using the acidic-fluoride-containing solutions, are covered by surface functional groups ( $T_x$ ) such as -O, -F, and -OH. MXenes with the functional groups denote as  $M_{n+1}C_nT_x$  where  $T_x$  represents the functional groups. Since none of bare-MXenes are successfully synthesized, most of the computational studies usually consider the surface functional groups, to evaluate the properties for MXenes. By calculating the electronic properties, such as the Formation energy, the computational work can predict the proper site for the  $T$  atom that will include three possible sites in which the  $T$  functional groups can be placed on the surface of  $M_{n+1}X_n$  MXenes which is A, B and C stacking sites as indicated in Figure 2.4.

### 2.1.3 Synthesis and single-layer delamination of MXenes

The timeline of the experimental exfoliation methods are collected by Alhabeab that would provide a guideline for synthesis of MXenes, as indicated in (Alhabeab *et al.*, 2017). After  $Ti_3C_2T_x$  multilayered MXenes was synthesized by using HF acid for the exfoliation in 2011, a variety of different MXenes, such as  $Ti_2CT_x$ ,  $(Ti,Nb)_2CT_x$ ,  $(V,Cr)_3C_2T_x$ ,

$Ti_3CNT_x$ , and  $Ta_4C_3T_x$ , were also successfully made in 2012 (Naguib *et al.*, 2012). In 2013, single layers of MXenes were isolated by intercalation and delamination with organic molecules (Mashtalir *et al.*, 2013). In 2014, in situ HF etchants such as  $NH_4HF_2$  or LiF/HCl mixture were used as the exfoliation method of  $Ti_3C_2T_x$  (Halim *et al.*, 2014). Additionally, the isolation of single flakes of  $Ti_3C_2T_x$  are done by clay-like behavior method that sonicate of  $Ti_3C_2T_x$  clay in water (Ghidiu *et al.*, 2014). In 2015, the report of using the amine-assisted method or TBAOH for high yield delamination of MXenes were achieved (Mashtalir *et al.*, 2015). Furthermore, the ordered double-*M* elements, e.g.,  $Mo_2TiC_2T_x$ ,  $Cr_2TiC_2T_x$ , and  $Mo_2TiC_3T_x$ , are discovered (Naguib *et al.*, 2015). In 2016, delamination and isolation of large single flakes of  $Ti_3C_2T_x$  were achieved through optimization of the LiF/HCl exfoliation method, which is referred to MILD (Anasori *et al.*, 2015). In 2017,  $Mo_{1.3}CT_x$  MXenes with ordered divacancies was achieved by exfoliating one of the transition metals from in-plane double transition metal MAX phase, such as  $Mo_{2/3}Sc_{1/3}AlC$  (Tao *et al.*, 2017).

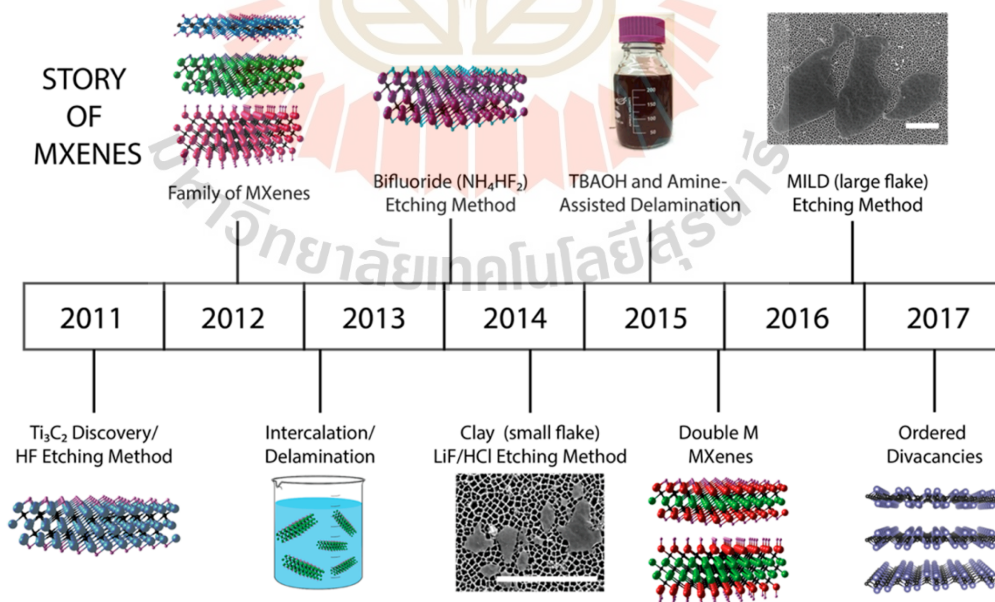


Figure 2.4 present the timeline of synthesized MXenes (Alhabeab *et al.*, 2017).

## 2.2 Tunable properties of MXenes by structural modifications

Since MXenes compose of wide chemical and structural variety, these makes them competitive among the 2D materials. For this reason, theoretical and experimental works report about tunable intrinsic properties of MXenes by either structural form modifications or changing their elemental compositions. Additionally, the characteristics of MXenes may be altered by structural changes such as (1) adjusting the atom type and  $n$ -ordering of the "M" transition metals, (2) tuning the "X" atom, (3) tuning the "T" surface functional groups, and (4) external influences where examples are listed in the following.

### 2.2.1 Tuning atom type and $n$ -ordering of the "M" transition metals

A complex material made of mixture of light and heavy transition metals can be chosen from MAX phase before the etching process, which makes it possible to tune the number of valence electrons and its electronic property. For example, despite  $Ti_3C_2T_x$  is metallic, the Mo-containing in the  $Ti_3C_2T_x$  exhibits semiconductor-like properties conforming that changing the layers ordered can affect to the electronic properties (Anasori et al., 2015). Based on DFT calculation, the stability properties of  $M'$  and  $M''$  mixed transition metal of monolayer  $Mo_2M''_n C_{n+1} T_x$  (where  $M''$  is Ti, V, Ta and Nb;  $n = 1$  or 2) MXenes are predicted. The result show that  $Mo_{2+x}M''_{1-x}C_2$  and  $Mo_{2+x}M''_{2-x}C_2$  and with higher concentration of  $M''$  in the middle layer will provide higher stability in the structure. In addition, the comparison of calculating DOS for  $Mo_3C_2T_x$ ,  $Mo_2TiC_2T_x$ , and  $Ti_3C_2T_x$  also confirmed that DOS of the  $M'$  and  $M''$  mixed system shift down to the lower energy region leading them to perform lower of the total energy.

Recently, Nb-transition metal substitution in scandium-based carbide MXenes ( $ScNbCO_2$ ) are performed in term of density functional calculation (Guo *et al.*, 2017). Interestingly, by rearranging positional of Nb and Sc transition metal atoms, their electronic structures are changed which would be further provided as band engineering material. The calculation of partial DOS indicated that  $d_{x^2-y^2}$  orbital of Nb-atom, which below fermi-level ( $E_f$ ), obtained the charge from the Sc-atom leading it to decrease in the energy gaps. By the Nb-doping, a direct energy gap was also obtained that provide

the visible light adsorption coefficient to be remarkably improved allowing applications such as transistors and optoelectronic devices.

In 2017, Zhang symmetrically predicted that Li-ion mobility of bare- $M_2C$  MXenes, where  $M$  is Ti, Zr, Hf, Ta and Mo, are extremely low compared to that of TMDs, e.g.,  $MoS_2$ , and graphene as shown in Figure 2.5 (A), (B) and (E) (Zhang *et al.*, 2017). In Figure 2.5 (A), (B) and (C) show that a tendency of different  $M$  transition metals atom and the  $n$ -ordered layer of  $M_2C$  affects to a diffusion barrier in transition states in which its different of energy range does not greater than 20 meV. However, the addition of the functional groups, such as O and F as indicated in Figure 2.5 (D), leading the Li-ion diffusion barrier to increase about 10 times to that of nonfunctional groups.



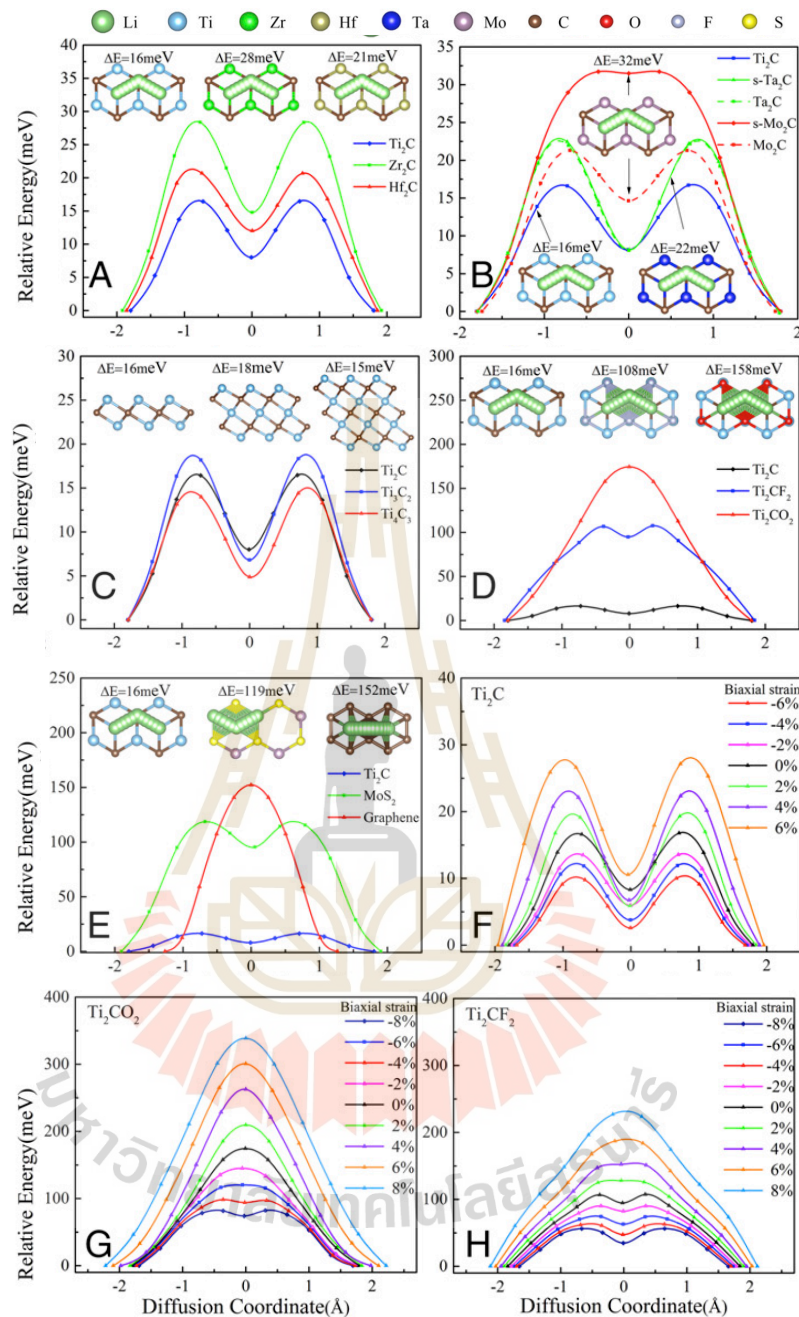
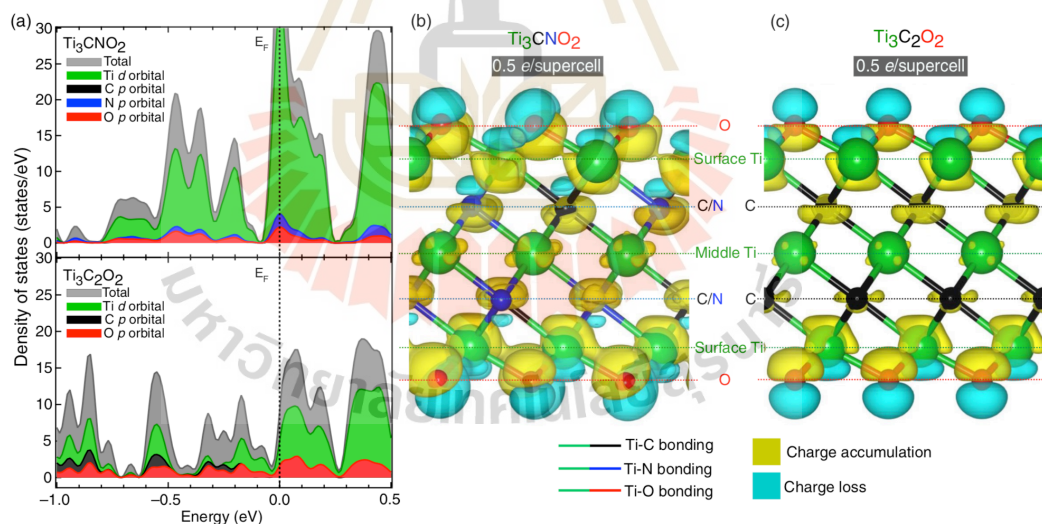


Figure 2.5 show the symmetrically prediction of Li-ion mobility of MXenes that include the comparison for that of (A) $M_2C$  where  $M$  is Ti, Hf, and Zr, (B) $Ti$ , Ta and Mo, (C)  $Ti_2C$  where the  $n$ -ordering vary by  $n = 1, 2$  and  $3$ , (D) $Ti_2C$  with including functional atoms (F and O), (E)  $Ti_2C$  comparing to that of  $MoS_2$  and Graphene, (F, G, and H) applying the biaxial strain to  $Ti_2C$ ,  $Ti_2CO_2$ , and  $Ti_2CF_2$ , respectively (Zhang *et al.*, 2017).

## 2.2.2 Tuning of the “X” atom

$M_3C_2T_x$ ,  $M_3N_2T_x$  and  $M_3CNT_x$  may refer to transition metals carbide (TMC), transition metals nitride and transition metals carbonitride, respectively. Some report shows a different electronic properties of different X atom such as the following example. The reason of  $Ti_3CNT_x$  becoming higher charge capacitance than  $Ti_3C_2T_x$  compound, by replacing N to C atoms of  $Ti_3C_2T_x$ , was explained (Jindata *et al.*, 2021). In details, the first experimental observation of the spectroscopic signature of negative electronic compressibility (NEC) in MXenes and theoretically calculations were confirmed that  $Ti_3CNT_x$  allowing more charge to be stored in the material, as indicated in Figure 2.6(b) and (c). In addition, the hybridization of titanium-nitrogen bonding in  $Ti_3CNO_2$  helps to promote the available states of Ti atoms for gaining more electrons above the fermi level, as indicated in Figure 2.6(a), which could be applied to enhance energy storage materials.



**Figure 2.6** indicate (a) comparison of DOS between  $Ti_3CNO_2$  and  $Ti_3C_2O_2$ , and calculations of the charge density difference upon electron doping of  $0.5e$  per supercell of (b)  $Ti_3CNO_3$  and (c)  $Ti_3C_2O_2$  (Jindata *et al.*, 2021).

### 2.2.3 Tuning of the “T” surface functionals groups

Some of reports showed that optical response, crystal structure, and electronic structure may strong dependence on the surface functional groups and its position offering possibilities for surface state engineering (Bai *et al.*, 2016; Lashgari *et al.*, 2014). Recently, the report of electron energy-loss spectroscopy in scanning transmission electron microscope (STEM) (Karlsson *et al.*, 2015; Wang *et al.*, 2015), high-quality neutron total scattering (Wang *et al.*, 2016), and NMR spectroscopy (Hope *et al.*, 2016) in the surface functional groups of  $Ti_3C_2T_x$  MXenes compound were presented. As a result, the studies confirmed that a random distribution of the  $T_x$  on MXenes surfaces is preferable than a certain kind of functional group. Interestingly, the surface functional groups on the layer of  $Ti_3C_2T_x$  MXenes had been selected by increasing the temperature during the synthesis process (Persson *et al.*, 2017). As indicated in Figure 2.7, the organization of the surface types on  $Ti_3C_2T_x$ -MXenes were accomplished as a function of temperature in which the functional F was found to be predominate over the functional O at room temperature. Furthermore, the F functional desorbs, and the O functional moved to the alternative site after the temperature over 550°C.

Furthermore, some reports presented that the properties may depend on the  $T_x$  functional atom type. Although, both MAX phase bulk and bare-MXenes are all reported to be metallic (Barsoum and Radovic, 2011; Khazaei *et al.*, 2013; Khazaei *et al.*, 2014), eight types of MXenes with functional groups transforming to semiconductor, including  $Sc_2C(OH)_2$ ,  $Sc_2CF_2$ ,  $Sc_2CO_2$ ,  $Ti_2CO_2$ ,  $Zr_2CO_2$ ,  $V_2CF_2$ ,  $V_2C(OH)_2$  and  $Hf_2CO_2$ , were provided (Tang *et al.*, 2012; Zhang *et al.*, 2015; Hu *et al.*, 2014; Khazaei *et al.*, 2013). Figure 2.9 depicts the DOS of bare- $Sc_2C$ ,  $Sc_2CO_2$ , and  $Sc_2CF_2$ , whereas Figures 2.9(c) and (d) illustrate different functionalization positions, indicating the transformation of metallic to semiconductor by the presence of the F or O atom. Additionally, the electronic and optical properties of pristine and functionalized of monolayer  $Ti_2C$  and  $Ti_3C_2$  with F, OH, and O were theoretically examined (Bai *et al.*, 2016). The total density of state (TDOS), as shown in Figure 2.8, indicates that the monolayer of  $Ti_2C$ ,  $Ti_2CT_2$ ,  $Ti_3C_2$  and  $Ti_3C_2T_2$  (where  $T$  is O, F and OH functional groups), except  $Ti_2CO_2$ , have DOS around the fermi energy exhibiting electronic conduction behaviors. Whereas  $Ti_2CO_2$  is the one that has a narrow band gap because of, although, the DOS at  $E_f$  are mainly

dominated by Ti-d state in bare, F and OH functional of  $Ti_2C$ , the O-p state take place in the valence bands from -6.0 eV to 0 eV, in which strongly hybridize with both Ti-d and C-p state, leading  $E_f$  to shift downward to the narrow gap.

Compositions of the surface functional groups can also affect their electronic properties. For example, by calculating the band structure in the Sc base MXenes, despite  $Sc_2CO_2$  are reported to be semiconductor for a-II and a-III model of O functional group configurations, a-I model perform conducting behavior (Guo *et al.*, 2017). The bond length between Sc and O of the a-I model is shortest among others which may affect to the electronic orbital at the Fermi energy of the electronic structure as shown in Figure 2.10.

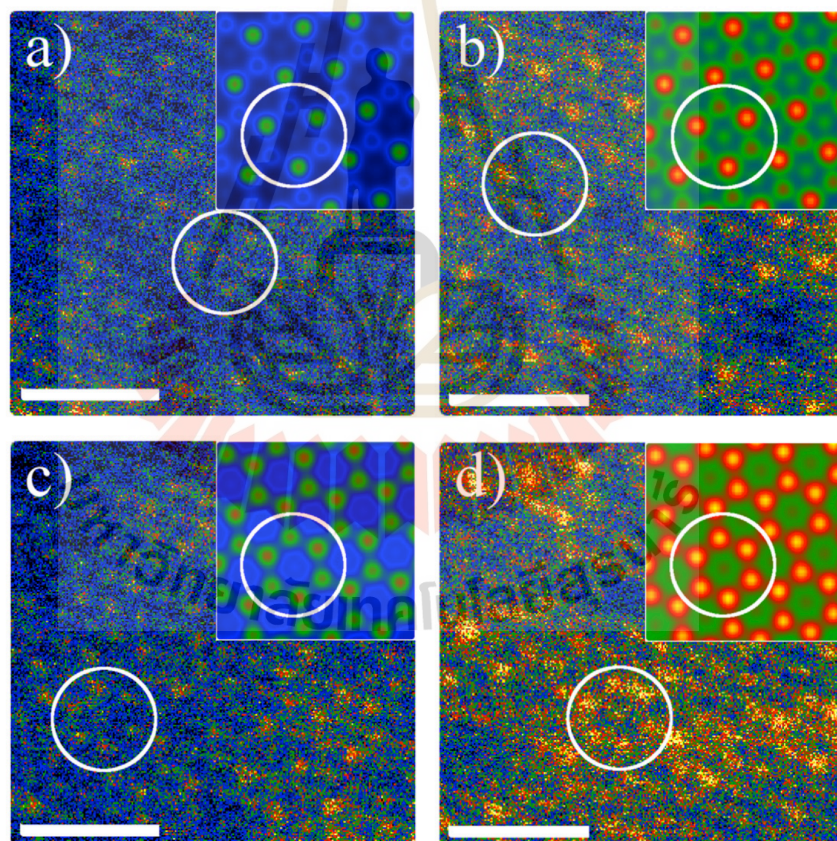


**Figure 2.7** show (a) bare- $Ti_3C_2$  surface and O functional atoms occupying on (b) the bottom surface, (c) the top surface, and (d) both bottom and top surface of  $Ti_3C_2$  of false color STEM image of a single  $Ti_3C_2T_x$  sheet after heating  $700^\circ C$  (Persson *et al.*, 2017).

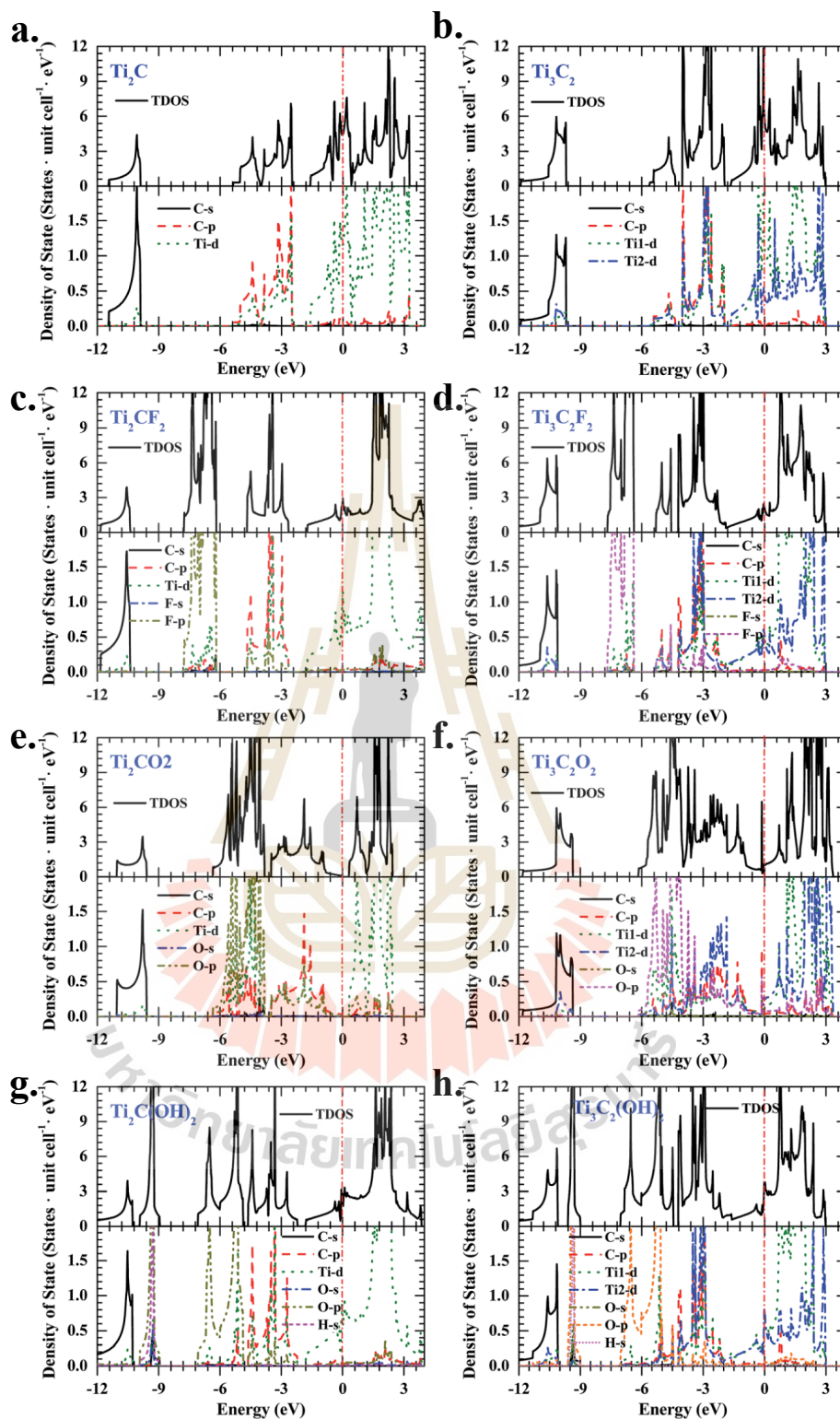


Figure 2.8 show the calculated DOS of bare- $\text{Ti}_2\text{C}$ ,  $\text{Ti}_3\text{C}_2$ ,  $\text{Ti}_2\text{CT}_2$  and  $\text{Ti}_3\text{C}_2\text{T}_2$ , where  $T$  include F, O and OH (Bai *et al.*, 2016).

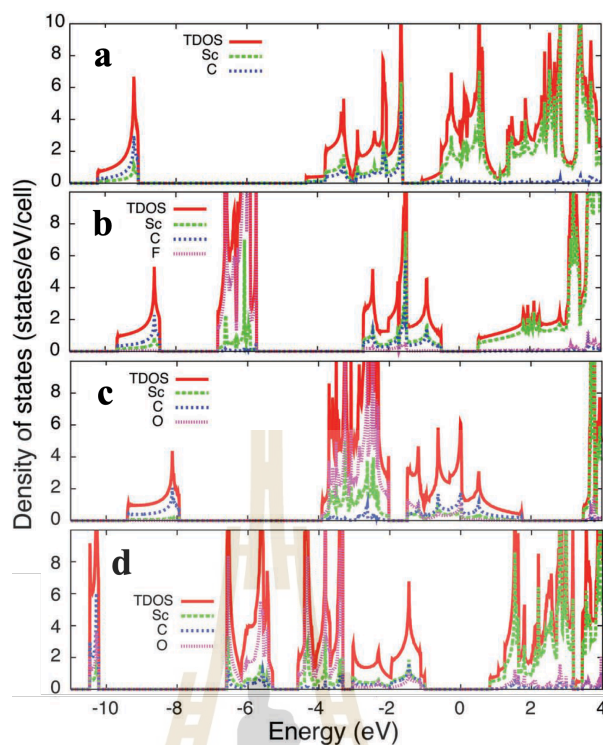


Figure 2.9 DOS of (a) bare- $\text{Sc}_2\text{C}$ , (b) the a-I model of  $\text{Sc}_2\text{CF}_2$ , (c) the a-I model of  $\text{Sc}_2\text{CO}_2$ , and (d) the a-II model of  $\text{Sc}_2\text{CO}_2$  (Khazaei *et al.*, 2013).

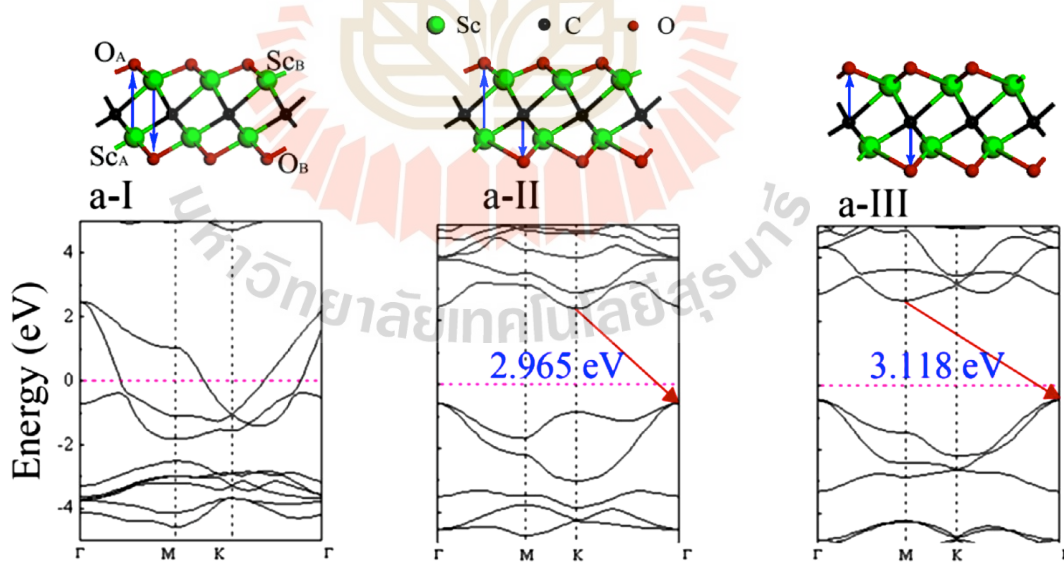


Figure 2.10 show the comparison of the electronic structure by different of surface functional configurations of the O atom. model a-I present conductor with no energy gap whereas model a-II and a-III are semi-conductor with 2.965 eV and 3.118 eV, respectively (Guo *et al.*, 2017).

#### 2.2.4 External effects

Generally, applying strain, external charge, electric field, and impurity may affect to the electronic structure, ionic mobility, and charge distribution on the surface of materials (Van de Walle and Neugebauer, 2004; Schedin *et al.*, 2007; Zhang *et al.*, 2017). Zhang reported that, by applying strain to the layer of  $\text{Ti}_2\text{C}$ ,  $\text{Ti}_2\text{CO}_2$  and  $\text{Ti}_2\text{CF}_2$ , the significant change of Li-ion mobility was simulated as shown in Figures 2.5(F), (G) and (H). Lee and co-worker symmetrically reported that tuning of indirect-direct energy gaps was done by applying strain to monolayer  $\text{Sc}_2\text{CO}_2$  allowing high carriers mobility in a novel optical nanodevice (Lee *et al.*, 2014). Effects of strain on bulk and few layer semiconductors may result in tunable electronic structure as well (Peelaers and Van de Walle, 2012; Desai *et al.*, 2014; Fan *et al.*, 2015; Chang *et al.*, 2013; Su *et al.*, 2014). Moreover, the tuning of indirect-direct band structure in 2D semiconductors were systematically investigated to greatly enhancement of the absorption coefficients in low photon-energy range (Miao *et al.*, 2017).

### 2.3 Strong adsorption properties of MXenes

The spontaneous intercalation of cations from aqueous salt solutions, including  $\text{Na}^+$ ,  $\text{K}^+$ ,  $\text{NH}_4^+$ , and  $\text{Al}^{3+}$ , had been demonstrated on between  $\text{Ti}_3\text{C}_2$  layered MXenes and found that these variety of cations co be intercalated electrochemically, offering capacitance in excess of  $300 \text{ Fcm}^{-3}$  (Lukatskaya *et al.*, 2013). In addition, because of MXenes exhibiting ultra large interlayer spacing, it was easily intercalate for  $\text{Li}^+$ ,  $\text{K}^+$  and  $\text{Na}^+$  ions performing good performance for energy storage material (Anasori *et al.*, 2017). The alkali, alkaline earth, and some lanthanide ions, which do not directly contribute to the band formation, can be able to construct for the crystal structure by intercalation process. Moreover, based on the calculation of the formation energy, Li *et al.* revealed that almost all the transition metal atoms, excepting Cd and Hg, in gas phase were strongly absorb on the surface of  $\text{Sc}_2\text{CO}_2$ ,  $\text{Nb}_2\text{NO}_2$  and  $\text{Ta}_2\text{NO}_2$  (Li *et al.*, 2018). Because of the intercalation of chosen light and heavy transition metals ion into MXenes were possible, MXenes may provide as a candidate for next-generation energy storage devices such as alkali ion battery and metal ion capacitors. Furthermore,

electrically conducting with polymers and transition metal oxides such as  $\text{RuO}_2$ , also provided higher volumetric and areal capacitance in macro-porous  $\text{Ti}_3\text{C}_2\text{T}_x$  films (Lukatskaya *et al.*, 2017).

## 2.4 Li-ions applications

Energy harvesting and storage materials are a key development of today's technology such as Li-ion batteries (LIB) for transportation and energy storage devices. Since, graphene had involved high electrochemical properties of anode material for rechargeable LIBs, such as the large surface areas, low migration barrier and broad voltage windows (Yoo *et al.*, 2008). However, extensive research has been attempted to explore and develop new anode materials with higher capacities and long-lasting than current. Furthermore, other graphene-like 2D materials, such as transition metal dichalcogenides (TMD) (Jing *et al.*, 2013) and MXenes (Mashtalir *et al.*, 2013), have also been widely studied exhibiting high specific capacity and extremely high charging rates. To date, it is still a challenge to obtain a satisfactory electrode with good electrical conductivity, excellent cycling stability, and high-rate capability.

### 2.4.1 Reviews of MXenes as Li-ions applications

Since, MXenes compose of wide element compositions and provide of tunable structure, the competitive among the 2D materials make them popular in the worldwide research especially in energy storage application. In 2012, the reversible capacity of layered  $\text{Ti}_2\text{CT}_x$  had been reported, at 1 C, to be  $110 \text{ mA}\cdot\text{h}\cdot\text{g}^{-1}$  after 80 cycles (Naguib *et al.*, 2012). Furthermore,  $\text{Nb}_2\text{C}$  and  $\text{V}_2\text{C}$  with functional groups ( $f\text{-Nb}_2\text{C}$  and  $f\text{-V}_2\text{C}$ ) are experimentally reported as promising electrode materials for LIBs which achieve high charge-discharge rate of reversible capacities of 170 and  $260 \text{ mA}\cdot\text{h}\cdot\text{g}^{-1}$  at 1 C cycling rates, respectively (Naguib *et al.*, 2013). A large capacity of first cycle capacity of  $\text{V}_2\text{CT}_x$  of  $\sim 380 \text{ mA}\cdot\text{h}\cdot\text{g}^{-1}$  is obtained while that of  $\text{Nb}_2\text{CT}_x$  is obtained to be  $\sim 422 \text{ mA}\cdot\text{h}\cdot\text{g}^{-1}$ . In addition, high theoretical capacitance of single layered  $\text{Nb}_2\text{CO}_2$ ,  $\text{V}_2\text{CO}_2$  and  $\text{Ti}_2\text{CO}_2$  had symmetrically predicted to be 233-250, 335-367 and  $350 \text{ mA}\cdot\text{h}\cdot\text{g}^{-1}$ , respectively (Eames and Islam, 2014; Xie *et al.*, 2014).

The calculated diffusion barriers of MXenes, particularly for bare- $M_2C$  MXenes, are expected to be remarkably low, ranging from 0.01 to 0.05 eV. However, because no bare-MXenes have been synthesized, the theoretical predictions usually take functional-MXenes into account. For example,  $Ti_2CO_2$  and  $Ti_2CF_2$  are achieved the value around 0.10 and 0.18 eV, respectively. Gravimetric capacity, diffusion barrier, and volume expansion of Li intercalations into lightweight multilayer MXenes are investigated as described in Table 2.1 (Ashton *et al.*, 2016). Surprisingly, the gravimetric capacitance predictions of  $Ti_2CO_2$  and  $V_2CO_2$  in bilayer form are quite consistent with the experimental values.



**Table 2.1** Theoretical prediction for the LIBs and experimental information.

Material	Theoretical calculations		Experimental data
	Gravimetric capacitance ( $\text{mA}\cdot\text{h}\cdot\text{g}^{-1}$ )	Diffusion barrier by Cl-NEB (eV)	Reversible capacity ( $\text{mA}\cdot\text{h}\cdot\text{g}^{-1}$ )
graphite	372	0.3	350
graphene	-	0.152 <sup>7</sup>	-
$M_2C$ (M: Sc, Ti, V)	400-500 <sup>4</sup>	$\sim 0.015$ (M: Ti) <sup>7</sup>	-
$M_2C$ (M: Zr, Nb, Mo)	200-300 <sup>4</sup>	$\sim 0.020$ - $0.035$ <sup>7</sup>	-
$M_2C$ (M: Hf, Ta)	100-150 <sup>4</sup>	$\sim 0.02$ <sup>7</sup>	-
$\text{Ti}_2\text{CT}_x$ multilayer	-	-	110 <sup>1</sup>
$\text{V}_2\text{CT}_x$ multilayer	-	-	260 <sup>2</sup>
$\text{Nb}_2\text{CT}_x$ multilayer	-	-	170 <sup>2</sup>
$d\text{-Ti}_2\text{CT}_x$	-	-	410 <sup>3</sup>
$d\text{-Ti}_2\text{CO}_2$	350-383 <sup>4,5</sup>	0.18 <sup>7</sup>	-
$d\text{-V}_2\text{CO}_2$	335-367 <sup>4,5</sup>	-	-
$d\text{-Nb}_2\text{C}_2$	233-250 <sup>4,5</sup>	-	-
$\text{Ti}_2\text{CO}_2$ multilayer	192 <sup>6</sup>	0.63 <sup>6</sup>	-
$\text{V}_2\text{CO}_2$ multilayer	276 <sup>6</sup>	0.82 <sup>6</sup>	-

1(Naguib *et al.*, 2012), 2(Naguib *et al.*, 2013), 3(Mashtalir *et al.*, 2013), 4(Eames and Islam, 2014), 5(Xie *et al.*, 2014),

6(Ashton *et al.*, 2016), 7(Zhang *et al.*, 2017)

## 2.4.2 Key development of MXenes as electrode material for LIBs

Theoretical studies can help to identify the most promising properties of materials for LIBs, such as gravimetric capacitance, Li-ion mobility, and calculated voltage. Furthermore, increasing of theoretical gravimetric capacitance for Li-ions are one of the main propose of the future theoretical study. Because of the theoretical gravimetric capacitance is calculated by the number of Li-ions adsorbed on the surfaces, from the binding energy calculation, divided by the formula weights in one unit-cell, the compound with low weight and high adsorption properties will perform high gravimetric capacities. For example, it was found that in terms of theoretical gravimetric capacity, MXenes with low formula weights, e.g.,  $Sc_2C$ ,  $Ti_2C$ ,  $V_2C$  and  $Cr_2C$ , were the most promising among all MXenes. This was also relevant to  $M_2X$  electrodes, which were expected to perform at higher gravimetric capacities than their  $M_3X_2$  and  $M_4X_3$  counterparts. Identically, there are some experiments that have confirmed that the gravimetric capacity for Li-ions of  $Ti_2CT_x$  is more than 50% higher than that of  $Ti_3C_2T_x$  in the same preparation condition. (Naguib *et al.*, 2012; Mashtalir *et al.*, 2013). Moreover, all the O-functional MXenes, where  $M$  is Sc, Ti, V and Cr, was also predicted to be higher capacity among other functional groups, such as F and OH, which feasible for Li-ion storage (Eames and Islam, 2014; Xie *et al.*, 2014).

In the experimental aspect, delamination of any 2D material is necessary for exploring its adsorption properties. The intercalation of surface functionalized  $f-Ti_3CO_2$  MXenes had been found that intercalated by hydrazine, and its co-intercalation with N, N-dimethylformamide, resulted in increases the c-lattice parameters from 19.4 Å to ~30% and ~37%, respectively (Mashtalir *et al.*, 2013). By increasing of interlayer spacing from the delamination process, the performance of the  $f-Ti_3CO_2$  MXenes as anode material in Li-ion batteries show excellent capacity at extremely high charging rates as shown in Figure 2.11. The measurement of the specific capacity of  $d-Ti_3C_2$  obtained a capacity of  $410 \text{ mA}\cdot\text{h}\cdot\text{g}^{-1}$ , which was 4 times higher than that of  $f-Ti_3C_2$ . Therefore, some theoretical works attempt to guide the delamination of multilayers to a single layer, such as the metal-intercalation model, by increasing the interlayer spacing.

On the other hand, in theoretical study, the voltage calculation is commonly used, with a positive result indicating that Li ions intercalation is a desirable reaction

for LIBs. Systematically calculation of the relation between theoretical gravimetric capacity and calculated voltage of  $\text{Li}_2\text{M}_2\text{C}(\text{OH})_2$ ,  $\text{Li}_2\text{M}_2\text{C}(\text{O})_2$ ,  $\text{Li}_2\text{M}_2\text{C}(\text{F})_2$ ,  $\text{Li}_2\text{M}_2\text{CH}_2$ , and  $\text{Li}_2\text{M}_2\text{C}_2$ , where  $M$  is Hf, Ta, Zr, Nb, Mo, Sc, Ti, V, and Cr early transition metal, were reported (Eames and Islam, 2014). As a result, high capacitance was found to be exhibited by Sc, Ti, V, and Cr-based MXenes, whereas the structure composed of F, OH, and H functional groups exhibited a low calculated voltage and was not preferable as an electrode for the LIBs. The charge density difference for  $\text{Ti}_2\text{CH}_2\text{Li}_2$  in Figure 2.13 indicates that the surface cannot acquire large amounts of electron density, which restricts the amount of lithium adsorption atoms on the surface, which relates to an unfavorable voltage of below 0 V as shown in Figure 2.12. Therefore, the most promising group of MXenes that are predicted to have more than  $200 \text{ mA}\cdot\text{h}\cdot\text{g}^{-1}$  and a preferable voltage above 0 V are compounds containing light transition metals, such as Sc, Ti, V, and Cr, with O-functional groups.

In general, the theoretical Li-ion mobility can assure the experimental charging rate in the electrode. Decreases in the diffusion barrier would enhance the Li-ion mobility on the material's surface. For example, in the theoretical prediction as indicated in Figure 2.5(F, G, and H), the applying of the biaxial strain to  $\text{Ti}_2\text{C}$ ,  $\text{Ti}_2\text{CO}_2$  and  $\text{Ti}_2\text{CF}_2$  monolayer as well as decreasing of the  $n$ -ordering of  $M$  transition metal atom results to higher of the Li-ion diffusion barrier. Moreover, it has also been symmetrically observed that the decreasing of the diffusion barriers of the  $\text{V}_n\text{C}_{n+1}\text{O}_2$  MXenes was related to the volume expansion of the unit cell and the raising of the  $n$ -order of  $M$  transition metals. (Ashton *et al.*, 2016). However, electronic structure, for example, the electronic charge state of the system that can be indicative of more physical insight, is still waiting to be investigated.

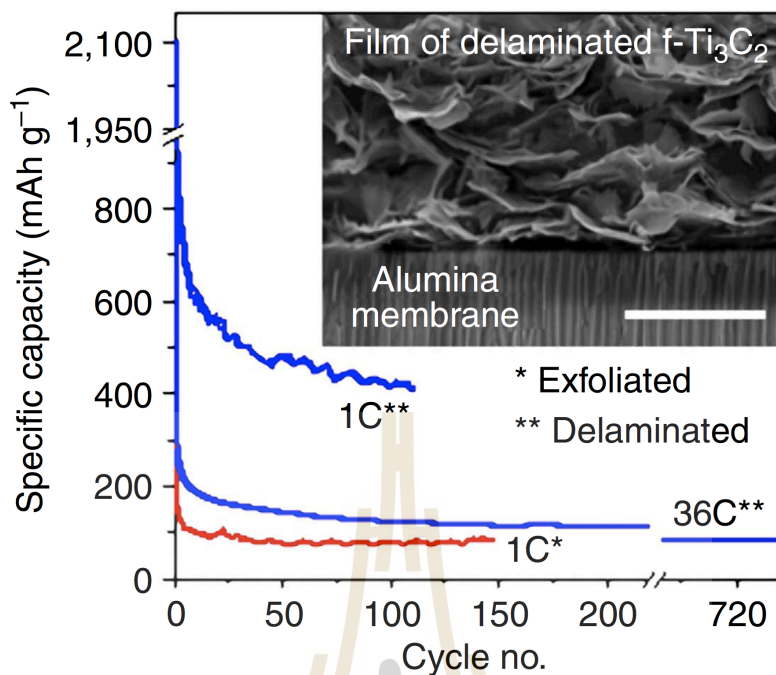


Figure 2.11 presents the specific capacity of exfoliated and delaminated of  $f\text{-Ti}_3\text{C}_2$  where inset shows SEM image of delaminated  $f\text{-Ti}_3\text{C}_2$  film (Mashtalir *et al.*, 2013).

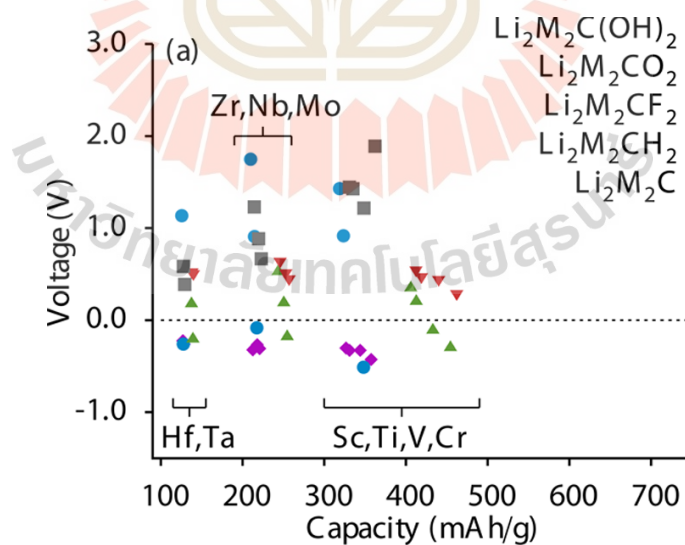
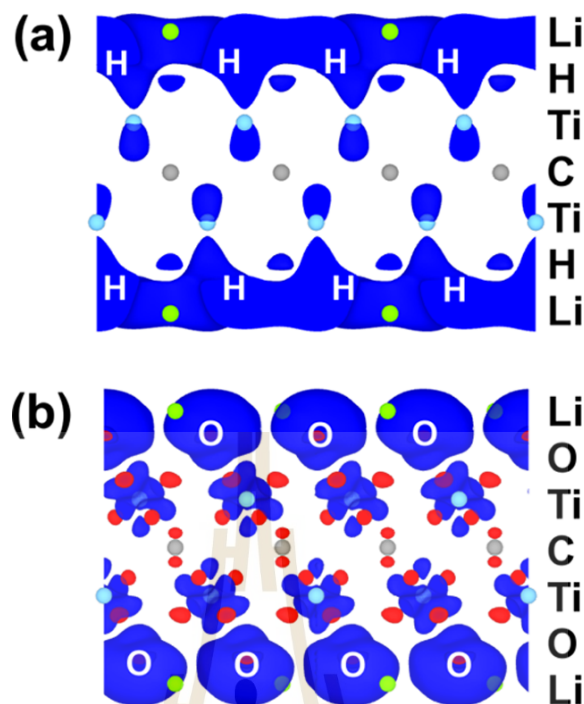


Figure 2.12 indicate systematically calculation of the relation between theoretical gravimetric capacity and calculated voltage of  $\text{Li}_2\text{M}_2\text{C}(\text{OH})_2$ ,  $\text{Li}_2\text{M}_2\text{C}(\text{O})_2$ ,  $\text{Li}_2\text{M}_2\text{C}(\text{F})_2$ ,  $\text{Li}_2\text{M}_2\text{CH}_2$ , and  $\text{Li}_2\text{M}_2\text{C}_2$  where  $M$  is early transition metals (Eames and Islam, 2014).



**Figure 2.13** show Charge density difference after Li intercalation of (a)  $\text{Ti}_2\text{CH}_2$  and (b)  $\text{Ti}_2\text{CO}_2$  where red indicate decreasing of charge density, and dark blue indicate increasing of charge density (Eames and Islam, 2014).

### 2.4.3 Future research perspective for MXenes

From the literature reviews, we found that the tunable structural properties will be importance for the development of the LIBs anode of MXenes. The structural and electronic properties, and Li-ion characteristic of anode materials for LIBs were investigated theoretically in this thesis by altering the  $M$  transition metal carbides with Sc, Ti, V, Nb, or Cr, and including O and F as the functional groups of  $M_2\text{CT}_2$  MXenes. In addition, positions of  $T$  functional atoms of two side in the monolayer of MXenes which will be constructed in many configurations, are considered as the surface modification in these studies. Moreover, we point out all possible configurations the monolayer structure that will later be provided into bilayer configurations in which symmetry and asymmetry in bilayer are presented. The significant of bilayer study may refer to, even though the monolayer can be chosen as the ionic insertion structure, but it is not enough to cover overall effect between two different enclosed layer and the ionic insertion.

## 2.5 Research Objectives

- In this research, we would like to study the structural and electronic properties of MXenes from a theoretical perspective.
- Beyond the monolayer-structure, to investigate the variety of structural configurations from their surface combinations, we will further investigate the bilayer-structures of the selected compounds of MXenes family for Li-ions battery application. Moreover, the electronic properties will be performed in the systems.
- We will address intercalation with alkali metals and transition metals, and charge impurities on to the selected MXenes by mainly focus on a tendency of the structural and electronic properties.
- Other properties (such as structural parameters, formation energy, density of states, band structure, *etc.*) that can be compared with experiments will be calculated as well.

## 2.6 Scope and Limitations of the Study

This research will cover the theoretical study of selected transition metal carbide compounds, especially Sc, Ti, V, Cr, and Nb based transition metals with the oxygen and fluorine surface functional groups provided as  $M_2CT_2$  for both monolayer and bilayer structure. Using first-principles calculations based on DFT, the metals (Li, Be, Mg, Ca, Na, and K atoms) and non-metal (such as sulfur atom) intercalated into the selected bilayer system are simulated. The electronic and ionic mobility properties of MXenes systems with and without intercalation will be investigated. The calculations will employ GGA exchange correlations and the DFT-D3 method of Grimme to treat properly the van der Waals interaction. It is widely known that DFT calculations yield precise mechanical characteristics and reliable total energy outputs. However, the many-body interaction approximation causes the electronic band structure utilizing the Perdew-Burke-Ernzerhof (PBE) version of the generalized gradient approximation (GGA) for the exchange-correlation functional to be undervalued.

## 2.7 Expected Results

We expect that different structural configurations of the selected MXenes will indicate a significant feature of electronic properties. On the other hand, we expect that some intercalation atoms inserted into the material will improve the diffusion properties of Li-ion. As a result, we hope that this work will provide useful information about the properties of 2D materials and encourage the development of next-generation energy storage devices.



## CHAPTER III

### THEORETICAL BACKGROUND

Advanced computational systems and highly developed computational techniques open an opportunity to study many physical and chemical properties of various materials. The “first-principles calculations” or “*ab initio* calculations” based on quantum mechanical calculations and density functional theory (DFT) are the theoretical methods for investigating physical and chemical properties of materials (Kresse and Hafner, 1993). Without taking any parameters from experiment in calculations except some fundamental information such as the number of atoms in the systems *etc.*, DFT calculations allow one to obtain many properties of materials. Therefore, this chapter provides an overview of theoretical research and the historical timeline used to develop DFT. Based on Quantum mechanics, the many bodies problem and their interactions are also introduced. Furthermore, DFT that was developed to simplify electron interactions in terms of exchange-correlation, hence reducing the complexity of electron interactions are also included.

#### 3.1 Many-body problem and Schrödinger equation

Basically, physics of condensed matter could be obtained from the interactions of positively charged nucleus and negatively charged electrons. Quantum mechanics is the branch of physics that describes the interactions between nuclei and electrons. The quantum mechanical wave function of the Schrödinger equation, which governs the dynamics of a time-independent non-relativistic system, can be used to derive the matter characteristics of any system (Schrödinger, 1926). In the hydrogen atom system, the simplest example of the Schrödinger equation is as follows:

$$\left[ -\frac{\hbar^2}{2m} \nabla^2 - \frac{e^2}{4\pi\epsilon_0 r_1} \right] \psi(r_i) = E\psi(r_i), \quad 3.1$$

Where  $-\frac{\hbar^2}{2m}\nabla^2$  is the kinetic energy of the electron,  $-\frac{e^2}{4\pi\epsilon_0r_1}$  is the potential due to the nucleus and  $\psi(r_i)$  is the electron wave function (probability distribution of electron position), and  $E$  is the total energy of the electron. A single electron and a nucleus are separated by the distant  $r_i$ . There are multiple solutions, each defined by the set of quantum numbers: the principle quantum number ( $n$ ), the orbital angular momentum number ( $l$ ) and the magnetic quantum number ( $m_l$ ) in terms of wave function  $\psi_{nlm_l}(r, \theta, \phi)$ . When the equation is extended to the Helium atom system, it becomes more complicated. Because Helium has two electrons and one nucleus, the Hamiltonians for the first and second electrons can be split, resulting in the following Schrödinger equation:

$$[H_1 + H_2 + W]\psi(r_1, r_2) = E\psi(r_1, r_2), \quad 3.2$$

We have three distance to consider  $r_1$ ,  $r_2$ , and  $r_{12}$  (distance between the two electrons).  $W$  is the cross term between them and the operator can be spelled out as

$$\left[ -\frac{\hbar^2}{2m}\nabla_1^2 - \frac{e^2}{4\pi\epsilon_0r_1} - \frac{\hbar^2}{2m}\nabla_2^2 - \frac{e^2}{4\pi\epsilon_0r_2} + -\frac{e^2}{4\pi\epsilon_0r_{12}} \right] \psi(r_1, r_2) = E\psi(r_1, r_2), \quad 3.3$$

where  $-\frac{e^2}{4\pi\epsilon_0r_{12}}$  is the problem that comes in. We must consider the interaction between two electrons.

In fact, we cannot simply solve this equation analytically. In general form, the full multi-electron and multi-nucleus Schrödinger equation for a N-atom and n-electron is defined as

$$H\psi(R_1, \dots, R_M; r_1, \dots, r_N) = E(R_1, \dots, R_M)\psi(R_1, \dots, R_M; r_1, \dots, r_N). \quad 3.4$$

The wave function can be written in terms of  $R_1, \dots, R_M$  and  $r_1, \dots, r_N$  which are the positions of nuclei and electrons, respectively. The Hamiltonian is given by

$$H = \left[ -\sum_{i=1}^N \frac{\hbar^2}{2M_i} \nabla_{R_i}^2 + \frac{1}{2} \sum_{i=1}^N \sum_{j<1}^N \frac{Z_i Z_j e^2}{|R_i - R_j|} - \sum_{i=1}^N \frac{\hbar^2}{2m_i} \nabla_{r_i}^2 + \sum_{i=1}^N \sum_{j=1}^N \frac{Z_i e^2}{|R_i - r_j|} + \frac{1}{2} \sum_{i=1}^N \sum_{j<1}^N \frac{e^2}{|r_i - r_j|} \right]. \quad 3.5$$

Here, the first term is the kinetic energy of the ions, the second term is the potential energy of the ions, the third term is the kinetic energy of the electrons, the fourth term is electron-ion interactions, and the last term is electron-electron interactions.

## 3.2 Density functional theory

It is a challenge task for calculation due to large number of atoms and even larger number of electrons. The density functional theory (DFT) based on Kohn-Sham equations (Kohn and Sham, 1965) introduced to reduce the complication of the interactions between electrons by simplifying the electrons interactions in term of exchange-correlation.

### 3.2.1 Born-Oppenheimer Approximation

The Born-Oppenheimer approximation (Born and Oppenheimer, 1927) is based on the assumption that the electrons in a system move on a much faster time scale than the much heavier nuclei, and thus they adjust their positions “instantaneously” in response to such atomic motion. This simplifies the Schrödinger equation to a multi-electron equation in the presence of a potential due to fixed atomic nuclei  $\mathbf{R}_i$ . The Hamiltonian of the system from Eq. 3.5 can be written as:

$$H = \left[ -\frac{\hbar^2}{2m} \sum_{i=1}^N \nabla_{r_i}^2 + \sum_{i=1}^N \sum_{j=1}^N \frac{Z_i e^2}{|\mathbf{R}_i - \mathbf{r}_j|} + \frac{1}{2} \sum_{i=1}^N \sum_{j < i}^N \frac{e^2}{|\mathbf{r}_i - \mathbf{r}_j|} \right] \quad 3.6$$

However, according to Eq. 3.6, a  $3N$ -dimensional problem has to be solved, where  $N$  is the total number of electrons in the system. We still need to figure out a good way to account these interactions within the system. If we try to solve the many body problems numerically, we still quickly run into trouble and waste on computational time. The Density functional theory (DFT) finally came along that was formulated by Walter Kohn who won the Nobel Prize in 1998 (Kohn and Sham, 1965). Basically, the density functional theory (DFT) mentions that working with the wave functions with  $3N$  variables is very complicated. Ideally, in the ground state, all aspects of the electronic structure of the interacting electrons system in an “external” potential, due to the nuclei, are determined by electron density  $\rho(\mathbf{r})$  which can be written as:

$$\rho(r) = \sum_i^N |\psi_i(r)|^2, \quad 3.7$$

where  $N$  is the total number of electrons in the system.

### 3.2.2 The Hohenberg-Kohn theorem

The two basic theorems of the Hohenberg-Kohn theorem are:

- The first Hohenberg-Kohn (Hohenberg and Kohn, 1964) theorem establishes that for any external potential, there is a unique ground state electronic density.
- This implies that the ground state electronic density determines all the properties of the system.

The first Hohenberg-Kohn theorem can be proven by supposing that there are two potentials, differing by more than a constant, that yield the same ground state density.

The expectation value of the energy is defined as

$$E = \langle \psi | H | \psi \rangle = \int \psi^*(r) H \psi(r) dr. \quad 3.8$$

Assume that two external potentials (two Hamiltonians) with the same ground state charge density  $\rho_0(r)$  are written as:

$$E_0 = \langle \psi | H | \psi \rangle \quad 3.9$$

and

$$E'_0 = \langle \psi' | H' | \psi' \rangle. \quad 3.10$$

From the variational principle (Sakurai, 1994), if the expectation value of the energy for a given Hamiltonian is computed operating on the wave function which is not the ground state, an energy value greater than the ground state energy will always be received. From Eq. 3.9 and 3.10, can be denoted as:

$$E_0 < \langle \psi' | H | \psi' \rangle \quad 3.11$$

and

$$E'_0 < \langle \psi | H' | \psi \rangle \quad 3.12$$

By substituting  $H = H' + (H - H')$  and  $H' = H + (H' - H)$  back into Eq. 3.11 and 3.12 then we get

$$E_0 < E'_0 + \langle \psi' | H - H' | \psi' \rangle \quad 3.13$$

and

$$E'_0 < E_0 + \langle \psi | H' - H | \psi \rangle \quad 3.14$$

It can be concluded that  $E_0 + E'_0 < E_0 + E'_0$ , which is obviously false.

The second Hohenberg-Kohn theorem can be proven by showing that this leads to a contradiction involving the expectation values of the energy. The DFT theorem implies that we can determine the ground state energy  $E_0$  of an interacting electron system in terms of the charge density,  $\rho(\mathbf{r})$ . The energy functional can be defined as

$$E[\rho(\mathbf{r})] = T_s[\rho(\mathbf{r})] + \int V_{ext}(\mathbf{r})\rho(\mathbf{r})d\mathbf{r} + \frac{e^2}{2} \int \frac{\rho(\mathbf{r})\rho(\mathbf{r}')}{|\mathbf{r}-\mathbf{r}'|} d\mathbf{r}d\mathbf{r}' + E_{xc}[\rho(\mathbf{r})], \quad 3.15$$

where  $T_s[\rho(\mathbf{r})]$  is the kinetic energy of a homogeneous non-interacting electron gas,  $\int V_{ext}(\mathbf{r})\rho(\mathbf{r})d\mathbf{r}$  is the energy due to the external potential,  $\frac{e^2}{2} \int \frac{\rho(\mathbf{r})\rho(\mathbf{r}')}{|\mathbf{r}-\mathbf{r}'|} d\mathbf{r}d\mathbf{r}'$  is the Hartree energy, and  $E_{xc}[\rho(\mathbf{r})]$  is the exchange-correlation energy. The exchange correlation energy basically includes all the stuff. Therefore, it can be concluded that the interesting part of the kinetic energy is included in the exchange energy which is related to the Pauli exclusion principle (Pauli, 1925). Moreover, it also includes the correlation energy, which is related to Coulomb repulsion, and overall spin and symmetry in the system. Finally, it also includes the self-interaction correction.

### 3.2.3 Kohn-Sham equations

To find the wavefunctions that minimizing the total energy, the variational principle must be performed. A functional derivative lead to the Kohn-Sham equations (Kohn and Sham, 1965) can be written as

$$\left[ -\frac{\hbar^2}{2m} \nabla^2 + V_{ext}(\mathbf{r}) + V_H(\mathbf{r}) + V_{xc}(\mathbf{r}) \right] \psi_i(\mathbf{r}) = \varepsilon_i \psi_i(\mathbf{r}), \quad 3.16$$

where  $\psi_i(\mathbf{r})$  and  $\varepsilon_i$  are the single-electron Kohn-Sham orbitals and energies respectively. We must solve  $N$  single-electron equations for non-interacting electrons in an effective potential due to the nuclei and the other  $N-1$  electrons.

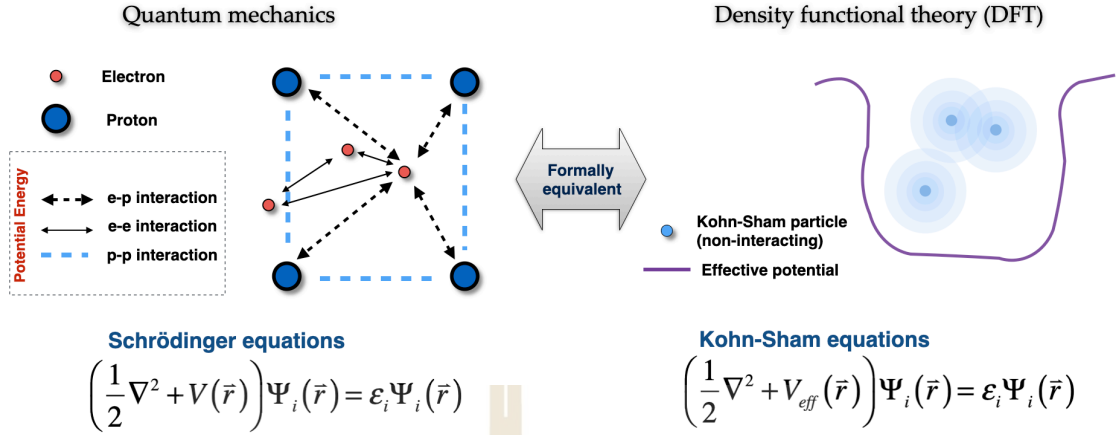


**Figure 3.1** Illustration of the formal equivalence between the density functional theory (DFT) and the traditional quantum mechanics.

### 3.2.4 The exchange-correlation energy

In principle, DFT is an exact formulation with no approximations. One can find exact solutions to the Schrödinger equation if one knows the form of the potential:

$$V = V_{ext}(r) + \frac{e^2}{2} \int \frac{\rho(r')}{|r-r'|} dr' + V_{XC}[\rho(r')] \quad 3.17$$

where  $V_{ext}(r)$  is the “external” potential generated by nuclei acting on the electron. Unfortunately, we do not know the exact value of  $V_{XC}[\rho(r)]$  which can be defined as

$$V_{XC}[\rho(r)] = \frac{\delta E_{XC}[\tilde{\rho}(r)]}{\delta \tilde{\rho}(r)} \Big|_{\tilde{\rho}(r)=\rho(r)} \quad 3.18$$

The Kohn-Sham equations (Kohn and Sham, 1965) from Eq. 3.16 can be written with the ground state energy  $E$  as

$$E = \sum_{j=1}^N E_j + E_{XC}[\rho(r)] - \int V_{XC}(r)\rho(r)dr - \frac{1}{2} \frac{\rho(r)\rho(r')}{|r-r'|} drdr' \quad 3.19$$

If  $E_{XC}[\rho(r)]$  and  $V_{XC}(r)$  are neglected, the Kohn-Sham equations are reduced to the self-consistent Hartree equations. In addition, the Many-body effects are already included in  $E_{XC}$  and  $V_{XC}$ . In practice, the main approximations for exchange correlation energy  $E_{XC}[\rho(r)]$  are listed in following (Calais, 1993). The most

commonly used approximations based on DFT are the local density approximation (LDA) (Ceperley and Alder, 1980) and/or generalized gradient approximation (GGA) (Perdew *et al.*, 1996). Alternatively, hybrid functionals constructed by mixing Hartree-Fock (HF) exact exchange energy (Becke, 1993) generally provide better accuracy for band structure and total energy but the methods are more computationally intensive than LDA or GGA (Hafner, 2008).

#### a. The Local Density Approximation (LDA)

The local density approximation (LDA) computes the exchange-correlation energy for a more simplified system than the actual one. It is a good approximation if the charge density does not change very rapidly in the system. The exchange-correlation energy can be written as

$$E_{XC}^{LDA}[\rho(r)] = \int \rho(r) \varepsilon_{XC}^{LDA} \rho(r) dr, \quad 3.20$$

where  $\varepsilon_{XC}^{LDA} \rho(r)$  is the exchange-correlation energy per particle of uniform electron gas of density  $\rho(r)$ . The exchange-correlation energy can be defined as:

$$\varepsilon_{XC}^{LDA}(n) = \varepsilon_X^{LDA}(n) + \varepsilon_C^{LDA}(n) \quad 3.21$$

where  $\varepsilon_X^{LDA}(n)$  and  $\varepsilon_C^{LDA}(n)$  are the exchange energy and correlation energy per particle respectively. Dirac's expression (Dirac and Fowler, 1926) can be used to define the exchange energy as

$$\varepsilon_X(n) = -\frac{3}{4} \left( \frac{3}{\pi} \right)^{\frac{1}{3}} n^{\frac{1}{3}} = -\frac{0.458}{r_s} a.u. \quad 3.22$$

The correlation part was estimated by Wigner (Wigner, 1934) as

$$\varepsilon_C(n) = -\frac{0.44}{r_s + 7.8} a.u. \quad 3.23$$

where  $r_s$  is the mean interelectronic distance expressed in atomic unit which is defined as  $r_s = \left( \frac{3}{4\pi n} \right)^{1/3}$ .

#### b. The Generalized Gradient Approximation (GGA)

The generalized gradient approximation is used to improve the LDA. By expanding  $E_{XC}$  as a series in terms of the density and its gradient  $|\nabla\rho(r)|$ , the inhomogeneity of density is also considered. This approach is known as gradient expansion. The exchange-correlation energy can be written in the following form:

$$E_{xc}[n] = \int \rho(r) \varepsilon_{xc}[\rho(r)] F_{xc}[\rho(r), \nabla \rho(r), \nabla^2 \rho(r), \dots] dr, \quad 3.24$$

Where  $F_{xc}[\rho(r), \nabla \rho(r), \nabla^2 \rho(r), \dots]$  is the function's factor for modifying LDA expressions according to the density variation at the considered point. The negativity of the exchange density can remarkably improve the quality of exchange energy. A modified gradient has been proposed, for instance, BLYP (Becke, 1988), PW91 (Perdew *et al.*, 1992), and PBE (Perdew *et al.*, 1996). Perdew, Burke, and Ernzerhof (PBE) presented a simplified construction, in which all parameters are fundamental constants.

$$F_X^{PBE}(s) = 1 + \kappa - \frac{\kappa}{1 + \frac{\mu s^2}{\kappa}}, \quad 3.25$$

where  $\mu = 0.21951$ ,  $\kappa = 0.804$ ,  $F_X^{PBE}(s)$  is the PBE exchange enhancement factor,  $s = |\nabla \rho(r)| / (2k_F \rho(r))$  is the exchange dimensionless reduced density gradient, and  $k_F = (3\pi^2 \rho(r))^{1/3}$ .

### 3.3 Projector augmented waves

In 1994, Blöchl (Blöchl, 1994) proposed the projector augmented waves (PAW) to create a smooth wavefunctions ( $\tilde{\Psi}$ ) by the transformation operator ( $\tau$ ) which made a linear transformation relating between all electron wave function ( $\Psi$ ) to the smooth wave function defined as:

$$|\Psi\rangle = \tau |\tilde{\Psi}\rangle. \quad 3.26$$

The whole electron wavefunction ( $\Psi$ ) can be written as:

$$|\Psi\rangle = |\tilde{\Psi}\rangle + \sum_m (|\Psi_m\rangle - |\tilde{\Psi}_m\rangle) \langle \tilde{p}_m | \tilde{\Psi} \rangle \quad 3.27$$

where  $\Psi_m$  is a localized all electron partial wave for state  $m$ ,  $\tilde{\Psi}_m$  is a localized smooth partial wave for state  $m$ , and  $\langle \tilde{p}_m |$  is the localized projection operator. The transformation operator ( $\tau$ ) can be written as:

$$\tau = 1 + \sum_m (|\Psi_m\rangle - |\tilde{\Psi}_m\rangle) \langle \tilde{p}_m |. \quad 3.28$$

The transformation operator can be used to add back the core potential of all electron wave functions to the smoothed wavefunctions. Additionally, the equation can be

applied equally well to core and valence states so that applying this equation to all electron state can derive all electron results (Martin, 2004).

### 3.4 Plane waves

The Blochl's theorem presented the plane waves (PWs) or the Blochl wave functions for the solutions of the Kohn-Sham equation. The plane waves are given by

$$\Psi_{nk}(\mathbf{r}) = e^{i\mathbf{k}\cdot\mathbf{r}} U_{nk}(\mathbf{r}), \quad 3.29$$

The wave functions in terms of  $e^{i\mathbf{k}\cdot\mathbf{r}}$ , times a function of periodic function,  $U_{nk}(\mathbf{r})$  (Kittel, 1982). The periodic part of the wave function can be expanded in term of a special set of plane wave:

$$U_{nk}(\mathbf{r}) = \sum_G c_G e^{i\mathbf{G}\cdot\mathbf{r}}, \quad 3.30$$

where  $e^{i\mathbf{G}\cdot\mathbf{r}}$  is the plane wave basis set, the summation is over the reciprocal lattice vectors (giving by  $\mathbf{G} = m_1\mathbf{b}_1 + m_2\mathbf{b}_2 + m_3\mathbf{b}_3$  for all integers  $m_i$ ). This means that solving for  $\Psi_{nk}(\mathbf{r})$  at each point in  $k$ -space requires the summation over an infinite number of  $\mathbf{G}$  vectors. Combining these two equations gives:

$$\Psi_{nk}(\mathbf{r}) = \sum_G c_{k+G} e^{i(\mathbf{k}+\mathbf{G})\cdot\mathbf{r}} U_{nk}(\mathbf{r}), \quad 3.31$$

The function  $e^{i(\mathbf{k}+\mathbf{G})\cdot\mathbf{r}}$  are solutions of the Schrödinger equation and the lower energy solutions are more physically relevant than very high energy solutions. Therefore, the reciprocal lattice vectors are included only that lead to solutions with kinetic energy less than some cutoff energy which defines as

$$\frac{\hbar^2}{2m} |\mathbf{k} + \mathbf{G}|^2 < E_{cutoff}. \quad 3.32$$

### 3.5 Pseudo wavefunction and Pseudopotential

The atomic orbitals are calculated by employing the single particle's, the Kohn-Sham equations, and the wave functions, then the energy for all electron orbitals of the atomics are obtained. This is called "all electron calculation". However, performing all electron calculation for larger systems is very expensive. The wavefunctions for the lower energy states, e.g., 1s, are spatially localized closer to the nucleus while having larger amplitude away from the nucleus for the valence states. All the wave functions

also have sharper features closer to the nucleus. The sharper feature in the wave functions requires many planes to represent. If the wave function is removed near the cutoff radius, ( $r_c$ ) from the nucleus, the wavefunction will have a very smooth behavior, which can be represented by a few planewaves and the pseudowavefunction. This method yields a result that exactly matches with the all electron wave function (Heine, 1970). The pseudopotential approximation basically has two main parts. The first part only treats the valence electrons explicitly and the second part treats nucleus plus core electrons which produces an effective or “pseudo” potential. The pseudopotential matches exactly with the core potential in larger range than the cutoff radius as shown in Figure 3.2.

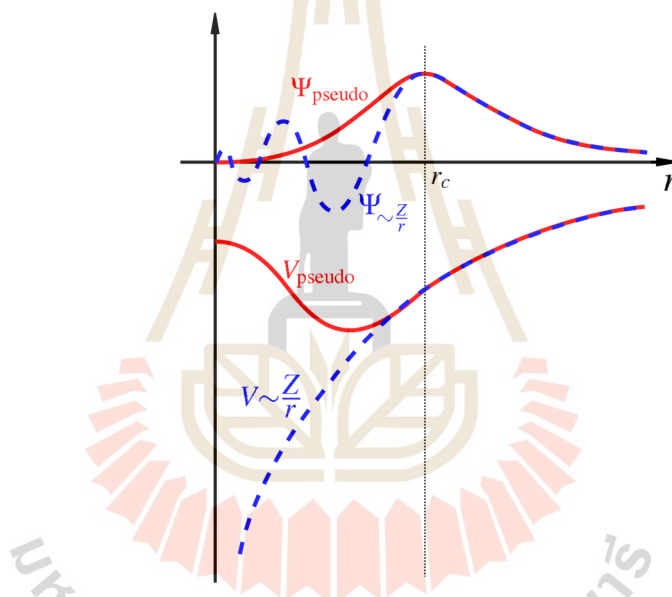


**Figure 3.2** Schematic illustrations of comparison of a wavefunction in the Coulomb potential of the nucleus (dashed blue) to the one in the pseudopotential (solid red). Above of the certain cutoff radius  $r_c$  represents a radius that the real and the pseudo wavefunction and potentials match (Quester, 2006).

### 3.6 Van der Waals approximation

In some cases, static density functional theory using LDA and GGA fail to describe the structural properties of materials, especially for layered materials, due to long-range dispersion interactions, generally denoted as van der Waals (vdW) interactions between atoms and molecules. The vdW correction to GGA that are

proposed by Grimme, introduces the dispersion force field parameters to the conventional DFT, so called the DFT-D3 method (Grimme *et al.*, 2010), are, therefore, importance role for the studies of layered material properties. The total energy is obtained by adding the term  $E_{Disp}$  to the DFT interaction energy as

$$E_{tot} = E_{DFT} + E_{Disp} \quad 3.33$$

where  $E_{DFT}$  is the DFT interaction energy estimated using an approximation exchange correlation function, and  $E_{Disp}$  is the dispersion energy specified for periodic systems as two-body interactions, as seen in the equation below.

$$E_{Disp} = - \sum_{i=1}^N \sum_{j=i+1}^N \left( f_{d,6}(r_{ij}) \frac{C_{6ij}}{r_{ij}^6} + f_{d,8}(r_{ij}) \frac{C_{8ij}}{r_{ij}^8} \right) \quad 3.34$$

where  $r_{ij}$  denote the distance between atom  $i$  and atom  $j$ , and the summations apply to all  $N$  atoms and all  $L = (l_1, l_2, l_3)$  unit cell translations.  $C_{6ij}$  and  $C_{8ij}$  specify the dispersion coefficient for the atom pair  $ij$  that are geometry-dependent, as they are changed around atoms  $i$  and  $j$  based on local geometry (coordination number). Parameters  $C_{6ij}$  can be calculated by  $C_{nij} = \sqrt{C_{ni}C_{nj}}$ .  $f_{d,n}(r_{ij})$  is a damping function that scales the force field so that contributions from interactions within typical bonding distances are minimized. In practice, the parts in the  $E_{Disp}$  equation relating to interactions over distances greater than a specified cutoff radius contribute only a tiny portion to  $E_{Disp}$  and can be neglected. The DFT-D3 approach employs damping of the following equation.

$$f_{n,6}(r_{ij}) = \frac{s_n}{1 + 6 \left( r_{ij} / (s_{R,n} R_{0ij}) \right)^{-\alpha_n}} \quad 3.35$$

where  $R_{0ij} = \sqrt{\frac{C_{8ij}}{C_{6ij}}}$ , and the parameters  $\alpha_6$ ,  $\alpha_8$ ,  $s_{R,8}$ ,  $s_6$  are fixed at values of 14., 16., 1., and 1., respectively. The values of  $s_8$  and  $s_{R,6}$  are variable parameters that are defined by the exchange-correlation functional employed.

## CHAPTER IV

### RESEARCH METHODOLOGY

Based on the approximations in the previous chapter, the Kohn-Sham equations can be solved. The solutions provide the ground state electronic wavefunctions, electronic structure, and total energy, *etc.* These solutions enable one to calculate the measurable quantities of material, such as lattice constant, band structure, electronic structure, density of states, and so on, allowing whether prediction or direct comparison that are in good agreement with experiment. The approach and details of the calculations performed using DFT calculations are described in this chapter.

#### 4.1 Vienna ab initio simulation package (VASP)

The first principles calculations will be performed by employing the projector augmented-wave (PAW) (Blöchl, 1994; Kresse and Joubert, 1999) method as implemented in the Vienna *ab initio* simulation package (VASP). Based on DFT, the GGA functional will be used with the parameterization of Perdew, Burke, and Ernzerhof (PBE) exchange-correlation function (Perdew *et al.*, 1996). The vdW interactions, which have been effectively employed to layered structures, such as graphene and layered MXenes, and are rectified using Grimme's DFT-D3 approach, can be incorporated in the VASP (Grimme, 2006; Yarifard *et al.*, 2016; Grimme *et al.*, 2010). The VASP uses self-consistent scheme to optimize wavefunctions as shown in the flowchart of Figure 4.1. After providing the atomic positions and calculation conditions as inputs, the self-consistent iterative minimization begins with trial charge density ( $\rho_{in}$ ) and trial wavefunctions ( $\phi_n$ ), that are generated by assuming from atomic orbitals on each atom. Hence, the input charge density and wavefunctions are independent quantities. Within each self-consistent loop, the charge density is used to set up the Hamiltonian. The effective potential and the energy of the system with the input charge density is calculated where the new charge density can further be obtained by solving the Kohn-

Sham equation. Furthermore, the mixing of the new and previous charge densities will be utilized to calculate new energy that may be compared to the old energy. If the energy difference ( $\Delta E$ ) is smaller than the specified accuracy by setting this energy value in the INCAR file, iteration is completed and the optimized energy, force, equilibrium volume, and so on are obtained.

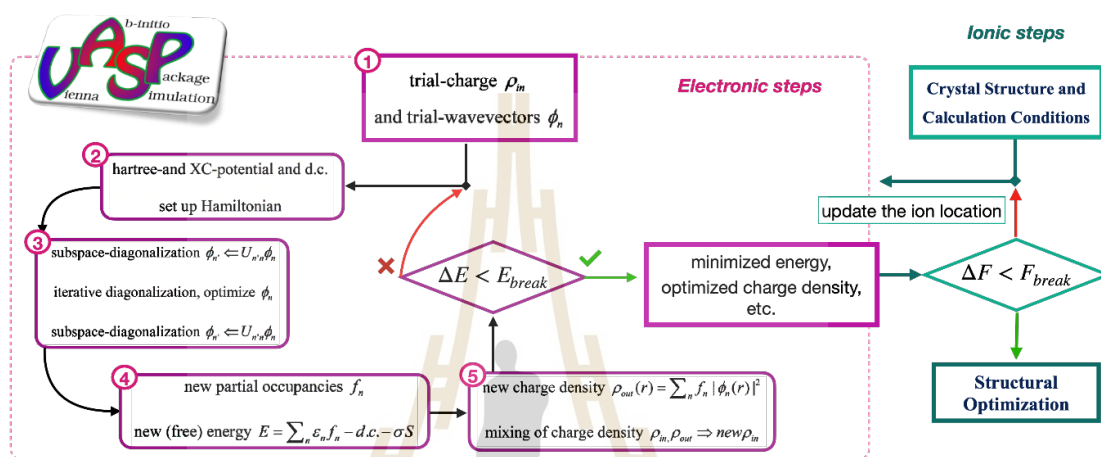


Figure 4.1 The self-consistent scheme used in the VASP code.

## 4.2 Structural optimization

General structure of MXenes has hexagonal unit cell with two equal axes ( $a$  and  $b$ ) and a height ( $c$ ) perpendicular to the base axes. In this research, equilibrium volume of pristine MXenes intercalated with alkali metals such as Li, Na, K and Rb will be determined by fitting total energy as a function of volume with Rose–Vinet isothermal equation of state (Vinet *et al.*, 1989). After that, the ground state wavefunctions of the relaxed structures can then be used to calculate the electronic structure, density of states, and so on.

### 4.2.1 Equation of state

The solid equation of state (EOS) specifies the correlation between thermodynamic variables of compressed solids and is used to investigate thermodynamic properties of materials. To describe the EOS, many empirical relationships have been presented. The Birch–Murnaghan isothermal equation of state

which is a relationship between the volume of a body and the pressure to which it is subjected (Murnaghan, 1944; Birch, 1947). Initially, the definition of the energy of a compressed system as a Taylor series based on the finite strain is given by

$$E(f) = a + bf + cf^2 + \dots \quad 4.1$$

where  $f$  is a finite strain specified by

$$f = \frac{1}{2} \left[ \left( \frac{V_0}{V} \right)^{2/3} - 1 \right]. \quad 4.2$$

In the above equation,  $V_0$  is the equilibrium volume of the system. The pressure and bulk modulus are respectively defined as

$$P = - \frac{\partial E}{\partial f} \cdot \frac{\partial f}{\partial V}, \quad 4.3$$

$$B = -V \left( \frac{\partial P}{\partial f} \cdot \frac{\partial f}{\partial V} \right). \quad 4.4$$

The second order of the equation 4.3 gives

$$P = \frac{3B_0}{2} \left[ \left( \frac{V_0}{V} \right)^{7/3} - \left( \frac{V_0}{V} \right)^{5/2} \right] \quad 4.5$$

The isothermal bulk modulus ( $B_0$ ) and pressure derivative of the bulk modulus ( $B'_0$ ) are further performed by

$$B_0 = -V \left( \frac{\partial P}{\partial f} \cdot \frac{\partial f}{\partial V} \right)_{P=0} \quad 4.6$$

$$B'_0 = \left( \frac{\partial B}{\partial P} \right)_{P=0}. \quad 4.7$$

The third-order Birch–Murnaghan isothermal equation of state is given by

$$P(V) = \frac{3B_0}{2} \left[ \left( \frac{V_0}{V} \right)^{7/3} - \left( \frac{V_0}{V} \right)^{5/2} \right] \left[ 1 + \frac{3}{4} (B'_0 - 4) \left[ \left( \frac{V_0}{V} \right)^{2/3} - 1 \right] \right] \quad 4.8$$

The internal energy is found by integration of the pressure:

$$E(V) = E_0 + \frac{9V_0 B_0}{16} \left\{ \left[ \left( \frac{V_0}{V} \right)^{2/3} - 1 \right]^3 B'_0 + \left[ \left( \frac{V_0}{V} \right)^{2/3} - 1 \right]^2 \left[ 6 - 4 \left( \frac{V_0}{V} \right)^{2/3} \right] \right\}. \quad 4.9$$

In this work, Rose–Vinet equation of state, that is a modification on the Birch–Murnaghan isothermal equation of state, have been generally used for the studies (Vinet *et al.*, 1987). The approach explains how the equation only involves four inputs: the isothermal bulk modulus, the derivative of bulk modulus with respect to pressure,

volume, and thermal expansion, all of which are assessed at zero pressure and at a single temperature. The same equation can be applied to all solid's classes and a wide range of temperatures. By giving the volume's cube root as

$$\eta = \left( \frac{V}{V_0} \right)^{1/3}, \quad 4.10$$

the equation of state is

$$P = 3B_0 \left( \frac{1-\eta}{\eta^2} \right) e^{\frac{3}{2}(B_0^{-1})(1-\eta)}. \quad 4.11$$

### 4.3 Electronic properties

The electronic structures are calculated along the high symmetry points in the first Brillouin zone (BZ). However, Bloch theorem (Bloch, 1929) which is used in DFT calculations builds upon the translational symmetry of the periodic crystal systems. A problem arises in the practical use of DFT calculations whenever we encounter with systems which the original translational symmetry is broken. Therefore, we must employ large supercells whose size determines the periodicity of the band structure through the Bloch theorem. This results in a smaller Brillouin zone compared with the Brillouin zone of primitive cell.

A self-consistent solution to the Kohn-Sham equations results in many Kohn-Sham orbitals and the corresponding Kohn-Sham energies (one-electron eigenvalues) for the set of  $k$ -points. By grouping them according to their orbitals, we can construct two very important pieces of information: band structure and density of state (DOS). A band structure displays the electronic states only along lines of high symmetry in the irreducible Brillouin zone (IBZ), while a DOS diagram collects electron states in the whole BZ. DOS provides the distribution of electronic states in  $k$ -space in terms of energy and is defined as the number of states at each energy interval that are available to be occupied in a band  $n$  given by

$$\rho(\varepsilon) = 2 \sum_k \delta[\varepsilon - \varepsilon_n(k)]. \quad 4.12$$

A high DOS at a specific energy level therefore means that there are many states available for occupation. If we integrate the DOS up to the Fermi energy, it becomes the number of electrons in the system

$$n = \int_0^{\epsilon_F} \rho(\epsilon) d\epsilon. \quad 4.13$$

In practice, the DOS calculation is composed of two steps including ground state calculation and static self-consistent calculation as show in Figure 4.2. The ground state is calculated by self-consistency to get the wave function, the charge density, and the magnetic properties. Before the calculation of the ground state, right parameters for the material system such as exchange correlation functional, k-points and the partial occupancies ( $f_n$ ) need to be performed. In the second step, in order to plot DOS with high resolution and more accuracy, the grids in k space (number of k-points) is increased and the partial occupancies ( $f_n$ ) is changed to tetrahedron method with Blöchl corrections (Blöchl *et al.*, 1994). After that, the charge density from the ground state calculation will be performed after 1 iteration loop of the calculation (static self-consistency or no Ionics updated).

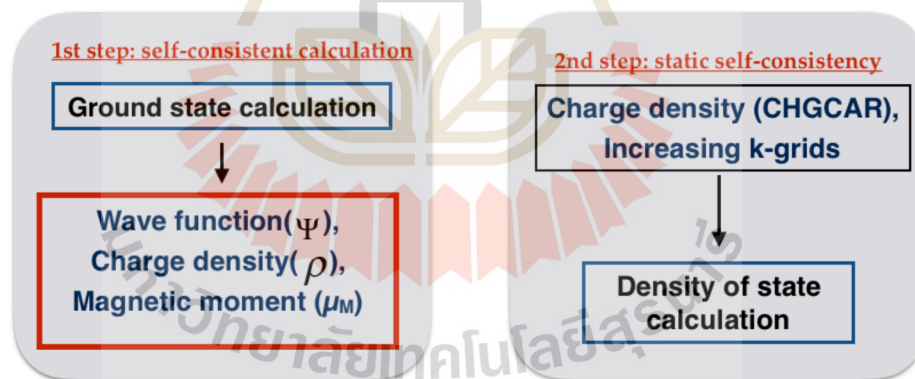


Figure 4.2 The calculation procedure of DOS.

## CHAPTER V

### STRUCTURAL AND ELECTRONIC PROPERTIES OF $M_2CT_2$ ( $M = \text{Sc, Ti, V, Nb, AND Cr; } T = \text{O AND F}$ ) MONOLAYERS

In this chapter presents the theoretical results and discussion for first principles study of structural and electronic properties for monolayer MXenes of  $M_2CT_2$  ( $M = \text{Sc, Ti, V, Nb, Cr and } T = \text{O, F}$ ). The equilibrium lattice parameters, total energy, and formation energy are included in the structural properties part. Moreover, the density of states for different forms of monolayer's surfaces is investigated. The excellent correlation between DOS, formation energy and layer thickness has also been explored in discussion.

#### 5.1 Structural properties

The monolayer structure of the  $M_2XT_2$  MXenes ( $M = \text{Sc, Ti, V, Nb, Cr; } X = \text{C; and } T = \text{O, F}$ ) are the interesting component for this study. According to Figure 5.1, the possible MXenes' components for the  $M$ ,  $X$ , and  $T$  atomic types are represented by red, violet, and green colors, respectively, where the border for each color designates the chosen type for the study. For the  $M$  atomic type, Sc, Ti, V, and Cr are chosen based on the periodic table's trend of numbers of electrons in their outer shells, which are represented as  $|\text{Ar}|3d^14s^2$ ,  $|\text{Ar}|3d^24s^2$ ,  $|\text{Ar}|3d^34s^2$ , and  $|\text{Ar}|3d^54s^1$ , respectively, where Nb ( $|\text{Kr}|4d^45s^1$ ) has the same number of electrons as V. To investigate the relaxation of the  $M_2XT_2$  monolayer MXenes, firstly, bare- $\text{MX}_2$  are chosen as preliminary compound with  $M$  is Sc, Ti, V, Nb, and Cr. The primitive cell of the structure was used for the initial computations to investigate the properties in MXenes compounds.

1 IA																		2 IIA										13 IIIA										14 IVA										15 VA										16 VIA										17 VIIA										18 VIIIA																																																																																																																																																																																															
1	H																	He																																																																																																																																																																																																																																																											
3	Li			Be													5		6		7		8		9		10																																																																																																																																																																																																																																																		
11	Na			Mg													13		14		15		16		17		18																																																																																																																																																																																																																																																		
19	K			Ca			21		22		23		24		25		26		27		28		29		30		31		32		33		34		35		36																																																																																																																																																																																																																																								
37	Rb			Sr			39		40		41		42		43		44		45		46		47		48		49		50		51		52		53		54																																																																																																																																																																																																																																								
55	Cs			Ba			57 - 71		72		73		74		75		76		77		78		79		80		81		82		83		84		85		86																																																																																																																																																																																																																																								
87	Fr			Ra			89 - 103		104		105		106		107		108		109		110		111		112		113		114		115		116		117		118																																																																																																																																																																																																																																								
57																		58																		59																		60																		61																		62																		63																		64																		65																		66																		67																		68																		69																		70																		71																	
La																		Ce																		Pr																		Nd																		Pm																		Sm																		Eu																		Gd																		Tb																		Dy																		Ho																		Er																		Tm																		Yb																		Lu																	
89																		90																		91																		92																		93																		94																		95																		96																		97																		98																		99																		100																		101																		102																		103																	
Ac																		Th																		Pa																		U																		Np																		Pu																		Am																		Cm																		Bk																		Cf																		Es																		Fm																		Md																		No																		Lr																	

Figure 5.1 MXenes family is indicated in the periodic table by the red, purple, and green regions, which represent the  $M$ ,  $X$ , and  $T$  atoms, respectively, and the frame of that color denotes the chosen atom in the research.

### 5.1.1 Computational details

The structural parameter of MXenes have been calculated by using VASP as a theoretical implement for DFT calculations. The structural properties of the bare- $M_2C$  and the  $M_2CT_2$  monolayers ( $M = \text{Sc, Ti, V, Nb, Cr}$  and  $T = \text{O, F}$ ) are obtained by using the projector augmented-wave (PAW) method as implemented in the VASP. The Perdew-Burke-Ernzerhof (PBE) approach has been used to account with the form of exchange correlation energy in the Kohn-Sham equation. The cutoff energy of the plane wave expansion is 500 eV and the  $\Gamma$ -centered Monkhorst-Pack  $k$ -mesh of  $12 \times 12 \times 1$  is used for the BZ integrations of the calculations of hexagonal-like structure. The vdW interactions is also included in the calculations. In addition, the equilibrium state of volume and lattice parameter of the compound is revealed by fitting the calculated total energy of varying lattice parameters with the equation of state by Rose-Vinet.

### 5.1.2 Structural relaxation of the bare- $M_2C$ MXenes

Because MXenes have a hexagonal structure, the angle between the  $\mathbf{a}$ -vector and the  $\mathbf{b}$ -vector in the primitive cell is 120 degrees. The  $\mathbf{c}$ -vector is perpendicular to the  $\mathbf{a}$  and  $\mathbf{b}$  vectors, and a vacuum spacing of 20 Å has been included to optimize the monolayer structure. The initial coordinates of the  $M_1$ ,  $M_2$ , and C atoms in the primitive cell in which  $T_1$ , and  $T_2$  surface functional atoms would be added afterward are listed in Table 5.1, with the  $\mathbf{a}$  and  $\mathbf{b}$  vectors referring to lattice parameters and the  $\mathbf{c}$  vector referring to layer thickness. The findings reveal that the equilibrium structure of  $Sc_2C$ ,  $Ti_2C$ ,  $V_2C$ ,  $Nb_2C$ , and  $Cr_2C$  are discovered by fitting the calculations with the Rose–Vinet EOS, and its plotting is depicted by Figures 5.2(a), (b), (c), (d), and (e), respectively. The global minima of total energy for the  $Sc_2C$ ,  $Ti_2C$ ,  $V_2C$ ,  $Nb_2C$ , and  $Cr_2C$ , which correspond to the plots in Figure 5.2, are -22.101, -25.164, -26.545, -29.5162, and -26.239 eV, respectively. Moreover, the  $a$ -lattice parameters for the  $Sc_2C$ ,  $Ti_2C$ ,  $V_2C$ ,  $Nb_2C$ , and  $Cr_2C$  are 3.3104, 3.0113, 2.8813, 3.1105, and 2.7780 Å, respectively, which is almost equivalent to the reference from Guo ( $Ti_2C \sim 3.082$  Å), Zhao ( $V_2C \sim 2.897$  Å and  $Nb_2C \sim 3.135$  Å) and Naguib ( $Cr_2C \sim 2.787$  Å) (Guo *et al.*, 2015; Zhao *et al.*, 2014; Naguib *et al.*, 2014). The structural parameters and total energy of the  $M_2C$  compound are obtained as shown in Table 5.2.

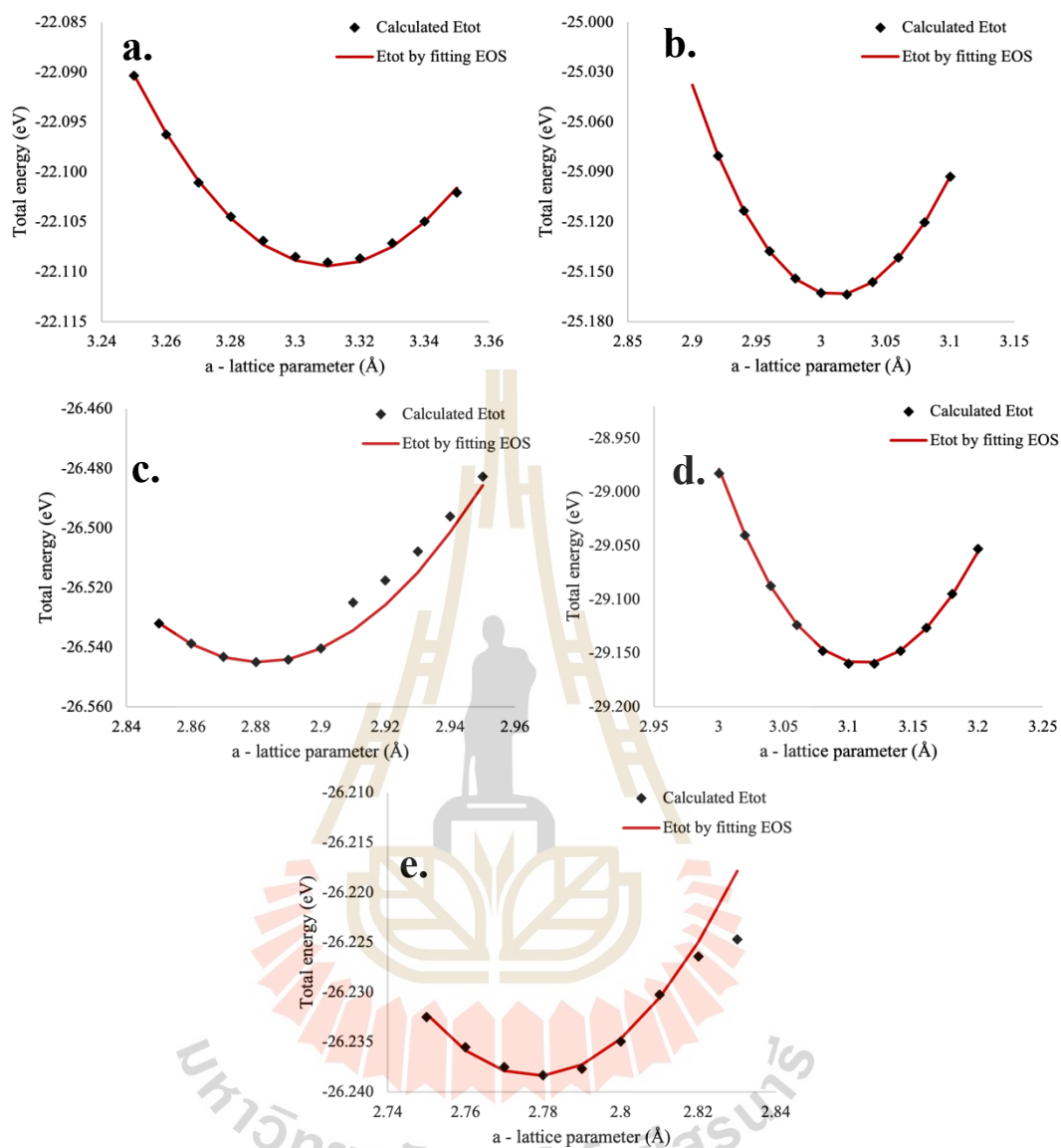


**Figure 5.2** The finding of an equilibrium structure of Sc<sub>2</sub>C, Ti<sub>2</sub>C, V<sub>2</sub>C, Nb<sub>2</sub>C, and Cr<sub>2</sub>C by fitting the calculations with the ROSE–Vinet’s equation of state where its plotting is represented by (a), (b), (c), (d), and (e), respectively.

**Table 5.1** indicate the initial structural composition of bare- $M_2C$  MXenes.

Label	Coordinate		
	$x$	$y$	$z$
$M_1$	$2/3$	$1/3$	0.8
$M_2$	$1/3$	$2/3$	0.2
C	0	0	0.5
$T_1$	-	-	1.0
$T_2$	-	-	0

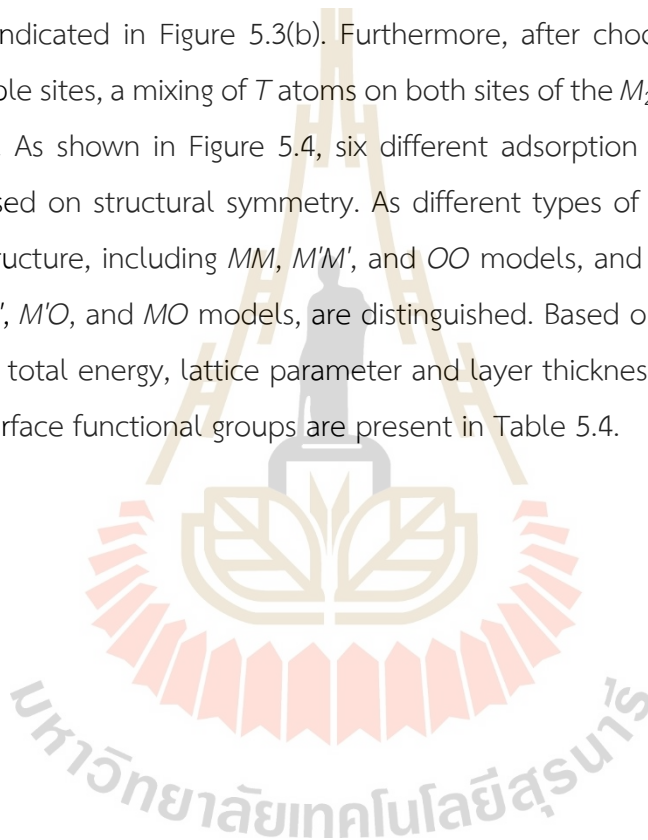
**Table 5.2** indicate the calculation information of structural relaxations of the  $M_2C$  compounds.

compound	$a$ -lattice parameters	Total energy	$a$ from Ref.
	(Å)	(eV)	
$Sc_2C$	3.3104	-22.101	-
$Ti_2C$	3.0113	-25.164	3.082 <sup>a</sup>
$V_2C$	2.8813	-26.545	2.897 <sup>b</sup>
$Nb_2C$	3.1105	-29.162	3.135 <sup>b</sup>
$Cr_2C$	2.7780	-26.239	2.787 <sup>c</sup>

<sup>a</sup> Ref. (Guo *et al.*, 2015)<sup>b</sup> Ref. (Zhao *et al.*, 2014)<sup>c</sup> Ref. (Naguib *et al.*, 2014)

### 5.1.3 Surface functional configurations and structural relaxations

By covering the surrounding  $M$  atoms with  $T$  surface functional atoms on both sides of the bare-MXenes surface, the structural configurations are predicted to be the preferred position among three alternative sites provided by  $M$ ,  $M'$ , and  $O$  as indicated in Figure 5.3 and Table 5.3. The  $M$  and  $O$  sites are respectively above the  $M_1$ , and  $C$  atoms as represented in Figure 5.3(a) and Figure 5.3(c). The  $M'$  site denotes a site where the  $T$  atom is on top of the hollow site and corresponds to the lower transition metal  $M_2$  which is indicated in Figure 5.3(b). Furthermore, after choosing the  $T$  functional atom's available sites, a mixing of  $T$  atoms on both sites of the  $M_2C$  monolayer's surface is achievable. As shown in Figure 5.4, six different adsorption site combinations are proposed based on structural symmetry. As different types of surface combinations, symmetric structure, including  $MM$ ,  $M'M'$ , and  $OO$  models, and asymmetric structure, including  $MM'$ ,  $M'O$ , and  $MO$  models, are distinguished. Based on the DFT calculation, the results of total energy, lattice parameter and layer thickness for all configurations of O and F surface functional groups are present in Table 5.4.



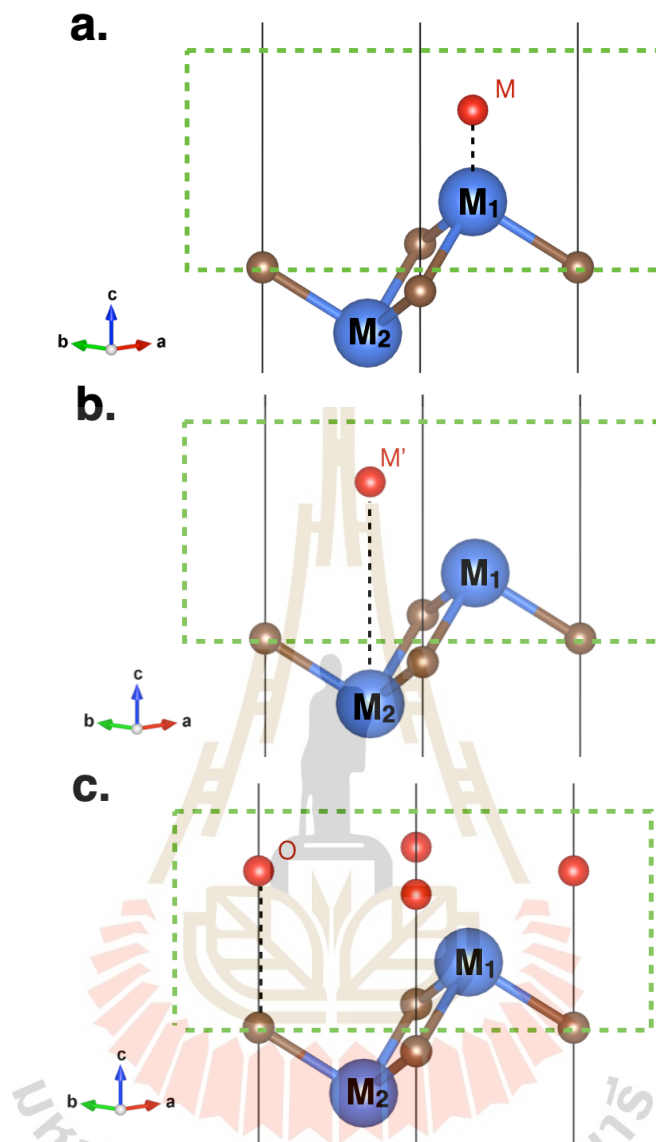
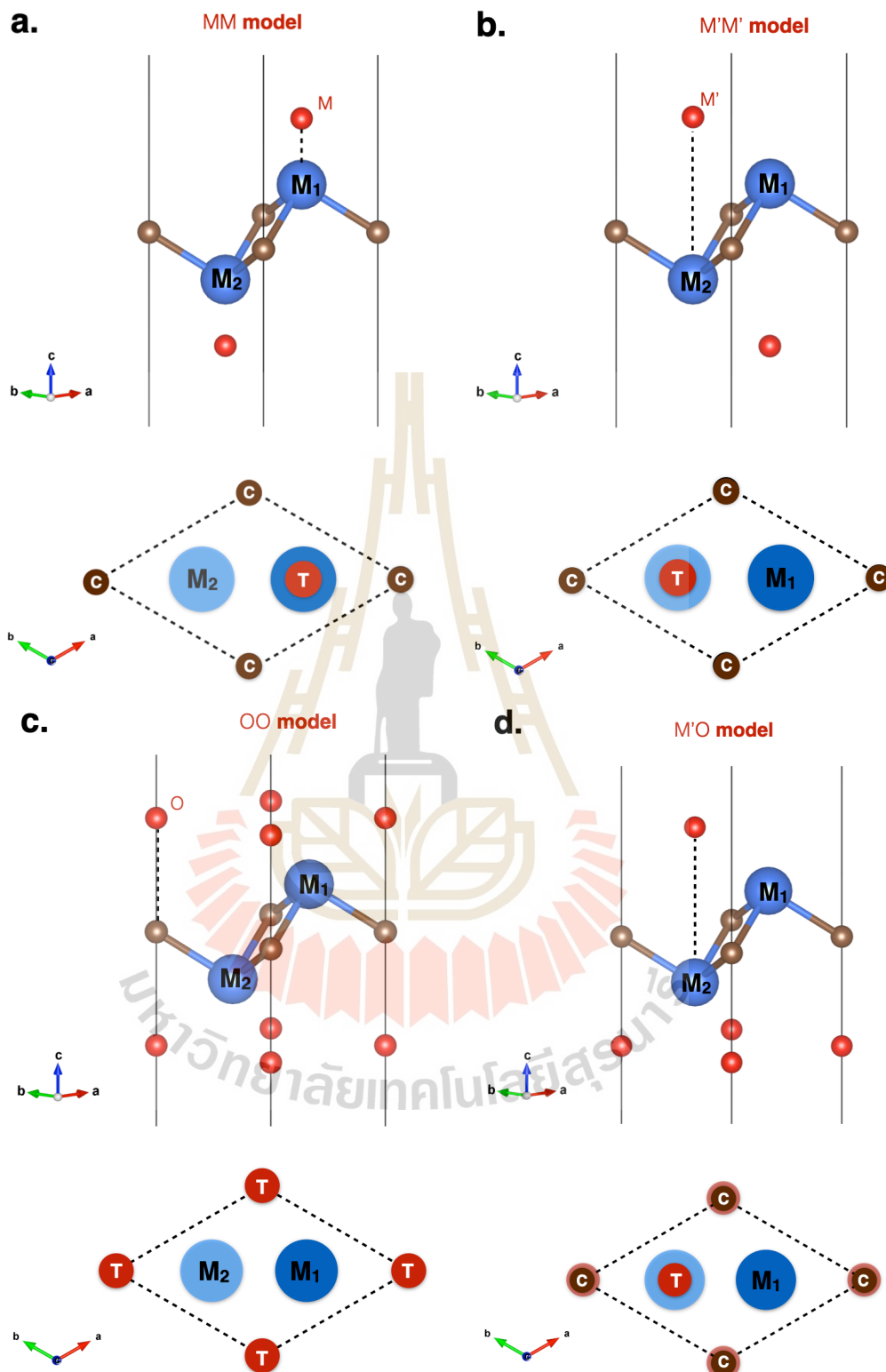
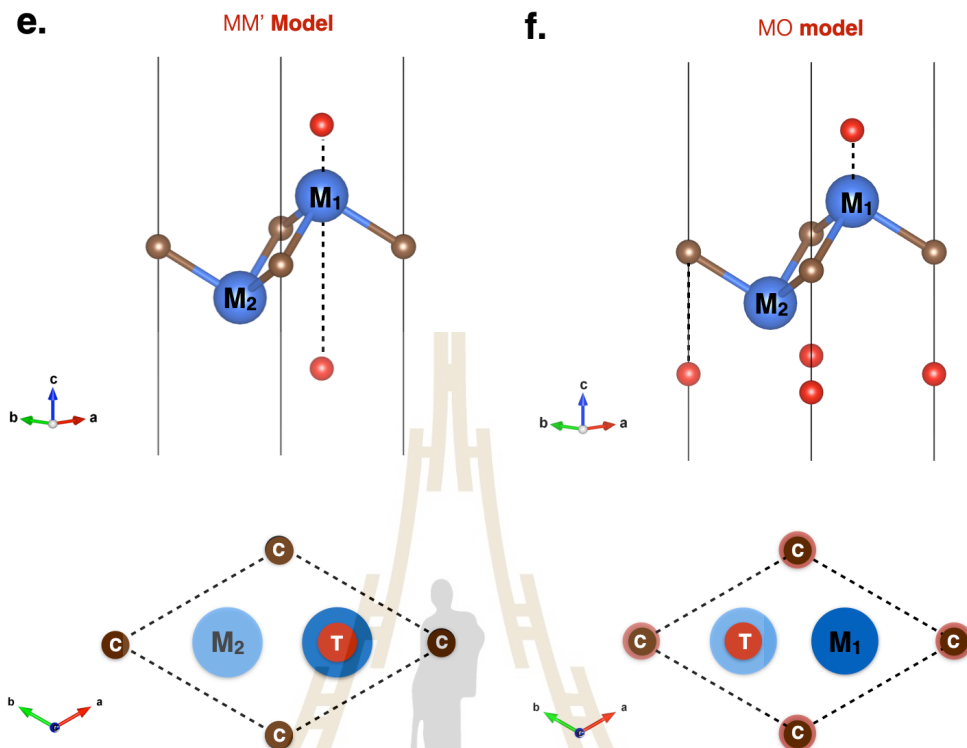


Figure 5.3 The preferable site of the  $M_2C$  surfaces that include (a)  $M$ , (b)  $M'$  and (c)  $O$  sites.



**Figure 5.4** Combinations of the  $M$ ,  $M'$  and  $O$  surface sites of the functional atoms forming  $M_2CT_2$  structure that present (a)  $MM$ , (b)  $M'M'$ , (c)  $OO$ , (d)  $M'O$ , (e)  $MM'$  and (f)  $MO$  models.



**Figure 5.4** Combinations of the  $M$ ,  $M'$  and  $O$  surface sites of the functional atoms forming  $M_2CT_2$  structure that present (a)  $MM$ , (b)  $M'M'$ , (c)  $OO$ , (d)  $M'O$ , (e)  $MM'$  and (f)  $MO$  models. (Continued)

**Table 5.3** compose of the compositions of T atom on both top and bottom surface of the  $M_2C$  monolayer in the unit cell (where  $M$  is Sc, Ti, V, Nb, Cr and  $T$  is O, F).

Label	Sites	Co-ordinate		
		$x$	$y$	$z$
$M$	top surface	$2/3$	$1/3$	1
$M'$	top surface	$1/3$	$2/3$	1
$O$	top surface	0	0	1
$M$	bottom surface	$1/3$	$2/3$	0
$M'$	bottom surface	$2/3$	$1/3$	0
$O$	bottom surface	0	0	0

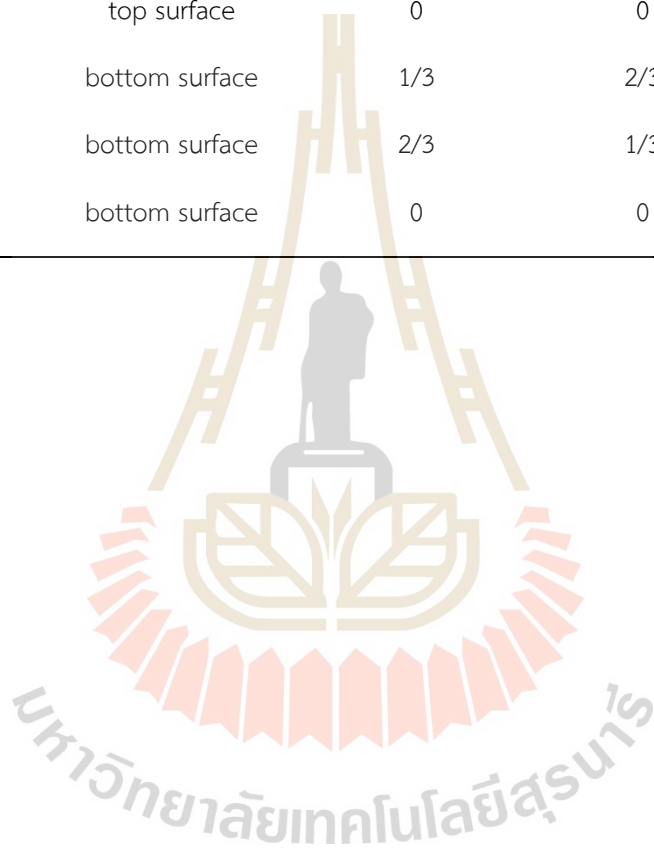


**Table 5.4** indicate the structural relaxation of the  $M_2CT_2$  monolayers where total energy, lattice parameter, and layer thickness are included.

	Total Energy (eV)		Lattice parameters a (Å)		Layer thickness d (Å)	
	F	O	F	O	F	O
<b>Sc<sub>2</sub>C</b>						
<i>MM</i>	-35.288	-33.740	3.503	3.461	6.003	6.166
<i>M'M'</i>	<b>-38.132</b>	-40.965	<b>3.251</b>	3.220	<b>4.783</b>	4.792
<i>M'O</i>	-37.550	<b>-41.622</b>	3.218	<b>3.410</b>	4.970	<b>3.843</b>
<i>OO</i>	-36.927	-41.498	3.171	3.351	5.180	4.067
<i>MM'</i>	-36.651	-37.482	3.355	3.288	5.350	5.464
<i>MO</i>	-35.993	-37.528	3.301	3.584	5.579	4.610
<b>Ti<sub>2</sub>C</b>						
<i>MM</i>	-38.086	-39.848	3.202	3.344	5.761	5.596
<i>M'M'</i>	<b>-39.794</b>	<b>-45.104</b>	<b>3.042</b>	<b>3.027</b>	<b>4.794</b>	<b>4.437</b>
<i>M'O</i>	-39.678	-44.381	3.004	2.999	4.919	4.609
<i>OO</i>	-39.391	-43.421	2.963	2.953	5.070	4.861
<i>MM'</i>	-38.936	-42.537	3.106	3.141	5.271	4.973
<i>MO</i>	-38.722	-41.739	3.063	3.095	5.394	5.162
<b>V<sub>2</sub>C</b>						
<i>MM</i>	-38.591	-42.437	3.165	3.105	5.328	5.362
<i>M'M'</i>	<b>-39.593</b>	<b>-44.756</b>	<b>2.964</b>	<b>2.882</b>	<b>4.632</b>	<b>4.433</b>
<i>M'O</i>	-39.128	-44.519	2.903	2.847	4.885	4.568
<i>OO</i>	-39.338	-44.160	2.782	2.811	5.134	4.721
<i>MM'</i>	-39.164	-43.397	2.986	2.962	5.092	4.908
<i>MO</i>	-38.668	-43.240	2.903	2.927	5.394	4.999

**Table 5.4** indicate the structural relaxation of the  $M_2CT_2$  monolayers where total energy, lattice parameter, and layer thickness are included. (Continued)

	Total Energy (eV)		Lattice parameters a (Å)		Layer thickness (Å)	
	F	O	F	O	F	O
<b>Nb<sub>2</sub>C</b>						
<i>MM</i>	-41.359	-45.412	3.113	3.307	6.310	5.859
<i>M'M'</i>	<b>-42.491</b>	<b>-48.730</b>	<b>3.184</b>	<b>3.122</b>	<b>4.990</b>	<b>4.634</b>
<i>M'O</i>	-42.068	-48.580	3.015	3.080	5.522	4.797
<i>OO</i>	-42.326	-48.215	2.988	3.032	5.541	4.990
<i>MM'</i>	-42.008	-46.833	3.187	3.181	5.540	5.271
<i>MO</i>	-41.827	-46.702	3.045	3.149	5.927	5.378
<b>Cr<sub>2</sub>C</b>						
<i>MM</i>	-37.611	-41.543	3.140	3.116	5.109	5.029
<i>M'M'</i>	<b>-37.829</b>	-42.709	<b>3.012</b>	2.768	<b>4.299</b>	4.625
<i>M'O</i>	-37.372	-43.018	2.844	2.721	4.844	4.739
<i>OO</i>	-37.417	<b>-43.385</b>	2.777	<b>2.687</b>	4.996	<b>4.812</b>
<i>MM'</i>	-37.521	-42.278	3.010	2.962	4.843	4.620
<i>MO</i>	-37.296	-41.992	2.846	2.790	5.253	5.101

## 5.2 Electronic properties and stability of the $M_2CT_2$ monolayer

This section builds upon the literature studies in Section 2.2.2, which discuss how to tune the electronic properties of a material by including surface structure variations. The structure that is formed by various surface functional groups, as well as their position, can have a significant impact on the material's electronic characteristics. For example, different types of functionalized atom ( $T$ ), such as  $Ti_2CO_2$  and  $Ti_2CF_2$ , differentiate electronic behavior of semiconductors and metals, as shown in Figure 2.8. Moreover, the difference electronic in properties was also achieved by rearranging the functionalized atom composition of  $Sc_2CO_2$  in Figures 2.9 and 2.10. However, it is important to investigate why certain surface functional types and their locations control the electronic properties of layered MXenes. Thus, the studies utilizing a significant number of surface functionalized permutations and transition metal based MXenes will then be improved. This section has provided computational studies of electronic characteristics such as DOS and formation energy as well as the association between layer thickness ( $d$ ), DOS, and formation energy.

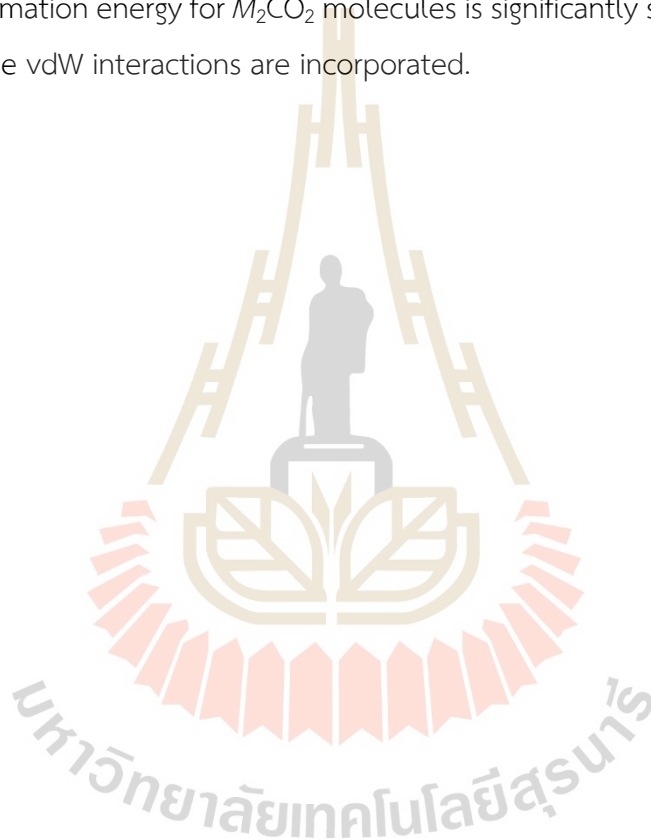
### 5.2.1 Stability of the $T$ atoms on the $M_2C$ layer.

In the computation and experiment, the stability of each model for the  $M_2CT_2$  MXenes is assessed using the formation energy ( $E_f$ ) estimations for the  $T$  functional group atoms adsorbed on the  $M_2C$  layer, which are referred to as the adsorption energy (Fu *et al.*, 2019). In this work, the electronic characteristics consisting of DOS and adsorption energy for the structural models of  $MM$ ,  $M'M'$ ,  $OO$ ,  $MM'$ ,  $MO$ , and  $M'O$  in the  $M_2CT_2$  ( $M = Sc, Ti, V, Nb, Cr$ , and  $T = O, F$ ) system are symmetrically performed. The preliminary results of the total energy from the structural relaxation sections are utilized. The formation energy ( $E_f^{M_2CT_2}$ ) of the surface functional atom adsorbed on the surface of the  $M_2CT_2$  MXenes is defined as

$$E_f^{M_2CT_2} = E^{M_2CT_2} - E^{M_2C} - 2 \frac{E^{T_x}}{x}, \quad 5.1$$

where  $E^{M_2CT_2}$ ,  $E^{M_2C}$ , and  $E^{T_x}$  are the total energies of the  $M_2CT_2$ , pristine  $M_2C$ , and  $T_x$  obtained from the (VASP) DFT calculations. According to this definition, the greater

negative formation energies indicate the high possibility of the  $T$  atoms adsorbing on both surface sides of the pristine layer, leading to compositions that are thermodynamically stable. The computation of the formation energy is presented, as shown in Figure 5.5 by displaying the lowest energy of every models in each compound, and compared to the reference from Khazaei *et al* (Khazaei *et al.*, 2013). In addition, the  $M'O$  model for  $Sc_2CO_2$ , the  $M'M'$  model for  $Ti_2CO_2$ ,  $V_2CO_2$  and  $Nb_2CO_2$ , and the  $OO$  model for  $Cr_2CO_2$  are achieved the lowest energy. Interestingly, the estimated formation energy for  $M_2CO_2$  molecules is significantly shifted down by about 1 eV when the vdW interactions are incorporated.



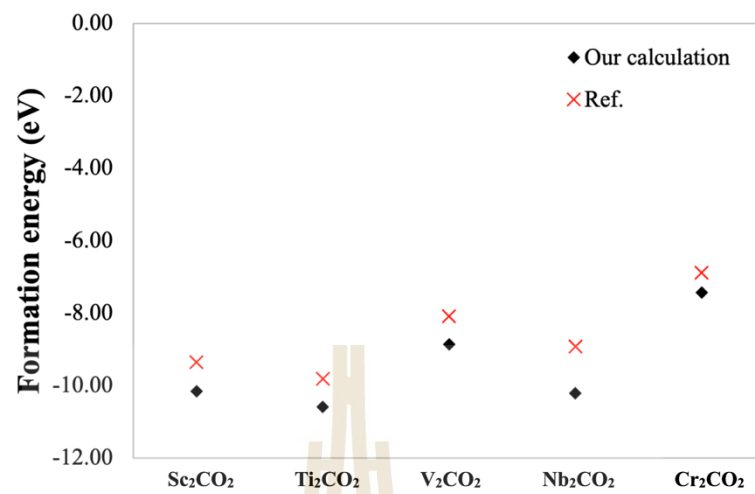


**Figure 5.5** Comparisons formation energy between our calculation with the vdW interaction and the reference's calculation without the vdW interactions of the  $M'M'$  model of the  $M_2CO_2$  MXenes (Khazaei *et al.*, 2013).

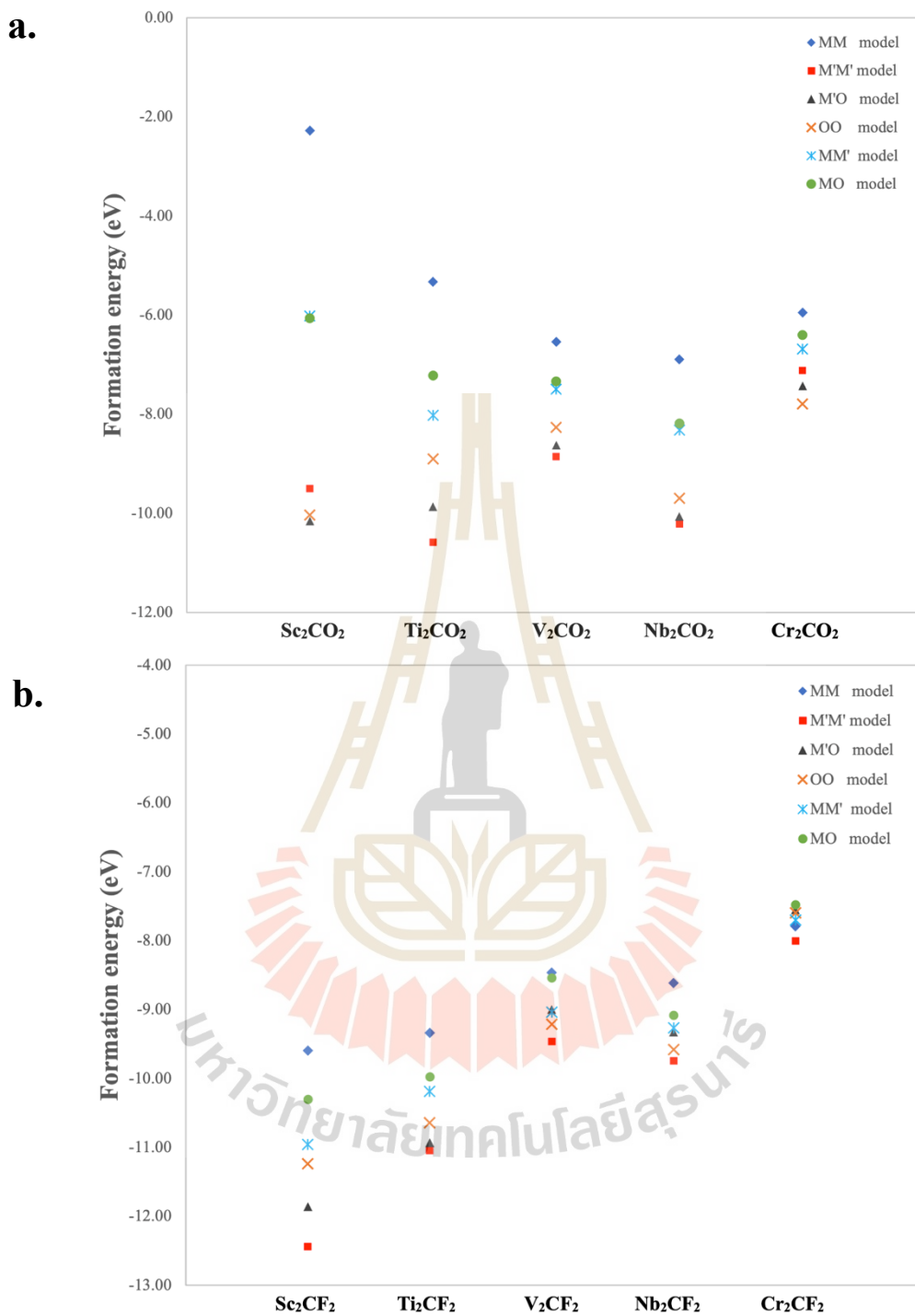


Figure 5.6 Formation energy of (a)  $M_2CO_2$  and (b)  $M_2CF_2$  monolayers with  $M$  is Sc, Ti, V, Nb, and Cr transition metal.

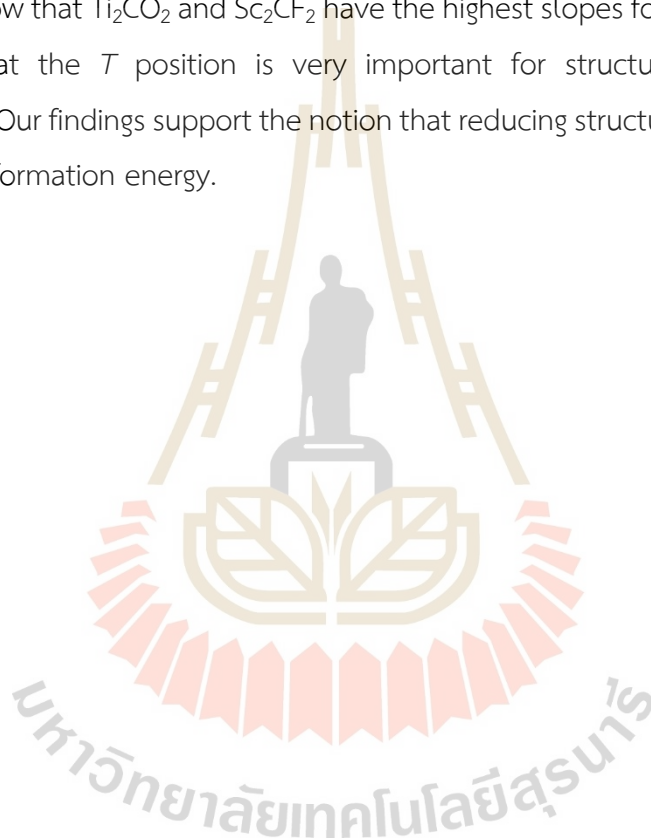
The calculations of the formation energy for the monolayer  $M_2CT_2$ , which consist of  $MM$ ,  $M'M'$ ,  $M'O$ ,  $OO$ ,  $MM'$ , and  $MO$  models, are presented in Figure 5.6, where Figures 5.6(a) and (b) illustrate the  $M_2CO_2$  and  $M_2CF_2$ , respectively. Consequently, excluding the  $Cr_2CF_2$ , the  $M'M'$ ,  $M'O$ , and  $OO$  models constitute a set of the  $M_2CT_2$ 's most favorable models. Instead of the  $M'M'$  model, which usually becomes a favorable structure among the  $M_2CT_2$  compounds, the  $M'O$  and  $OO$  models are preferable for the  $Sc_2CO_2$  and  $Cr_2CO_2$ , respectively. The calculations also show that the structural models for the compounds  $Ti_2CO_2$ ,  $V_2CO_2$ ,  $Nb_2CO_2$ ,  $Sc_2CF_2$ , and  $Ti_2CF_2$  have unique formation energy patterns. These compounds' favorable structures are arranged according to the  $M'M'$ ,  $M'O$ ,  $OO$ ,  $MM'$ ,  $MO$ , and  $MM$  models. The  $V_2CF_2$  and  $Nb_2CF_2$  almost have the same pattern as compared to the pattern of the  $Ti_2CO_2$ ,  $V_2CO_2$ ,  $Nb_2CO_2$ ,  $Sc_2CF_2$ , and  $Ti_2CF_2$  compounds. However, the formation energy of the  $M'O$  model for the  $V_2CF_2$  and  $Nb_2CF_2$  has slightly shifted up to a value above that of the  $MM'$  model. On the other hand, for the  $Sc_2CO_2$  structure, the  $M'O$ ,  $OO$ , and  $M'M'$  models clearly separated from other models in the relatively low formation energy area, with the  $M'O$  model having the lowest formation energy. Interestingly,  $Ti_2CO_2$  and  $Sc_2CF_2$  show the global minima formation energy among the  $M_2CT_2$ 's structural models, which can be correlated with the neutral oxidation state in the compound.

On the other hand, the plotted pattern for the formation energy of all structural models has an initial trend to constrict and further increases correlated with the number of transition metal's valence electrons for both  $M_2CO_2$  and  $M_2CF_2$ . We also observed that the larger size of the transition metal may contribute to the constricting trend for the formation energy value. For instance, when  $V_2CT_2$  and  $Nb_2CT_2$  ( $T=F, O$ ) are taken into consideration, the trend of the formation energy value of the structural models constricts as the transition metal size decreases, despite  $Nb_2CT_2$  having a larger size than  $V_2CT_2$  and the same number of valence electrons.

### 5.2.2 Effect of the layer thickness of the $M_2CT_2$ on the formation energy

In this section, we would like to observe the relation between the layer thickness and the formation energy. We may define the layer thickness ( $d$ ) by

measuring the distance between two functional groups on both sides of a layer in the  $z$ -coordinate. For instance,  $d$  is determined by measuring the length between both O atoms of the  $M_2CO_2$ . The various surface structures constructed at different  $T$  locations would have different  $d$  values. The depiction of the relationship between layer thickness ( $d$ ) and the formation energy shown in Figure 5.7 is made using all the estimated data for the  $M_2CT_2$  MXenes from the preceding section. The linearly tendency of the  $M_2CO_2$  and  $M_2CF_2$  are indicated in Figures 5.7(a) and (b), respectively. The plots show that  $Ti_2CO_2$  and  $Sc_2CF_2$  have the highest slopes for O and F adsorptions, indicating that the  $T$  position is very important for structural stability in these compounds. Our findings support the notion that reducing structural thickness is crucial for reducing formation energy.



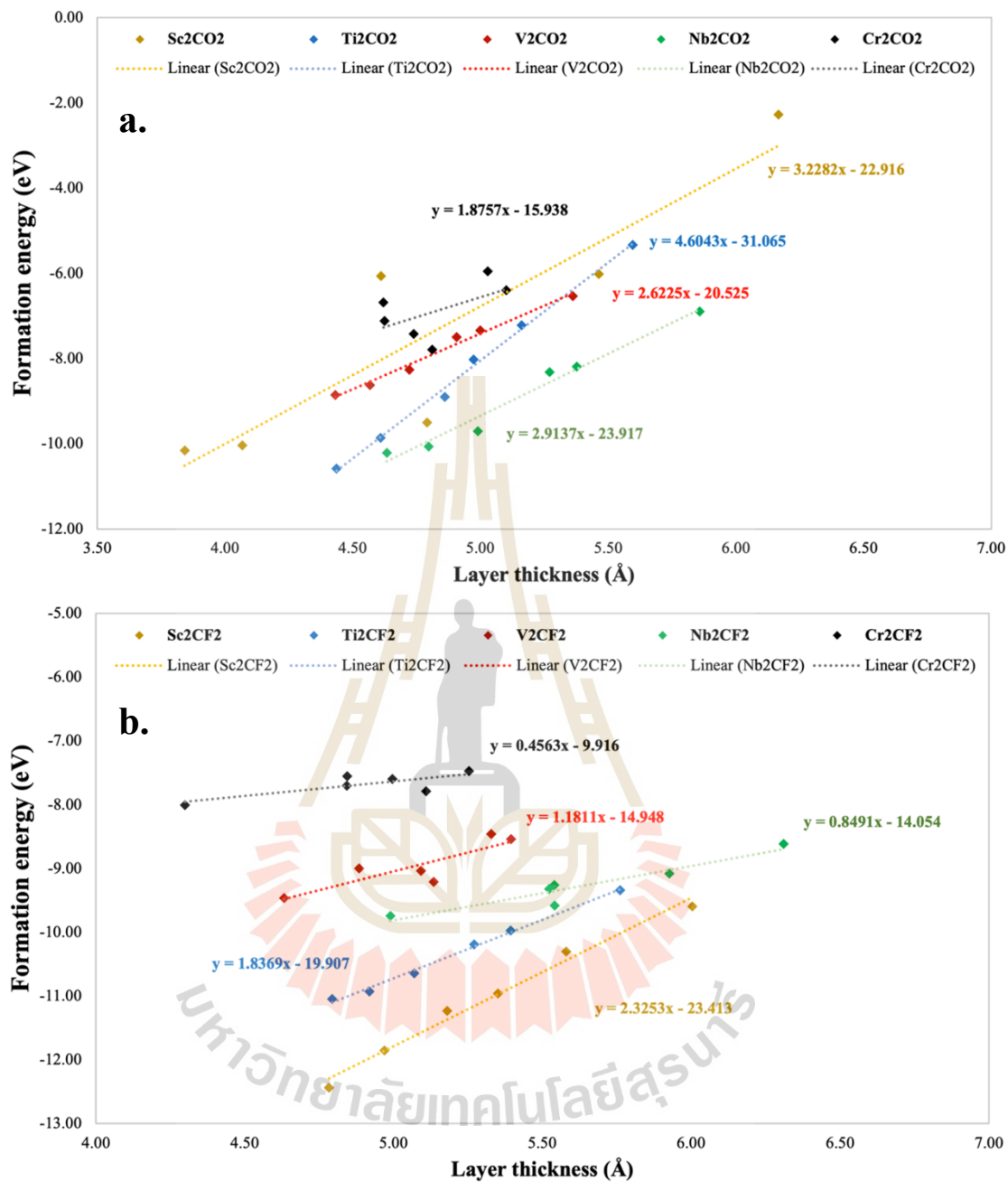


Figure 5.7 The plotting of the relation between layer thickness ( $d$ ) and the formation energy of (a)  $M_2CO_2$  and (b)  $M_2CF_2$ .

### 5.2.3 Density of state

The density of state (DOS) calculations is also obtained by using the projector augmented-wave (PAW) method as implemented in the Vienna *ab-initio* simulation Package (VASP). The form of exchange correlation energy in the Kohn-Sham equation is treated according to the Perdew-Burke-Ernzerhof (PBE) approach. The plane wave expansion's cutoff energy is specified to be the largest energy on the pseudopotential of all atomic species in the compound. For the BZ integrations, the  $\Gamma$ -centered Monkhorst-Pack  $k$ -mesh of DOS calculation is extended to be  $20 \times 20 \times 1$  in which the vdW interactions are also considered in the computations. In the theoretical aspect, partial density of state (PDOS) can provide additional information about the electronic structure of each component for each selected compound. Note that the bare  $\text{Ti}_2\text{C}$  and  $\text{Sc}_2\text{C}$  structures are metallic in nature, as illustrated in Figure 2.8(a) (Bai *et al.*, 2016) and Figure 2.9(a) (Khazaei *et al.*, 2013), respectively, whereas the energy states around the fermi energy are mostly constituted of the d orbitals of the transition metals (Ti and Sc). The lowest valence bands in the  $\text{Ti}_2\text{C}$  compound are generated by C-s states with a tiny mixture of Ti-p and d states, whereas the higher valence bands range from -5.5 eV to -2.5 eV and correspond to a substantial hybridization of Ti-d and C-p orbitals. However, addition of the surface functional groups with the F and O, on the other hand, results in a variety of electronic characteristics. The PDOS for each structural model, that rearranges by the formation energy values, is systematically investigated as illustrated in Figure 5.8, 5.9, 5.10, 5.11, 5.12, 5.13, 5.14, 5.15, 5.16, and 5.17, for the  $\text{Sc}_2\text{CO}_2$ ,  $\text{Ti}_2\text{CO}_2$ ,  $\text{V}_2\text{CO}_2$ ,  $\text{Nb}_2\text{CO}_2$ ,  $\text{Cr}_2\text{CO}_2$ ,  $\text{Sc}_2\text{CF}_2$ ,  $\text{Ti}_2\text{CF}_2$ ,  $\text{V}_2\text{CF}_2$ ,  $\text{Nb}_2\text{CF}_2$ , and  $\text{Cr}_2\text{CF}_2$  compounds, respectively.

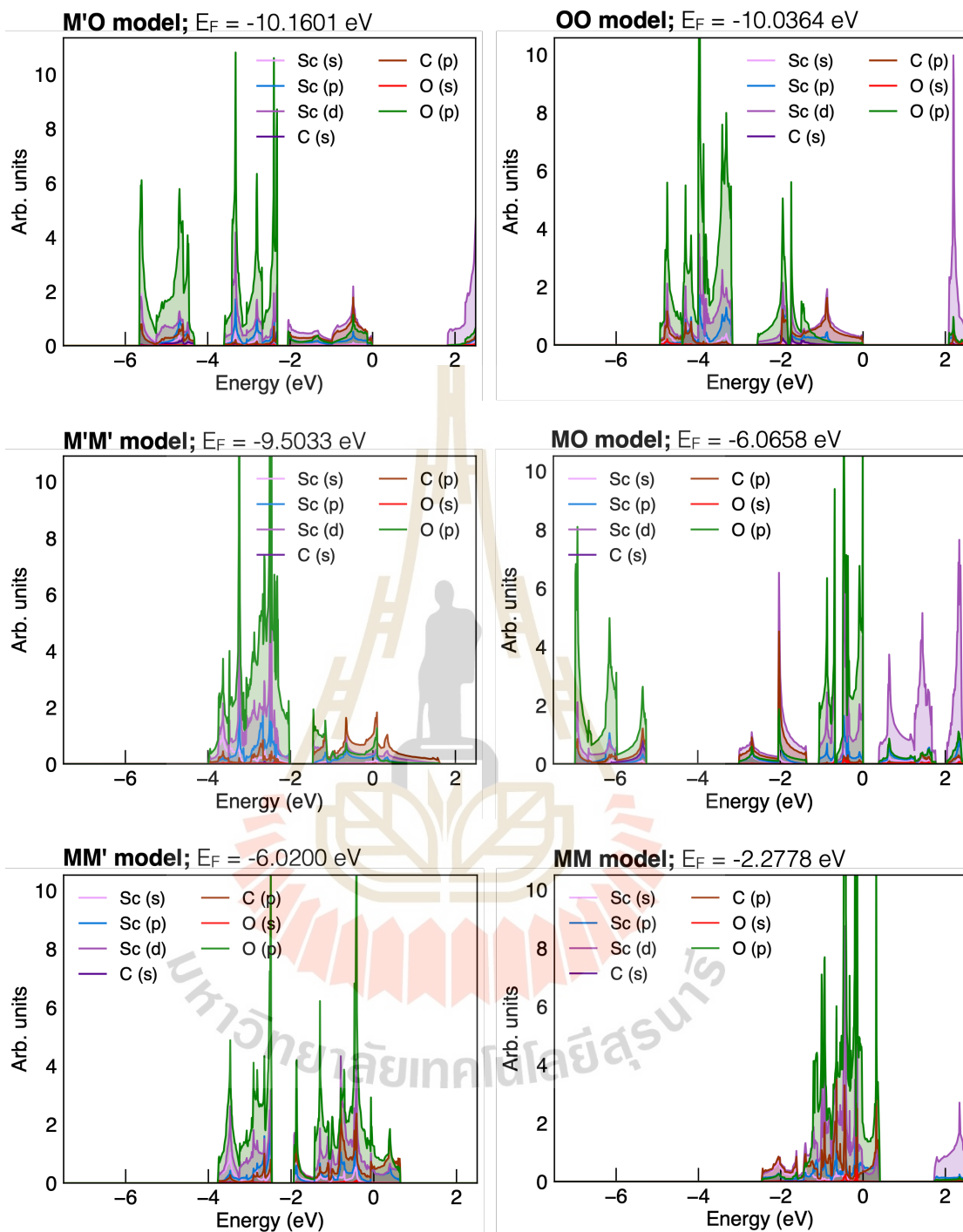


Figure 5.8 PDOS of  $\text{Sc}_2\text{CO}_2$  with  $M'M'$ ,  $M'O$ ,  $OO$ ,  $MO$ ,  $MM'$ , and  $MM$  models rearranged according to formation energy value.

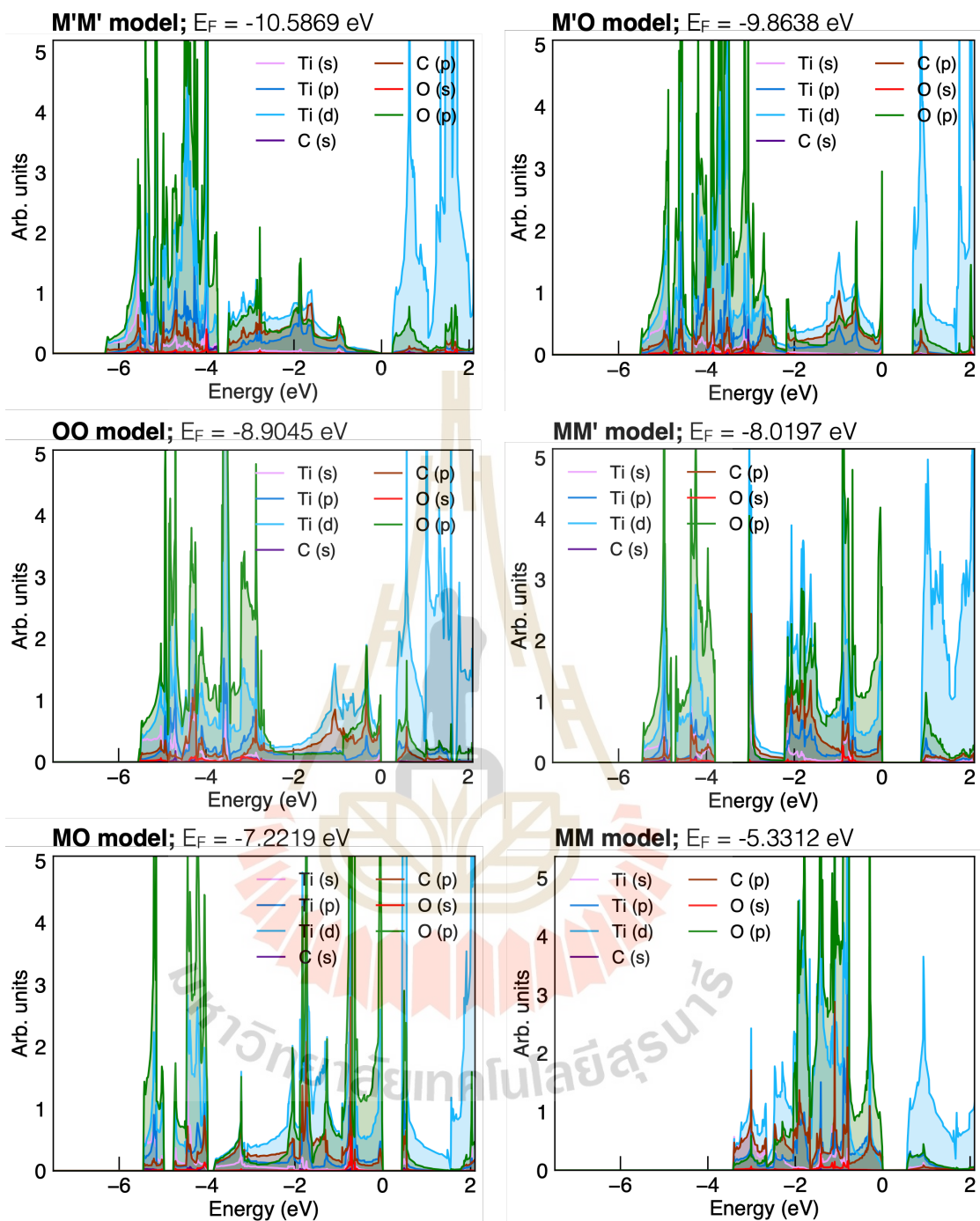


Figure 5.9 PDOS of  $\text{Ti}_2\text{CO}_2$  with  $M'M'$ ,  $M'O$ ,  $OO$ ,  $MO$ ,  $MM'$ , and  $MM$  models rearranged according to formation energy value.

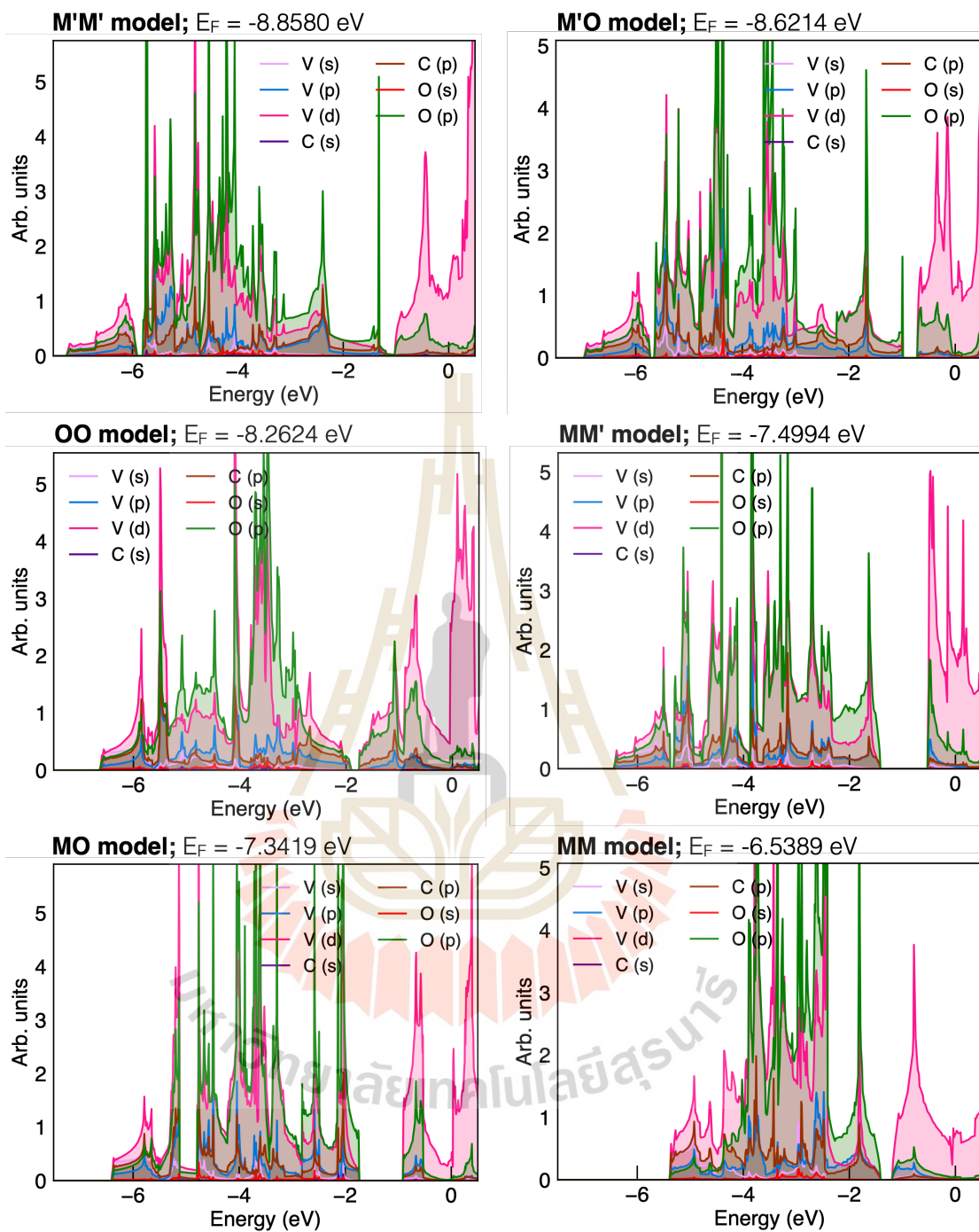


Figure 5.10 PDOS of  $V_2CO_2$  with  $M'M'$ ,  $M'O$ ,  $OO$ ,  $MO$ ,  $MM'$ , and  $MM$  models rearranged according to formation energy value.

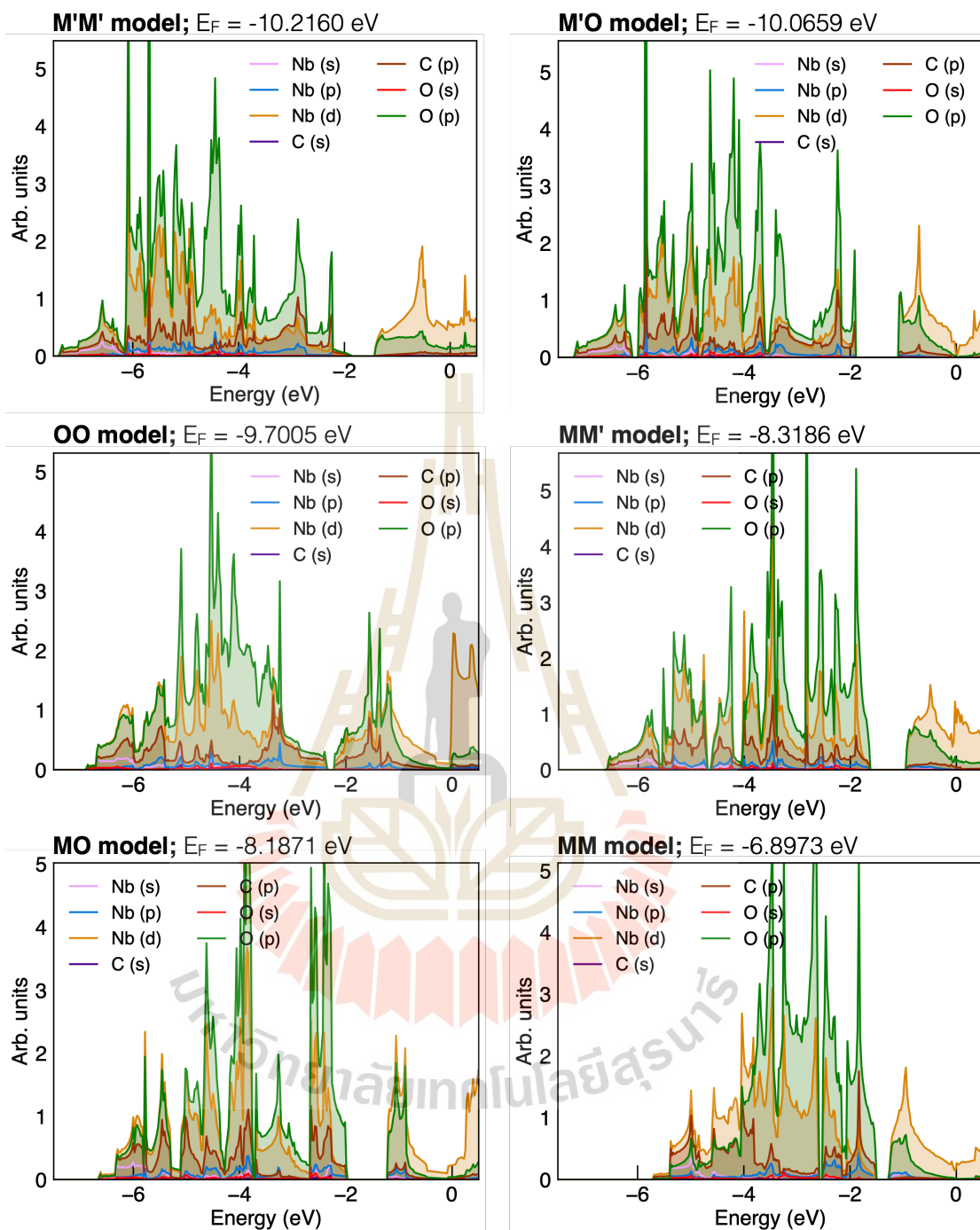


Figure 5.11 PDOS of  $\text{Nb}_2\text{CO}_2$  with  $M'M'$ ,  $M'O$ ,  $OO$ ,  $MO$ ,  $MM'$ , and  $MM$  models rearranged according to formation energy value.

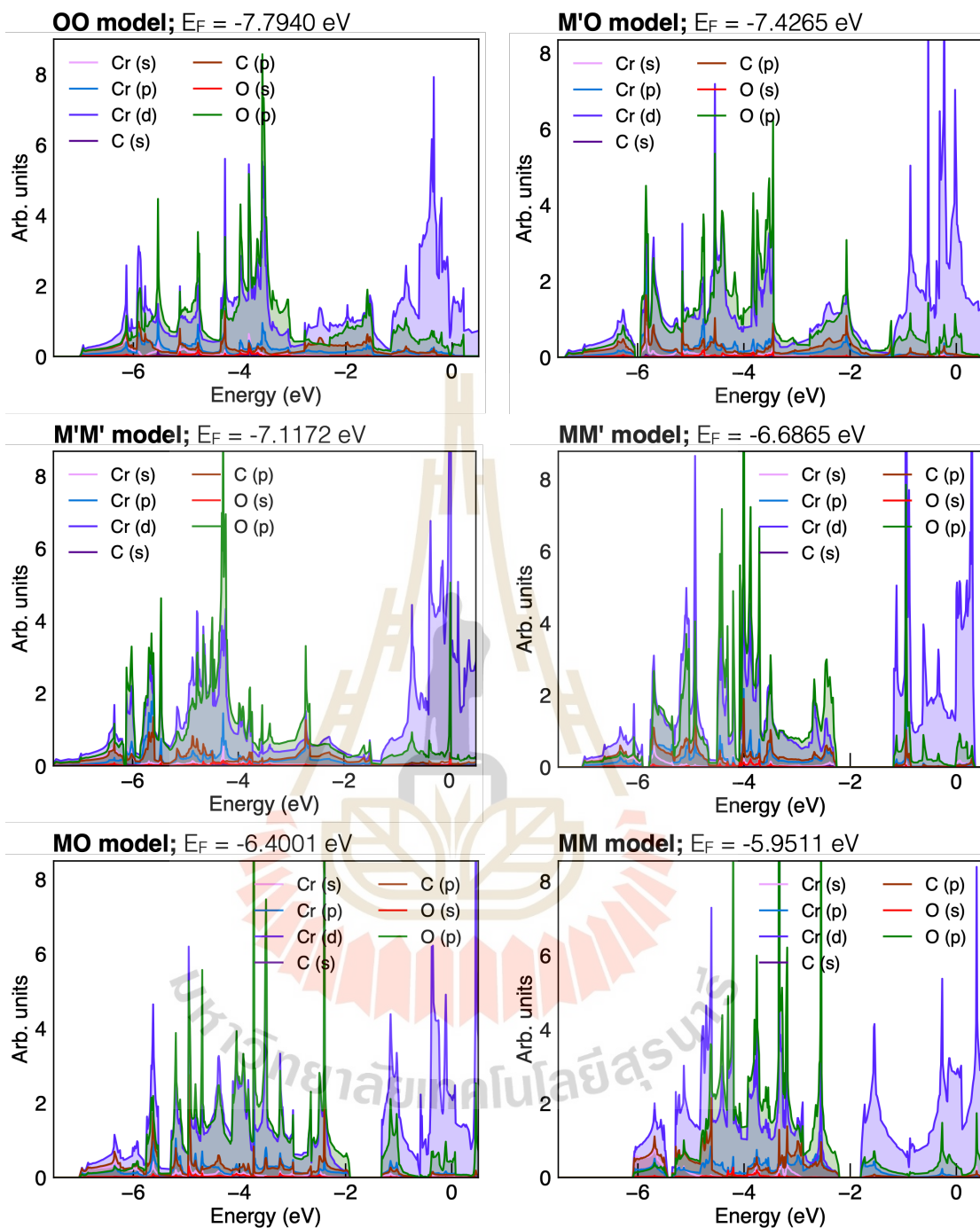


Figure 5.12 PDOS of  $\text{Cr}_2\text{CO}_2$  with  $M'M'$ ,  $M'O$ ,  $OO$ ,  $MO$ ,  $MM'$ , and  $MM$  models rearranged according to formation energy value.

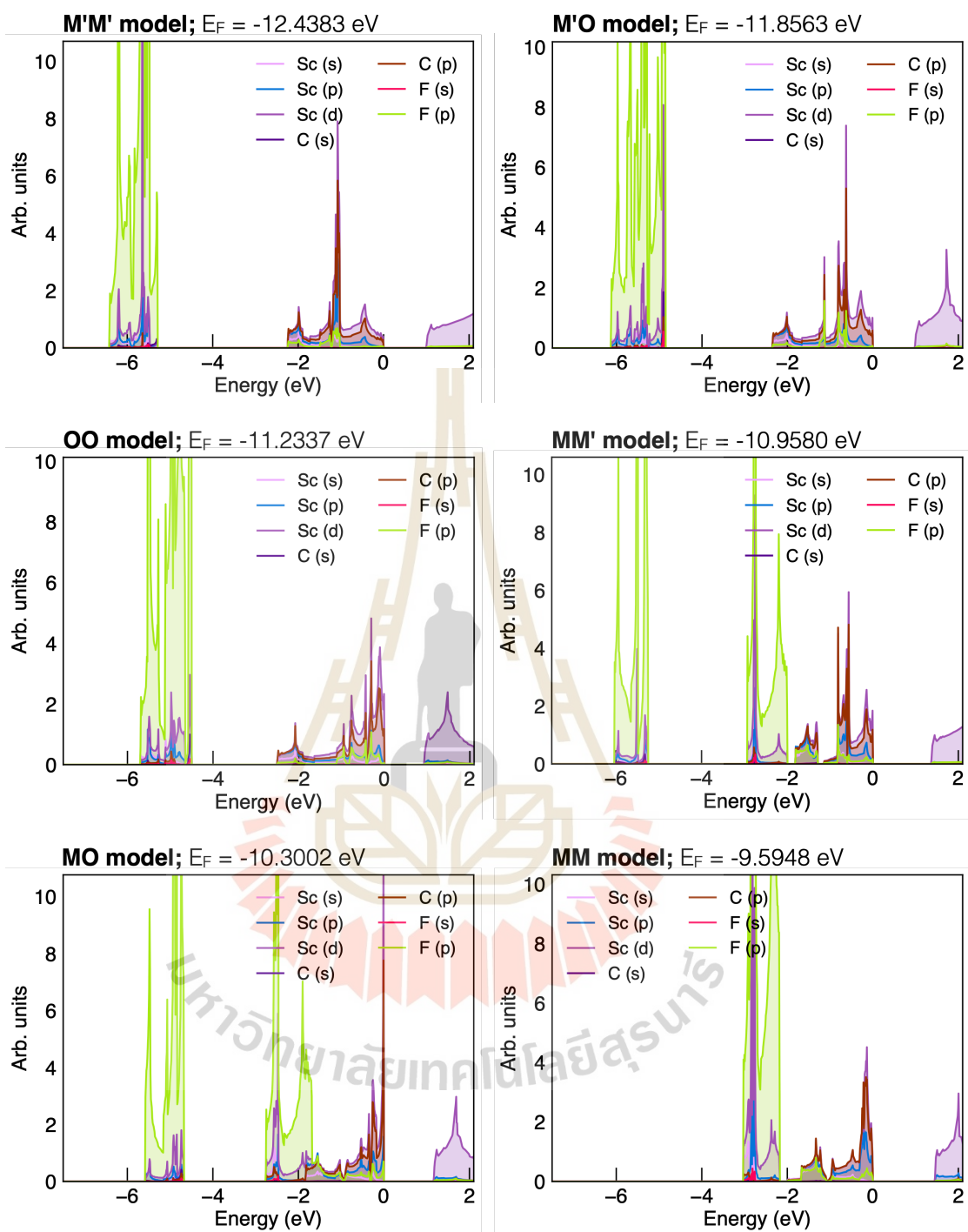


Figure 5.13 PDOS of  $\text{Sc}_2\text{CF}_2$  with  $M'M'$ ,  $M'O$ ,  $OO$ ,  $MO$ ,  $MM'$ , and  $MM$  models rearranged according to formation energy value.

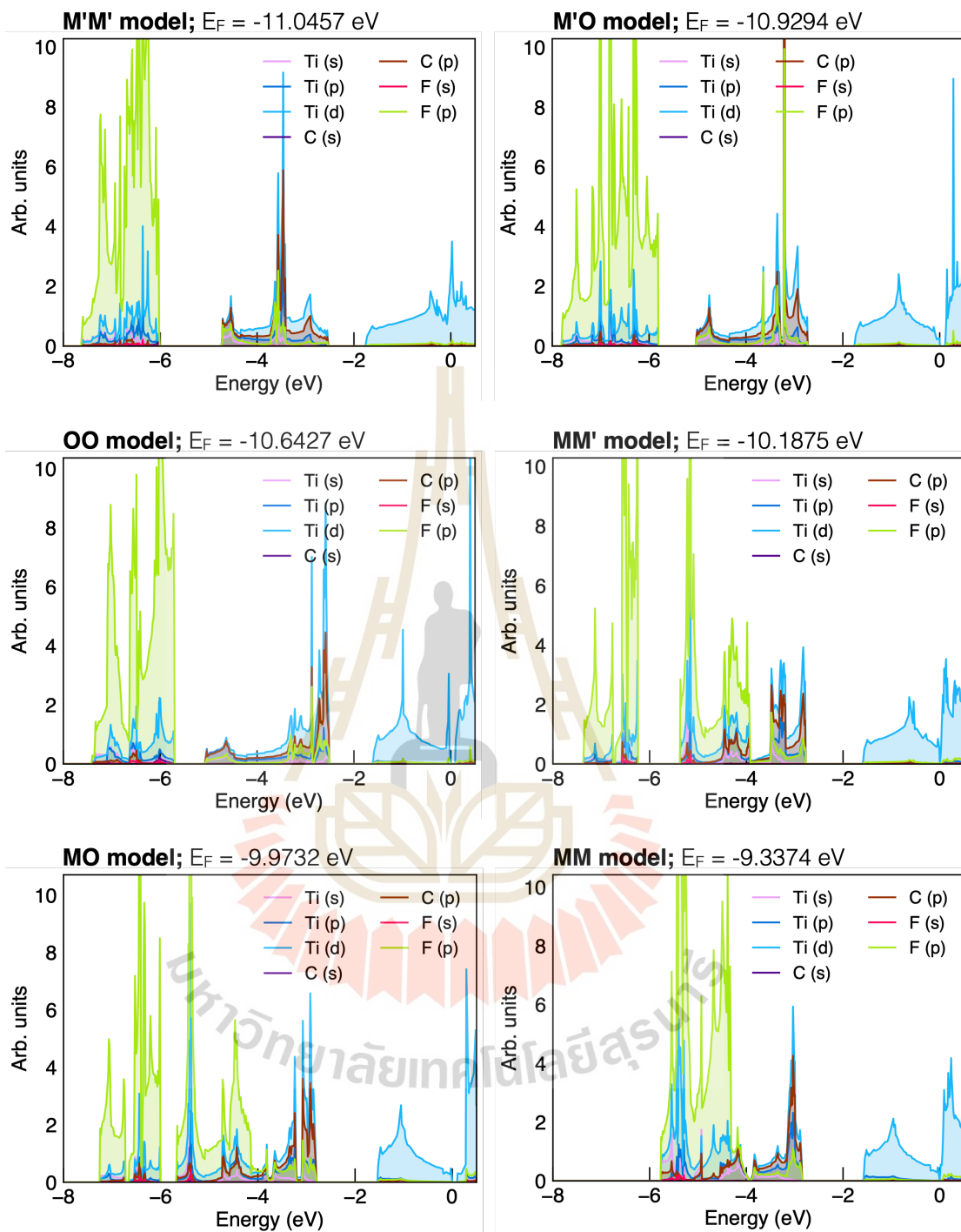


Figure 5.14 PDOS of  $\text{Ti}_2\text{CF}_2$  with  $M'M'$ ,  $M'O$ ,  $OO$ ,  $MO$ ,  $MM'$ , and  $MM$  models rearranged according to formation energy value.

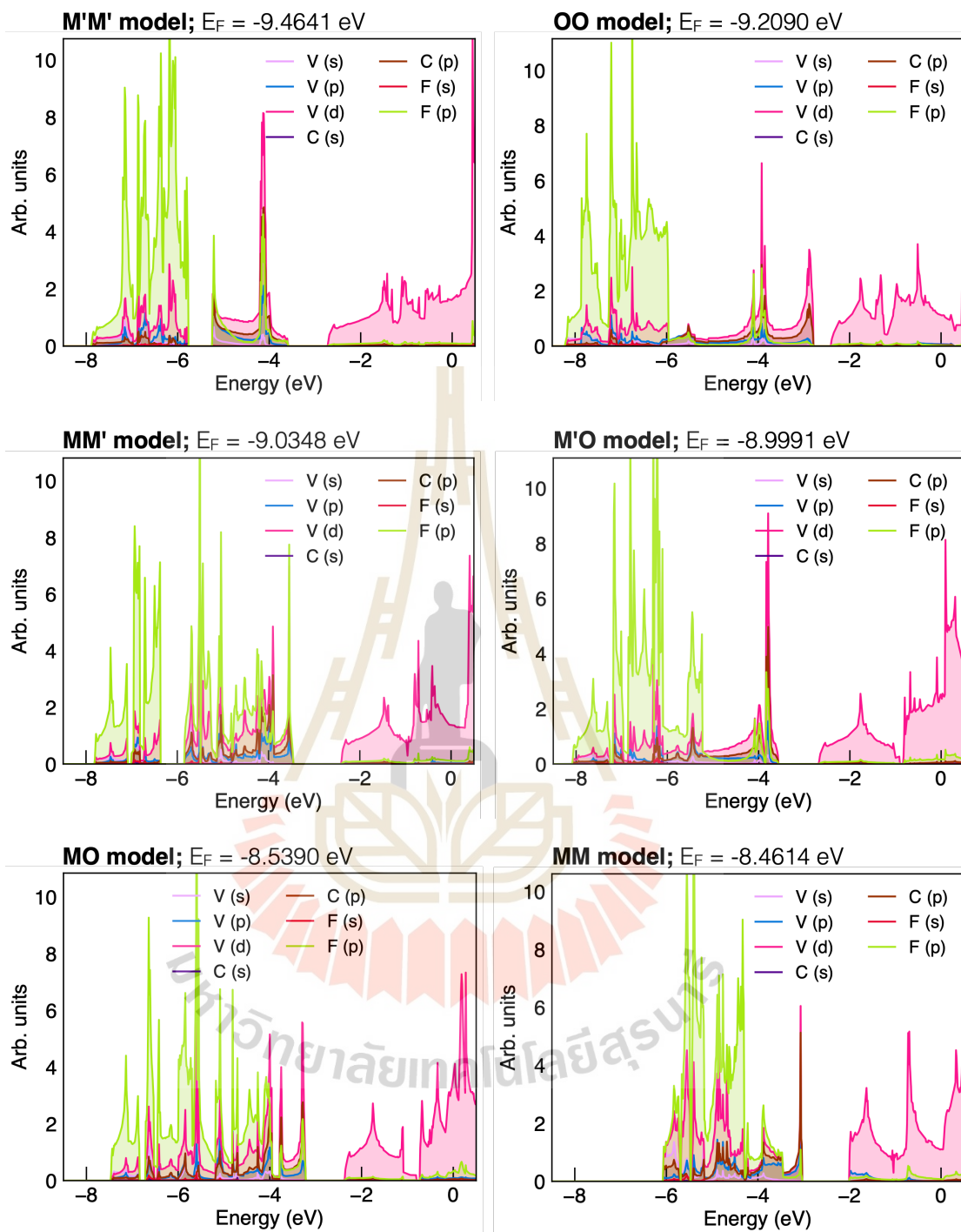


Figure 5.15 PDOS of  $V_2CF_2$  with  $M'M'$ ,  $M'O$ ,  $OO$ ,  $MO$ ,  $MM'$ , and  $MM$  models rearranged according to formation energy value.

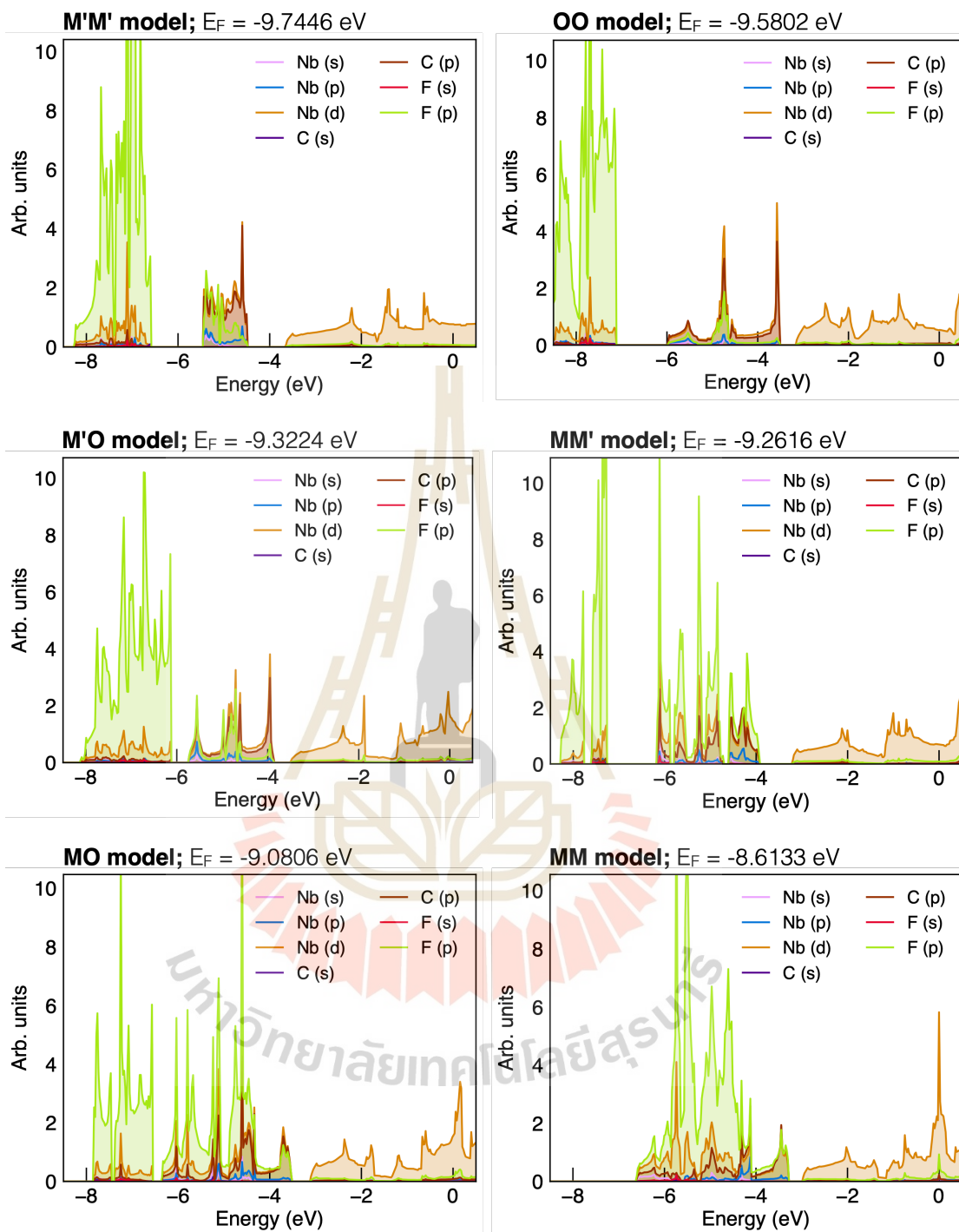


Figure 5.16 PDOS of  $\text{Nb}_2\text{CF}_2$  with  $M'M'$ ,  $M'O$ ,  $OO$ ,  $MO$ ,  $MM'$ , and  $MM$  models rearranged according to formation energy value.

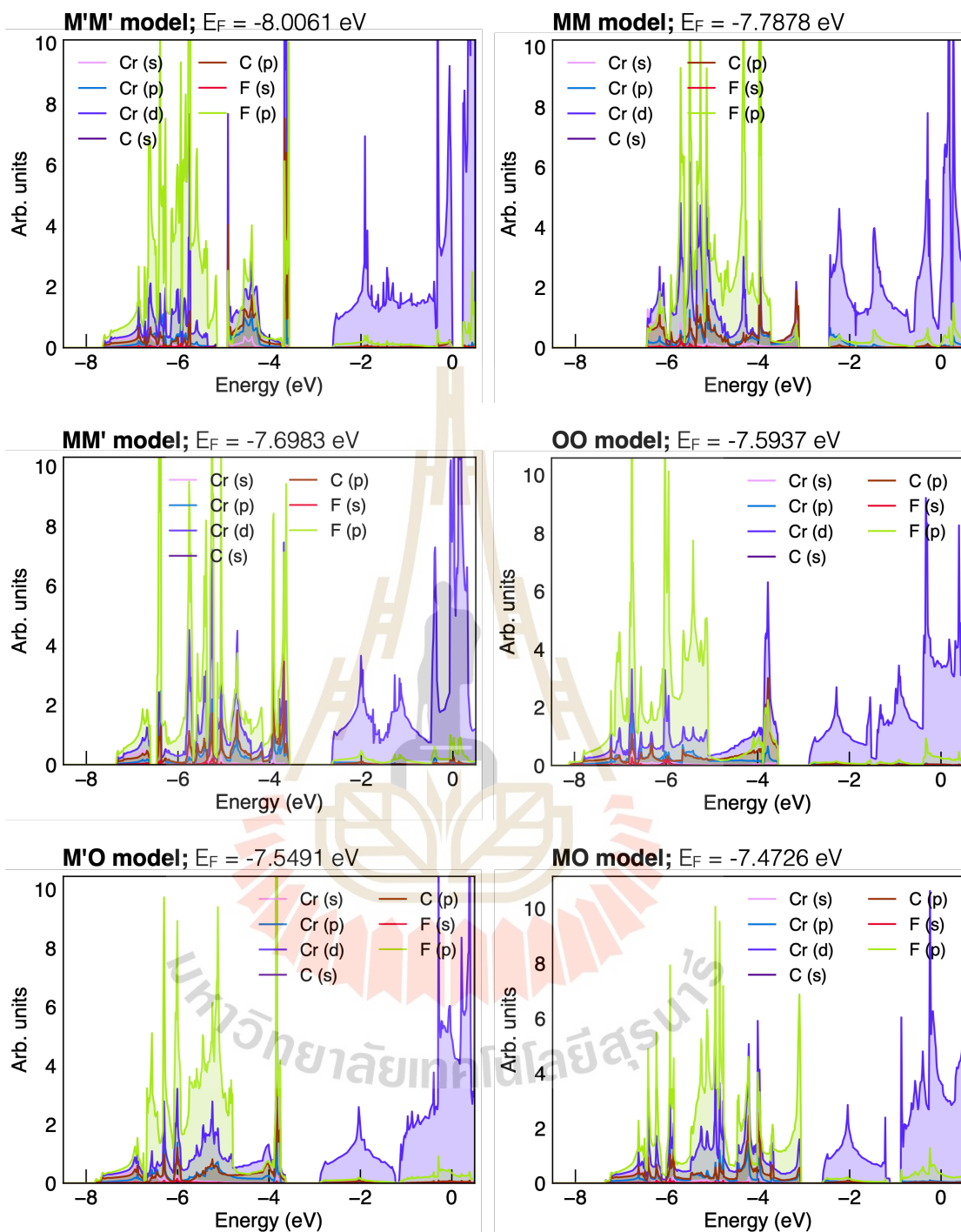


Figure 5.17 PDOS of  $\text{Cr}_2\text{CF}_2$  with  $M'M'$ ,  $M'O$ ,  $OO$ ,  $MO$ ,  $MM'$ , and  $MM$  models rearranged according to formation energy value.

The estimations show that the  $\text{Sc}_2\text{CO}_2$ ,  $\text{Sc}_2\text{CF}_2$ ,  $\text{Ti}_2\text{CO}_2$ , and  $\text{Ti}_2\text{CF}_2$  exhibit semiconductors with the conduction band being mostly given by the empty  $M$ -d transition metal states where the valence band edge is mostly given by the C-p sharing states. Interestingly, high energy gaps can be modified by adjusting the functional group's compositions for  $\text{Sc}_2\text{CO}_2$  and  $\text{Sc}_2\text{CF}_2$  compounds as indicated in Figure 5.8 and Figure 5.13. In some cases, e.g., the  $\text{Sc}_2\text{CO}_2$  compound with the  $M'O$ ,  $OO$ , and  $MO$  models and the  $\text{Cr}_2\text{CF}_2$  compound with the  $M'M'$  model, exhibit semiconducting behavior whereas others are metallic. Moreover, all models of the  $\text{Ti}_2\text{CO}_2$  exhibit semiconductors with energy gaps of less than 1.0 eV and vary slightly between them.

Furthermore, we note that Sc has a maximum oxidation state of +3, Ti has a maximum oxidation state of +4, V and Nb have a maximum oxidation state of +5, and Cr has a maximum oxidation state of +6, all of which are classified as positively charged transition metal atoms. Alternatively, C, F, and O are negatively oxidation states, with a charge of -4, -1, and -2, respectively. The  $\text{V}_2\text{CO}_2$ ,  $\text{Nb}_2\text{CO}_2$ ,  $\text{Cr}_2\text{CO}_2$ ,  $\text{Ti}_2\text{CF}_2$ ,  $\text{V}_2\text{CF}_2$ ,  $\text{Nb}_2\text{CF}_2$ , and  $\text{Cr}_2\text{CF}_2$  compounds perform as negative compounds with electron occupations in the d orbitals of the  $M$  transition metal due to charge state balancing. Because O requires more electrons than F functionalization, the Sc atom in the  $M'M'$  model cannot provide enough electrons for both attached  $M'$  sites in  $\text{Sc}_2\text{CO}_2$ . The PDOS of the  $\text{Sc}_2\text{CO}_2$  with the  $M'M'$  model, as shown in Figure 5.8, implies that because oxygen orbitals are devoid of electrons, electrons from the C-p orbital migrate to the O-p and Sc-d hybridization states. Certain C-p orbitals become electron deficient, as illustrated by the empty C-p orbitals above the fermi level. As a result, altering the oxygen atom from the  $M'$  site to above the Carbon atom ( $O$  site) is the most effective approach to get electrons from the O-p orbitals where the  $M'O$  model is an appropriate structure for  $\text{Sc}_2\text{CO}_2$ , as evidenced by the formation and total energy estimation. Similarly, the  $MM'$  and  $MM$  models exhibit electron deficiency in both O-p orbitals at the  $M$  site and C-p orbitals above the fermi level, indicating electron transfer from O or C atoms to Sc-d orbitals.

Additionally, the calculations reveal that the total DOS of  $M_2CT_2$  mainly contributes to the O-p and  $M$  transition metal sharing states. For example, the TDOS of  $\text{Ti}_2\text{CO}_2$  in Figure 5.9 clearly plots the shifting of occupied states from the  $M'M'$

model's lowest energy zone to the *MM* model's highest energy zone, with formation energies of -10.5869 and -5.3312 eV, respectively. The *M'M'* model's O-2p and M-3d orbitals have more frequently occupied states at the lowest energy region than the other models, implying that the *M'M'* model can be energetically favorable among the studied models. In the PDOS calculations for  $\text{Sc}_2\text{CO}_2$ ,  $\text{Sc}_2\text{CF}_2$ , and  $\text{Ti}_2\text{CF}_2$  MXenes, as shown in Figures 5.8, 5.13, and 5.14, respectively, show the obvious separation of O-p or F-p orbitals in the *MO*, *M'O*, and *MM'* models. They can be distinguished by the positions of O or F atoms on each surface side, while the PDOS of the other atoms, such as Sc, Ti, and C, remains largely unchanged. The PDOS in  $\text{Sc}_2\text{CF}_2$  and  $\text{Ti}_2\text{CF}_2$  also reveals that the F-p orbital for *M'M'*, *OO*, and *MM* models depicts the sequence of energy state features from the lowest to highest states, respectively, which is interestingly related to that of the tendency of the formation energies.

Furthermore, TDOS in the other  $M_2CT_2$  MXenes reveals a similar trend for the energy state feature of the *T*-p orbitals ( $T = \text{O}$  and  $\text{F}$ ), in which semiconducting compounds, such as  $\text{Sc}_2\text{CO}_2$ ,  $\text{Sc}_2\text{CF}_2$ ,  $\text{Ti}_2\text{CO}_2$ , and  $\text{Ti}_2\text{CF}_2$ , are more prominently shown than metallic compounds. As a general tendency, the model representing the major state of the *T*-p sharing orbitals at the lowest energy zone may be related to the lowest formation energy. The results also imply that the *T*-p orbitals may be performed as the influencing states that provide the most energetically stable structure. For example, especially in the case of the  $\text{Cr}_2\text{CF}_2$ , although the F-p orbitals of the *MM'*, *OO*, *M'O*, and *MO* models occur in the lower energy zone than that of the *MM* model, which has the lowest total energy among them.

#### 5.2.4 DOS plotting for different O-O length of $\text{Ti}_2\text{CO}_2$ and $\text{CO}_2$

It is proposed that the composition of surface functional groups plays an important role in determining the energetic properties of DOS and formation energy. The *M'* and *O* sites, which are hollow, allow the surface functionalized atom (*T*) to reach deeper than the *M* site, which is placed above the outmost transition metal atom. Therefore, the structure that has the *T* atomic composition constructed by the *M'* or *O* sites may perform as the thinnest structure while mostly exhibiting an

energetically favorable structure. Accordingly, the subsequent investigation is to explore the relationship between DOS and O position above the  $MX_2$  layer in the z-coordinate. The framework of  $Ti_2CO_2$  monolayer for the  $M'M'$  and  $OO$  models has been used for this reason. We perform the simulation by raising the height of oxygen functionalization atoms in the z-coordinate on both surface sides, while the  $M$  transition metal and carbon atoms will be fixed. The calculation details in this part are provided like those in the previous DOS computations. Figure 5.18 and 5.19 show PDOS with varieties of O-O distance in the z-coordinate of the  $Ti_2CO_2$  monolayer for the  $M'M'$  and  $OO$  models, respectively. On the other hand, the PDOS of  $CO_2$  with different O-O length is shown in Figure 5.20.



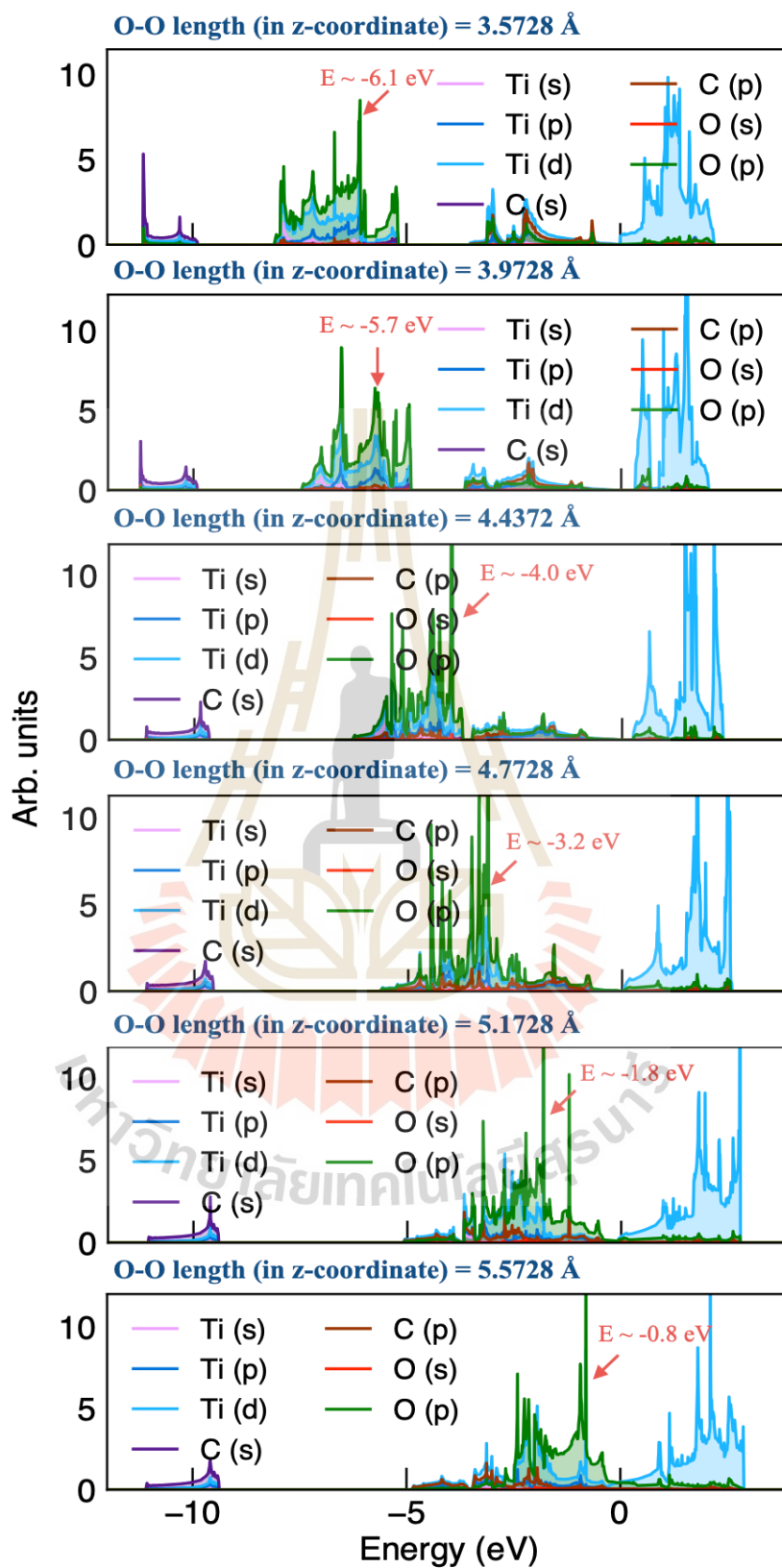


Figure 5.18 PDOS with different layer thickness of  $\text{Ti}_2\text{CO}_2$  monolayer for the  $M'M'$  model.

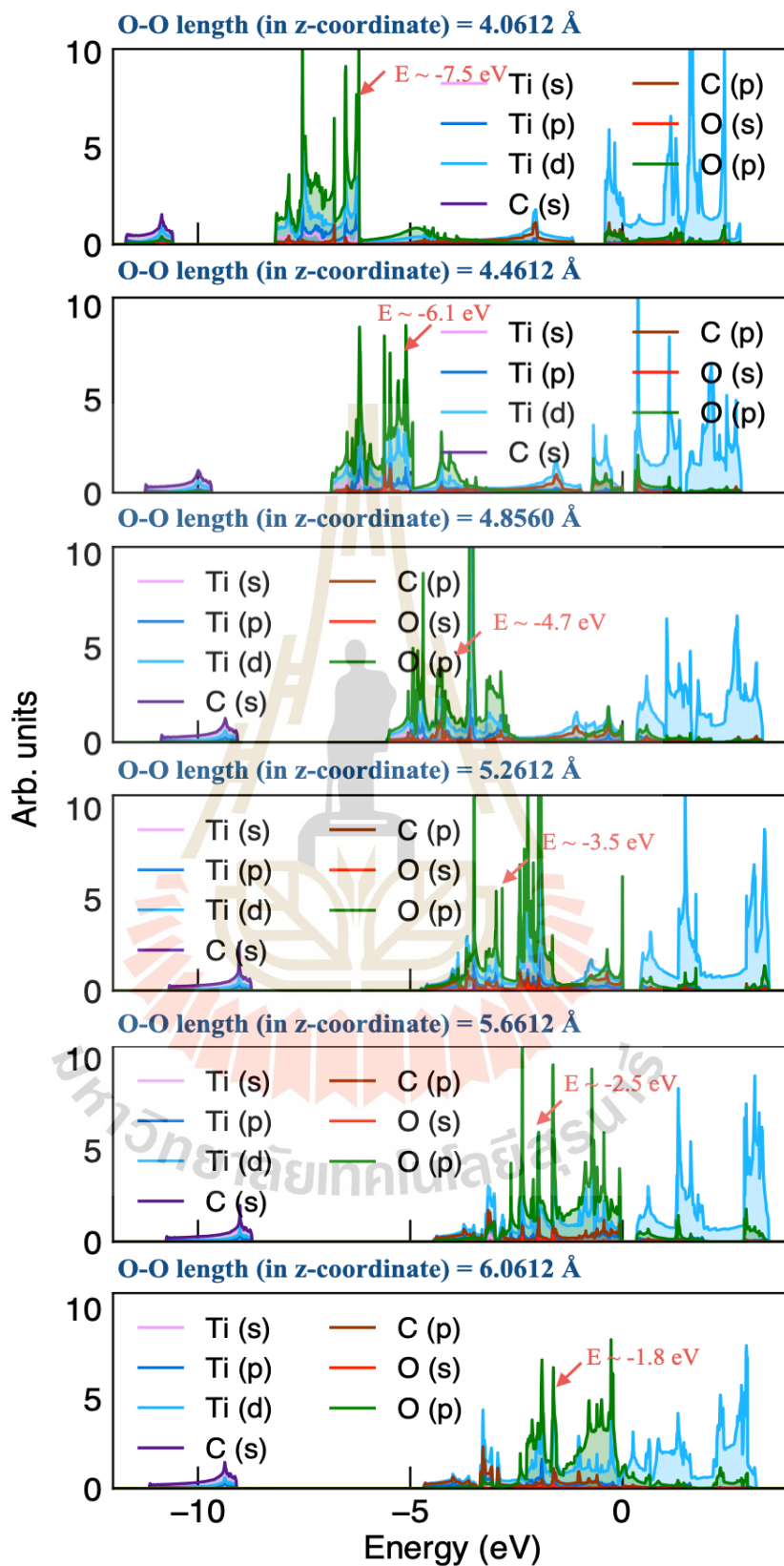


Figure 5.19 PDOS with different layer thickness of  $\text{Ti}_2\text{CO}_2$  monolayer for the OO model.

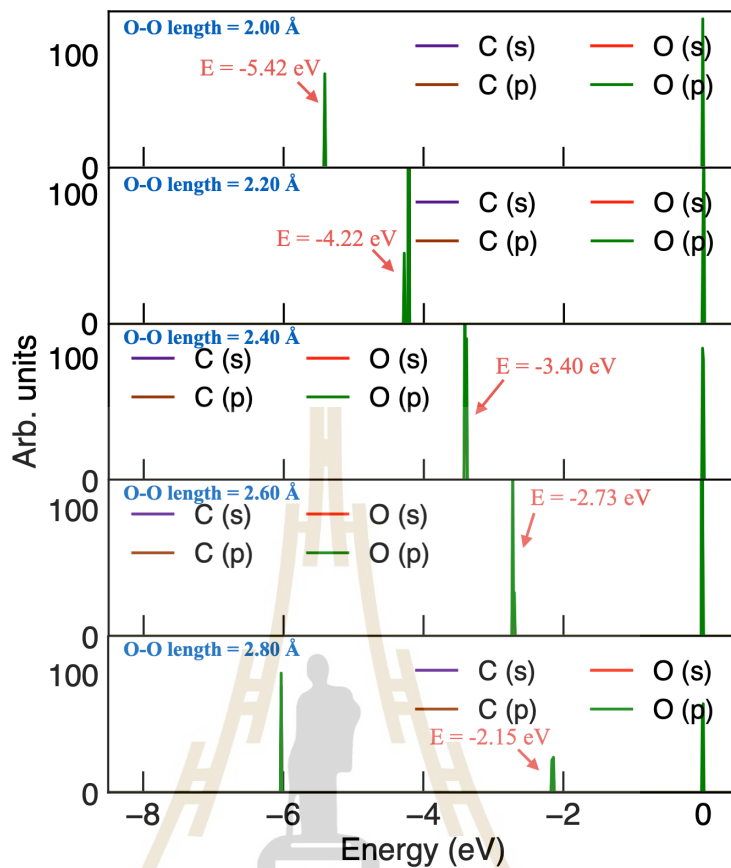


Figure 5.20 PDOS with different O-O length of  $\text{CO}_2$ .

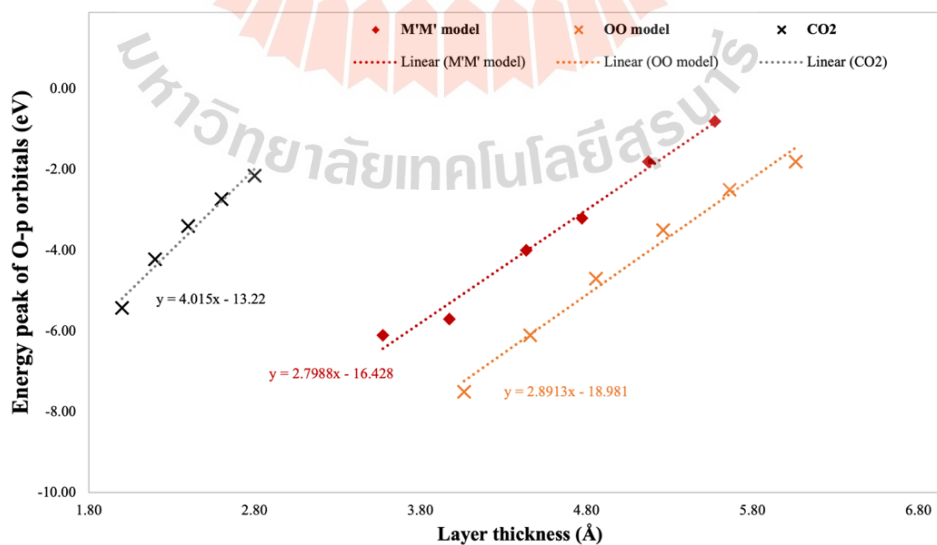


Figure 5.21 The identical peak state, as indicated in the arrow pointing, of the O-p orbitals of both  $M'M'$  and  $OO$  models of  $\text{Ti}_2\text{CO}_2$  monolayers and  $\text{CO}_2$ .

We note that the equilibrium structure for the  $M'M'$  and  $OO$  models of  $Ti_2CO_2$  correspond to the layer thickness of 4.4372 Å and 4.856 Å, respectively. The results show that the O-p orbitals of the  $M'M'$  and  $OO$  models are indicated by the identical peak state, which is represented by the arrow pointing in the figures. By plotting this energy peak state as a function of the layer thickness as shown in Figure 5.21, it is shown that the peak linearly moves as the O-O distance increases. Because of the increased bonding, the rest interaction between the O and the  $MC_2$  layer yields the higher energy of the O-p orbital. Therefore, we propose that the O-p energy state depends on the height of the O atom on the surface (layer thickness) in a similar manner to that of the  $CO_2$  molecule.

### 5.3 Discussion

In this section, the structural characteristics, and the electronic properties as well as their stability were investigated. We classified the monolayer's structural model as in the six forms that consist of  $M'M'$ ,  $M'O$ ,  $OO$ ,  $MM'$ ,  $MO$ , and  $MM$ . At first, we observed that  $M_2CT_2$  displays various characteristics in various compounds within its family, such as the switch from semiconducting to conducting by adjusting the  $T$  and  $M$  components, and the compositions of  $T$  atoms. For more insight into this finding, the trend of formation energy and DOS was further analyzed. It could be predicted that the relative structural stabilities of the  $M_2CT_2$  compounds were expected to be mainly influenced by the transition metal's ionic states. It is suggested that in the formation of the surface functional groups, the suitable  $M$  transition metal atoms would take precedence. These evidently had been found from the obvious oxidation state and formation energy estimations. Among the  $M_2CO_2$  and  $M_2CF_2$ , molecules with charge balance, such as  $Ti_2CO_2$  and  $Sc_2CF_2$ , maintain the highest stability. Furthermore, the type of structural models distinguished by surface functional group compositions took second precedence in the stability of the  $M_2CT_2$  structure. As a result, the formation energy calculation confirmed that most  $M'M'$  models perform the highest stability among the others. Additionally, the majority of the  $M'M'$ ,  $M'O$ , and  $OO$  models for the

$M_2CT_2$  MXenes, respectively, highlighted the preferable structure in terms of the analysis of the formation energy.

On the other hand, it should be concluded that the tendency of the reduced total energy was due to the DOS around the valence band edge shifting to the lower zone of the energy. The evidence showed that the DOS feature of  $M$ -d and  $T$ -p sharing orbitals of the  $M'M'$  models of the  $M_2CT_2$  compounds mostly takes place in the lowest energy region, which might give the lowest of the computed total and formation energies. In some cases, such as the  $Sc_2CO_2$ , alternative electron deficiency structures compound, with a negatively charged state of -2, attempted to relocate O closer to Sc and C atoms on one surface side. For example, the  $M'M'$ ,  $M'O$ , and  $OO$  models of  $Sc_2CO_2$ , had an opportunity that the C and O atoms might obtain the electrons that they required through the sharing orbitals. As a result, the DOS of the O-p, C-p, and Sc-d sharing orbitals in the  $M'O$  model had the lowest energy state and formation energy, resulting in the  $M'O$  model being the most preferred structure of the  $Sc_2CO_2$ . Furthermore, the F-p sharing orbitals of the  $M_2CF_2$  structures, where electrons were primarily attributed to the F-p and  $M$ -d orbitals, had generally constricted at a lower energy zone compared to that of the O-p state in the  $M_2CO_2$  structure. However, regarding the oxidation state and DOS of the  $M_2CF_2$  structure, the F-p orbital was unlikely to share electrons with the C atom, despite the F atom becoming closer to the C atom. This causes the F-p orbitals to have fewer altered features as the F atoms approach the C atoms rather than the transition metal atoms. For example, the DOS characteristic differed slightly between the  $M'M'$  and the  $OO$  models of the  $M_2CF_2$ , in which the  $OO$  model had the F atom closer to the C atom.

The relationship between DOS and the increasing height of O atoms above the layer for  $Ti_2CO_2$  was further presented. It was confirmed that the O-p state slightly shifted up as the height of the O atom in the z-coordinate above the surface increased. Consequently, it might be assumed that because of the  $M'M'$  model, that mostly have the thinnest structure, perform the best among all models of the  $M_2CT_2$  compounds in terms of stability. However, although the O-p orbital in the compound with the deepest of the O atoms occurred in the zone with the lowest energy state, it did not perform the lowest total energy due to the intermolecular distance between the two

oxygens. In particular, the models that merely shared by O-p, C-p, and *M*-d orbitals of the  $M_2CO_2$  appearing in the lowest energy zone, which was influenced by the O-p orbital, would be confirmed to have the energetically favorable structure. We concluded that the DOS of the surface functional groups, such as O-p and F-p sharing orbitals, and their locations heavily influence the stability of compounds. Finally, since the majority of the *M'M'*, *M'O*, and *OO* models performed the highest stability among the  $M_2CT_2$  MXenes, we therefore select these for the next calculations in which the integration of those models into the bilayer structures can then be expanded.



## CHAPTER VI

### STUDIES ON THE STRUCTURAL CHARACTERISTICS OF $M_2CT_2$ BILAYERS

In this chapter, the structural characteristics of bilayer  $M_2CT_2$  ( $M = \text{Sc, Ti, V, Nb,}$  and  $\text{Cr}$ ;  $T = \text{O}$  and  $\text{F}$ ) MXenes are investigated by employing the three types of monolayers from the previous chapter. This chapter firstly presents the structural parameter for simply identifying the bilayer system which contain the compounds, layer-layer combined types, and stacking configurations in a parameter. By considering the first and second outer atoms of the interface between the layers and operating the translation and rotation vectors to the overlying layer, the possibility of bilayer's stacking configurations is simplified. It has been discovered that the stacking configurations for different layer-layer combination types can be transformed into one another. Finally, the formation energy calculation of the various bilayer structures is presented. Interestingly, the  $M'M'-M'M'$  combined types of the bilayer as well as the  $s_1$  stacking configuration are found to be the most energetically favorable structures for the global estimation of the formation energy.

### 6.1 $X_{c,t,s}$ parameters for specifying bilayer structure

In this section, the integration of the selected models of the monolayer will be expanded, forming a bilayer structure. To make the bilayer structure comprehensible, it will be divided into three parts: compounds, layer-layer combined types, and stacking configurations. Therefore, we define  $X_{c,t,s}$  as a parameter which specifies the type for both atomic and co-ordinates of the bilayer system, where “ $c$ ” refers to the compound of the system, “ $t$ ” is the layer-layer combined types of the bilayer, and “ $s$ ” is the bilayer’s stacking configurations, as exemplified in Figure 6.1. The dark blue atom and the blue atom represent the foretop layer’s  $M_2$  atom and the bottom layer’s  $M_1$  atom, respectively, while the foretop layer’s  $T_2$  atom and the bottom layer’s  $T_1$  atom are orange and red, respectively. In addition, the integer “ $c$ ” composed of the 10 numbers of the interested compound which rearranged by  $\text{Sc}_2\text{CO}_2$ ,  $\text{Ti}_2\text{CO}_2$ ,  $\text{V}_2\text{CO}_2$ ,  $\text{Nb}_2\text{CO}_2$ ,  $\text{Cr}_2\text{CO}_2$ ,  $\text{Sc}_2\text{CF}_2$ ,  $\text{Ti}_2\text{CF}_2$ ,  $\text{V}_2\text{CF}_2$ ,  $\text{Nb}_2\text{CF}_2$ , and  $\text{Cr}_2\text{CF}_2$ , respectively. For example, the  $\text{Sc}_2\text{CO}_2$ ,  $\text{Ti}_2\text{CO}_2$ ,  $\text{V}_2\text{CO}_2$ ... and  $\text{Cr}_2\text{CF}_2$  compounds are equivalent to the “ $c$ ” integers of 1, 2, 3... and 10, respectively. The layer-layer combined types of the  $M_2CT_2$  bilayer in the unit cell are illustrated in Table 6.1 that formed by the combination of the  $M'M'$ ,  $M'O$ , and  $OO$  monolayer models, in which the “**bold**” letter indicates the closed interface types for both layers. Ten of the layer-layer combined types of the bilayer were categorized in terms of  $AM'-M'B$ ,  $AM'-OB$ , and  $AO-OB$  types of interfaces where  $M'M'-M'M'$ ,  $M'M'-M'O$ , and  $OM'-M'O$  belong to the  $AM'-M'B$  group;  $M'M'-OM'$ ,  $OM'-OM'$ ,  $M'M'-OO$ , and  $OM'-OO$ , belong to the  $AM'-OB$  group;  $M'O-OM'$ ,  $M'O-OO$ , and  $OO-OO$ , belong to the  $AO-OB$  group, in which  $A$  and  $B$  can be any surface form.

### Bilayer structure of $Ti_2CO_2$ compound

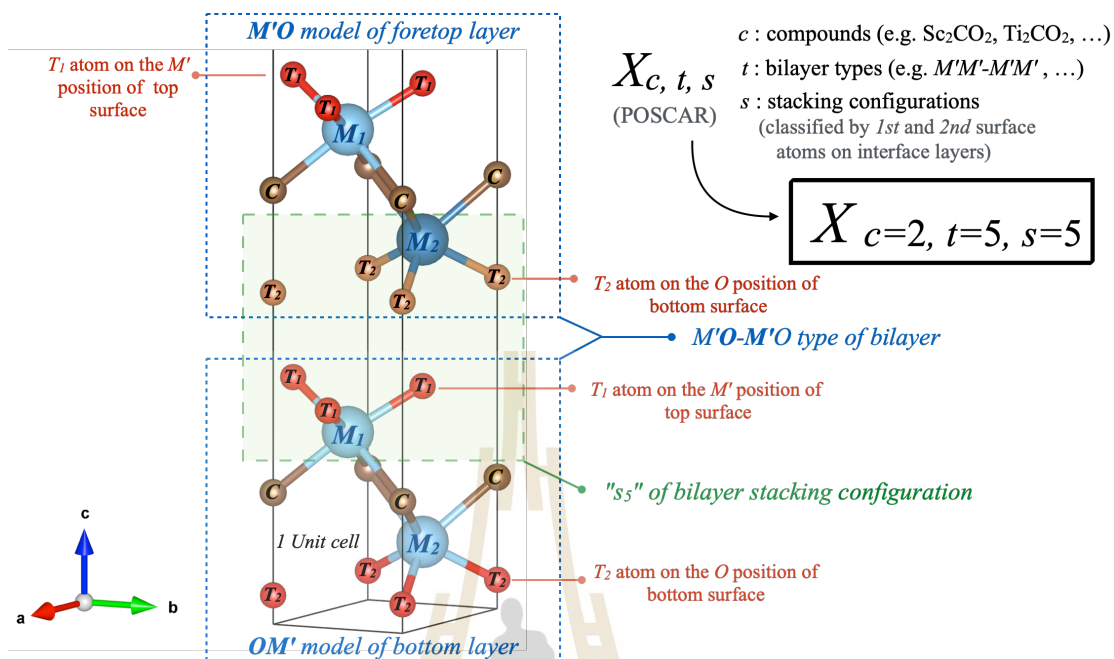


Figure 6.1 shows the  $X_{c,t,s}$  parameter, which is used for simply identifying the bilayer system. For example,  $X_{2,5,5}$  contain the  $Ti_2CO_2$  compounds, " $c = 2$ "; layer-layer combined types of  $M'M'-M'M'$ , " $t = 5$ "; and  $s_5$  stacking configurations, " $s = 5$ ".

**Table 6.1** present the combination of two single-layer of the  $M_2CT_2$  bilayer (where  $M$  is Sc, Ti, V, Nb, Cr and  $T$  is O, F) in the unit cell from the combination of the  $M'M'$ ,  $M'O$ , and  $OO$  monolayer models in which the “bold” letter indicate the closed interface types of both layers.

$t$	Combined bilayer types	
	foretop layer	bottom layer
1	$M'M'$	$M'M'$
2	$M'M'$	$M'O$
3	$M'M'$	$OM'$
4	$OM'$	$M'O$
5	$OM'$	$OM'$
6	$M'O$	$OM'$
7	$M'M'$	$OO$
8	$M'O$	$OO$
9	$OM'$	$OO$
10	$OO$	$OO$

## 6.2 Bilayer stacking configurations

To scan and identify all possible equilibrium structures for the bilayer formed by two single layers, including  $M'M'$ ,  $M'O$ , and  $OO$  models, the total energy for all possible stacking overlying layers would be examined. The self-consistency of the DFT computations is used to calculate the total energy of the  $Sc_2CO_2$ ,  $Ti_2CO_2$ , and  $V_2CO_2$  bilayers. The scan of the total energy along the  $12 \times 12$  divided grids in the  $x$  and  $y$  co-ordinates as a relative sliding site of the overlying layer are performed while the  $z$ -coordinate of the bilayer is allowed to relax. In addition, because the bilayer is chosen from the three-monolayer the lattice parameter of combined bilayer is determined by the average values of its counterpart layers. As a result, the three

related sites for the stacked overlaying layer are identical in the sample framework of  $AM'-M'B$ ,  $AM'-OB$ , and  $AO-OB$  groups (using the  $X_{c,t}$  for  $c = 1, 2, 3$  and  $t = 1, 5, 10$ ). By considering the translation and rotation vectors as included in the following, our result may also be further described in terms of structural transformations within the six specific types of bilayers stacking configurations.

### 6.2.1 Energy profiles of relative sliding for the overlaying layer

Initially, the stacking coordinate of the overlaying layer that is relative to the underlying layer is defined as the overlaying layer's translation. A direct stacking bilayer with respect to the corresponding of both C atoms in  $x$  and  $y$  coordinates from both layers (the overlaying layer's translation of  $\Delta a = 0$  and  $\Delta b = 0$  coordinate) is referred to by its energy of (0,0) coordinate. In addition, the energy landscape for the stacking of the overlaying layer sites in terms of total energy is included in Figure 6.3, while the correlated illustration structure for that of the stacking bilayer is shown in Figure 6.2. The results reveal that three overlaying layer's translations of (0, 0), (1/3, 2/3), and (2/3, 1/3) coordinates can be achieved to be the computed favorable sites. In addition, the overlaying layer's translation of (0, 0), (2/3, 1/3), and (2/3, 1/3) coordinates give the lowest energy for the  $X_{c,t}$  parameter of  $X_{2,1}$ ,  $X_{2,5}$ , and  $X_{2,10}$ , respectively. However, different compounds may show up in different energy landscapes but still obtain favorable sites within the overlaying layer's translation of (0, 0), (1/3, 2/3), and (2/3, 1/3) coordinates. The supplementary information shows a similar tendency for the mapping of the total energy in the  $Sc_2CO_2$  (Figure S1) and  $V_2CO_2$  (Figure S2) bilayer compounds except for the  $X_{3,10}$  which indicates the different lowest energy in (1/3, 2/3) translation coordinate. According to this finding, to further explore the various stacking configurations, we would precisely consider these three symmetric sites and identify the relationship between them.

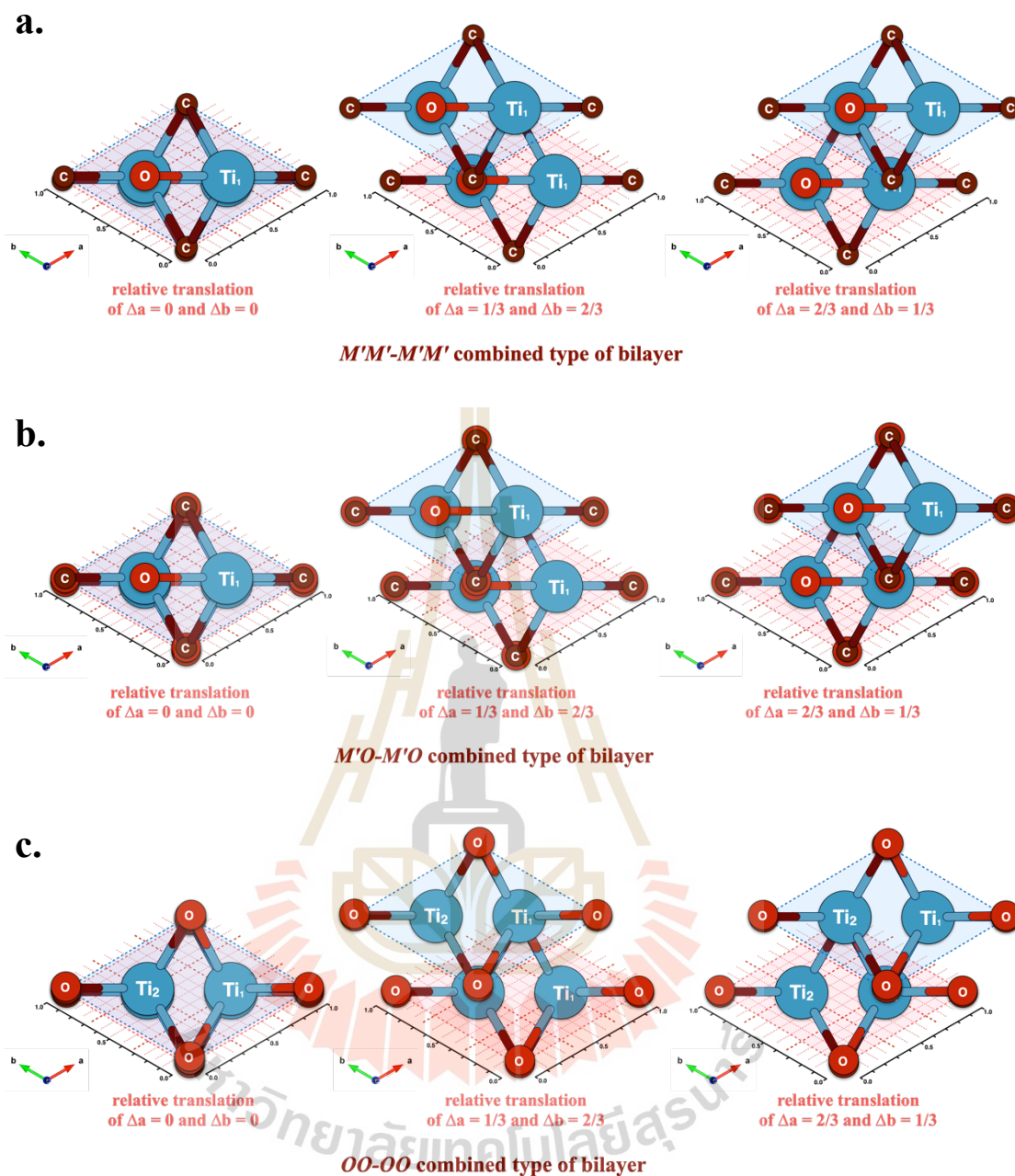


**Figure 6.2** Top-down views of the overlying layer's translation of the MXenes bilayer along the fixed underlying layer with the (a) *M'M'-M'M'*, (b) *M'O-M'O*, and (c) *OO-OO* bilayer's combined types of the  $\text{Ti}_2\text{CO}_2$ .

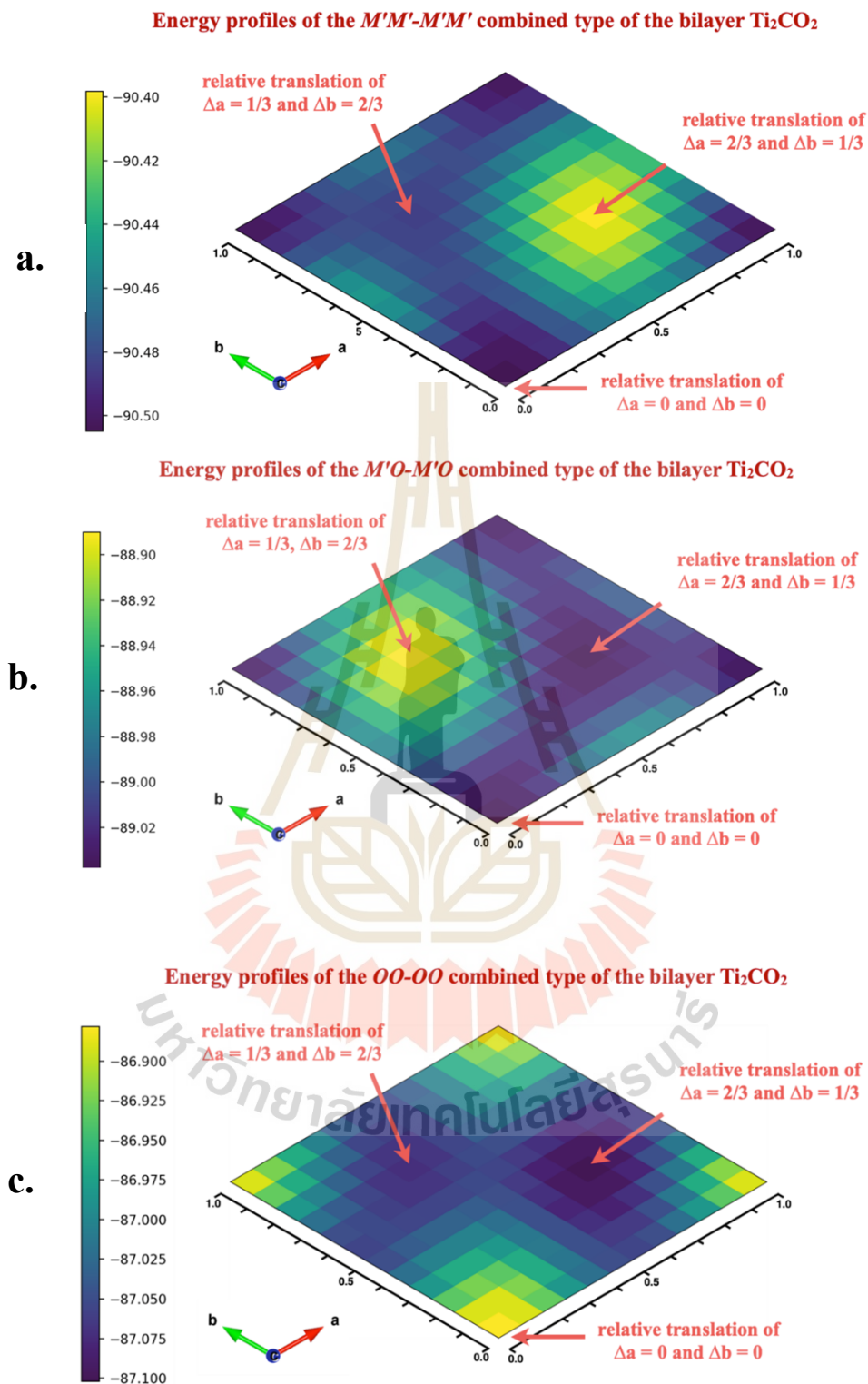


**Figure 6.3** Energy profiles of the overlying layer's translation for the (a)  $M'M'-M'M'$ , (b)  $M'O-M'O$ , and (c)  $OO-OO$  bilayer's combined types of the  $Ti_2CO_2$ .

## 6.2.2 Translation and rotation vectors

We noted that the overlying layer's translation for  $(0, 0)$ ,  $(1/3, 2/3)$ , and  $(2/3, 1/3)$  distances had been revealed as the significant symmetric structure. However, the computations for the overlying layer's translation in the  $x$  and  $y$  coordinates may not cover all conceivable stacking configurations. Therefore, the rotation for the overlying layer must be also considered. In this section, we analyzed the overlying layer's translation and rotation vectors as well as their correlations. Translation vectors are redefined by a vector in  $x$  and  $y$  coordinates that begins from the underlying layer's  $T_2$  atom to the overlying layer's  $T_1$  atom by a size and direction equal to  $\mathbf{d}_n$  vector as illustrated in Figure 6.4(a). Furthermore, as shown in Figure 6.4(b), possible high symmetric translation vectors are composed of six directions for the  $\mathbf{d}_n$  vectors (where  $n = 1, 2, 3, 4, 5,$  and  $6$ ). It is shown that the translation of the overlying layer operated by the  $\mathbf{d}_1, \mathbf{d}_3,$  and  $\mathbf{d}_5$  vectors has a homogeneous structure, whereas the translation of the overlying layer operated by the  $\mathbf{d}_2, \mathbf{d}_4,$  and  $\mathbf{d}_6$  vectors has a different homogenous structure. Due to the  $\mathbf{d}_1$  and  $\mathbf{d}_4$  vectors, which are defined as  $2/3\mathbf{a}+1/3\mathbf{b}$  and  $-2/3\mathbf{a}-1/3\mathbf{b}$ , respectively, having the same size but taking place in the opposite direction, it may be reduced to one translation vector ( $\mathbf{d}$ ) as indicated in Figure 6.4(c). Therefore, the  $D_i$  operator is defined by the number of  $i$  times to displacing the overlying layer with the  $\mathbf{d}$  vector.

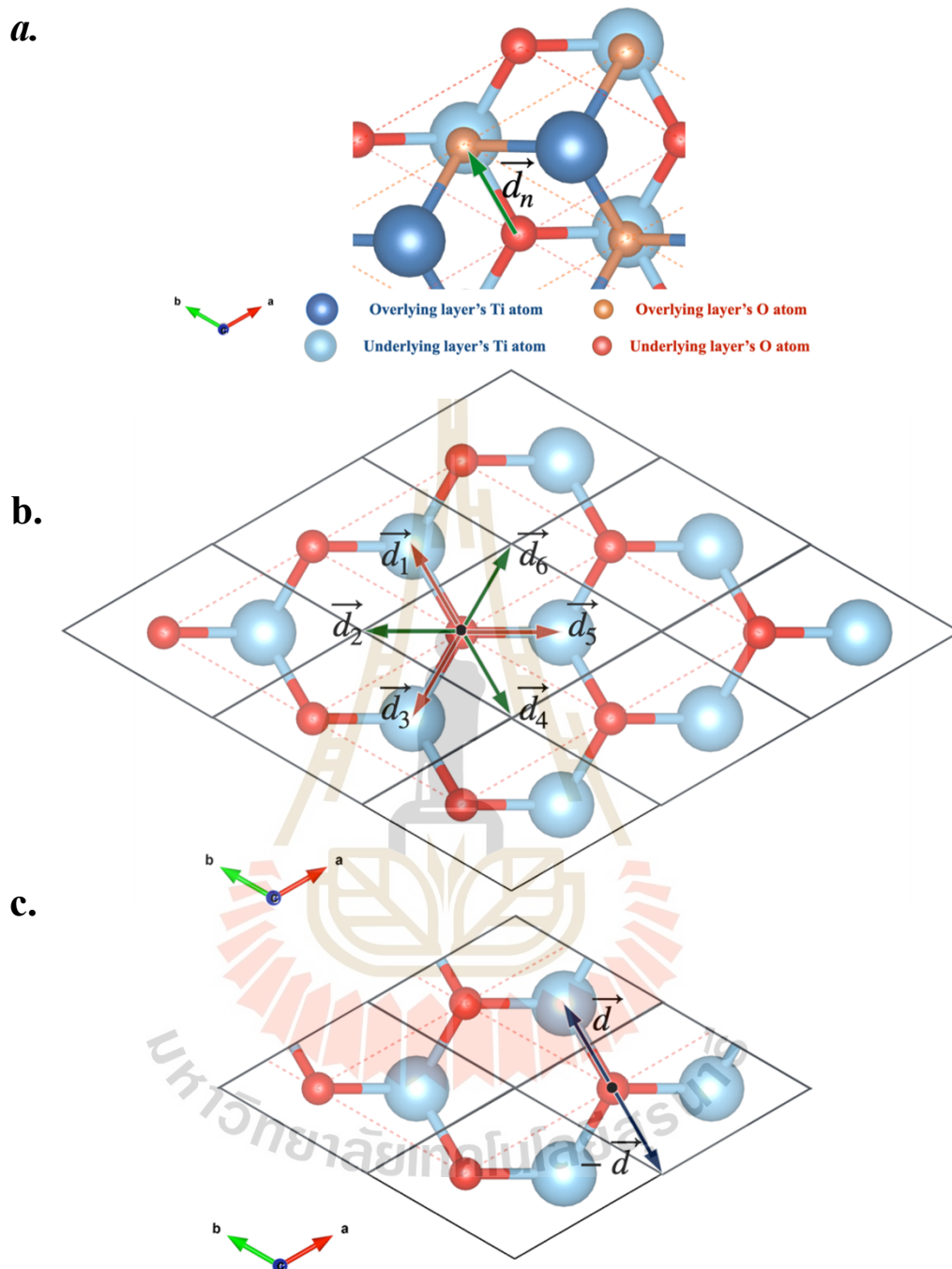


**Figure 6.4** Illustrations of the translation vectors in  $x$  and  $y$  coordinates include: (a)  $d_i$  vector that begins from the underlying layer's  $T_2$  atom to the overlying layer's  $T_1$  atom, (b) possible high symmetric translation vectors composed of six directions (where  $i = 1, 2, 3, 4, 5,$  and  $6$ ), and (c) a reducible vector of the  $d_i$  vector into  $d$  translation vector.

The rotation vector is defined by the counterclockwise rotation of the overlying layer with an angle of  $\theta$ , where a pivot point is at the overlying layer's  $T_2$ . The high symmetric structure of the bilayer's stacking configurations may also be obtained by operating the rotation vector with proportional to the  $\pi/3$  radian. The high symmetric structure of the bilayer's stacking configurations is given by

$$\theta_j = j \cdot \pi/3 \quad 6.1$$

where  $j$  is an integer indicating the number of the overlying layer rotation.

### 6.2.3 Structural transformations of the bilayer

By considering the first and second outer atoms of the interface between the layers, the stacking configurations are observed within the  $s_1 (X_{c,t,1})$ ,  $s_2 (X_{c,t,2})$ ,  $s_3 (X_{c,t,3})$ ,  $s_4 (X_{c,t,4})$ ,  $s_5 (X_{c,t,5})$ , and  $s_6 (X_{c,t,6})$  forms of the stacking configurations for the association of  $AM'-M'B$ ,  $AM'-OB$ , and  $AO-OB$  bilayer's combined types. For examples, side views and top-down views of the  $s_1$ ,  $s_2$ ,  $s_3$ ,  $s_4$ ,  $s_5$ , and  $s_6$  stacking configurations for the  $AM'-M'B$  bilayer's combined type are presented in Figure 6.5 and Figure 6.6, respectively. If we firstly consider the structure of the relative translation of (0, 0) coordinate for the  $AM'-M'B$ ,  $AM'-OB$ , and  $AO-OB$  bilayer's combined types, respectively, in Figure 6.2(a), (b), and (c), we found that it is related to the  $s_1$ ,  $s_5$ , and  $s_3$  stacking configurations. Moreover, for the  $AM'-M'B$  bilayer's combined type, the overlying layer's relative translation of (1/3, 2/3), and (2/3, 1/3) coordinates can be classified into  $s_2$ , and  $s_3$  stacking configurations, respectively. For the  $AO-OB$  bilayer's combined type in Figure 6.2(b), the overlying layer's relative translation of (1/3, 2/3), and (2/3, 1/3) coordinates are classified into  $s_2$ , and  $s_1$  stacking configurations, respectively. However, there are differences for the combined type of the  $AM'-OB$  bilayer. The overlying layer's relative translation of (1/3, 2/3), and (2/3, 1/3) coordinates are categorized into  $s_6$ , and  $s_4$  stacking configurations as shown in Figure 6.2 (c) and Figure 6.6.

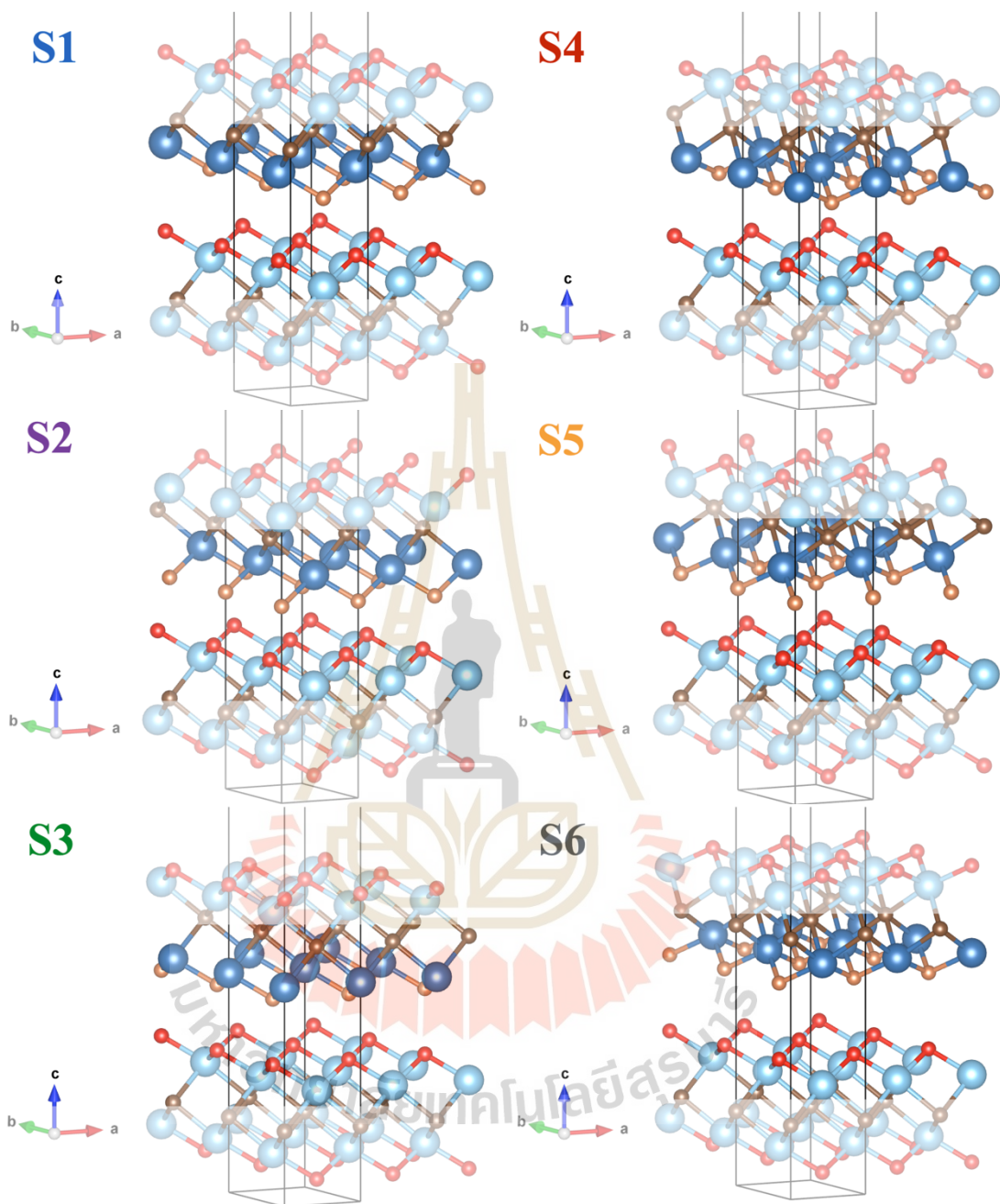


**Figure 6.5** Side view of in the  $s_1$ ,  $s_2$ ,  $s_3$ ,  $s_4$ ,  $s_5$ , and  $s_6$  stacking configurations of the AM'-MB bilayer's combined type.

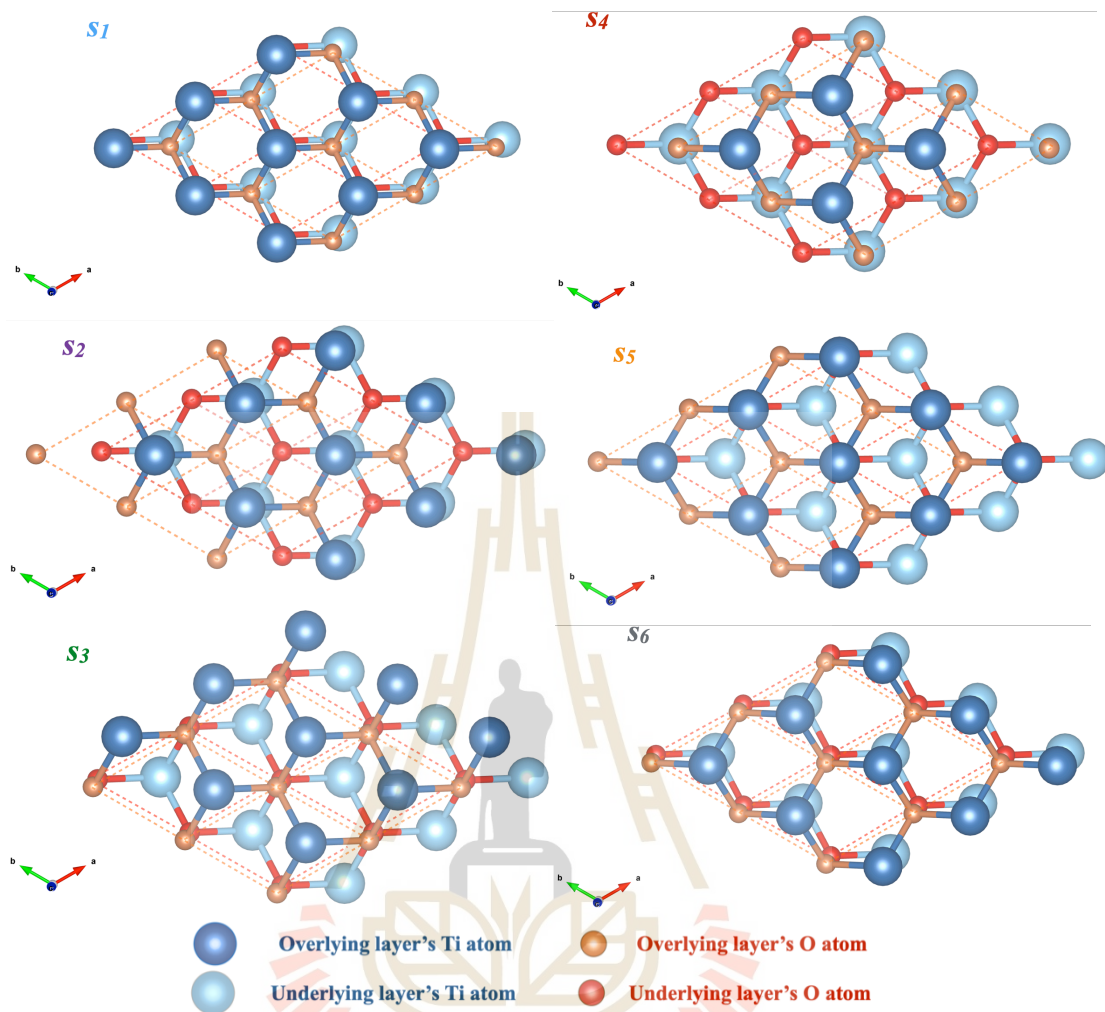


Figure 6.6 Top-down views of the  $s_1$ ,  $s_2$ ,  $s_3$ ,  $s_4$ ,  $s_5$ , and  $s_6$  stacking configurations.

It is found that for the  $AM'-M'B$ , as well as the  $AM'-OB$  bilayer's combined types, the  $s_1$  configuration operated by  $D_1$  and  $D_2$  (or  $-D_1$ ) can be transformed into the  $s_2$  and  $s_3$  configurations, respectively, that are given by

$$D_1 \cdot X_{c,t,1} = X_{c,t,2} \quad 6.2$$

$$D_2 \cdot X_{c,t,1} = X_{c,t,3} \text{ (or } -D_1 \cdot X_{c,t,1} = X_{c,t,3}) \quad 6.3$$

where  $t$  composes 1, 2, 3, 4, 5, 7 and 9. Meanwhile, the  $s_1$  operated by  $D_1$  (or  $-D_2$ ) and  $D_2$  (or  $-D_1$ ) can be transformed into the  $s_3$  and  $s_2$  configuration, respectively, for the  $AO-OB$  bilayer's combined type that are given by

$$D_1 \cdot X_{c,t,1} = X_{c,t,3} \text{ (or } -D_2 \cdot X_{c,t,1} = X_{c,t,3}) \quad 6.4$$

$$D_2 \cdot X_{c,t,1} = X_{c,t,2} \text{ (or } -D_1 \cdot X_{c,t,1} = X_{c,t,2}) \quad 6.5$$

where  $t$  composes of 6, 8, and 10. As a result, we can assume that the *AO-OB* bilayer's combined type performs inverse transformation while compared to the *AM'-M'B* and *AM'-OB* bilayer's combined types as concluded in Figure 6.7. In addition, initial stacking configurations at the relative translation of (0, 0) coordinate for the *AM'-M'B*, *AM'-OB*, and *AO-OB* bilayer's combined types are depicted in the light green border of Figure 6.7(a), (b), and (c), respectively.

Our finding further revealed that there are two specific rotation planes for the rotation of the overlying layer. The observations for the  $s_1$ ,  $s_2$ , and  $s_3$  stacking configurations in Figure 6.6 can be grouped into the first rotation plane, whereas those for the  $s_4$ ,  $s_5$ , and  $s_6$  configurations may be categorized into the second one. Interestingly, the rotation vector  $\theta_j$  operating on the overlying layer of the  $s_1$ ,  $s_2$ , and  $s_3$  stacking configurations can be transform into the  $s_4$ ,  $s_5$ , and  $s_6$  stacking configurations, respectively, which is given by

$$\theta_j \cdot X_{c,t,1} = X_{c,t,4} \quad 6.6$$

$$\theta_j \cdot X_{c,t,2} = X_{c,t,5} \quad 6.7$$

$$\theta_j \cdot X_{c,t,3} = X_{c,t,6} \quad 6.8$$

where  $j$  is an odd number (1,3,5... and so on),  $c$  and  $t$  are any integers. For example, as indicated in Figure 6.7, by varying the  $j$  integer by 1 step, the first rotation plane ( $s_1$ ,  $s_2$ , and  $s_3$ ) transforms into the second plane ( $s_4$ ,  $s_5$ , and  $s_6$ ). Besides, the rotation vector  $\theta_j$  operating on the overlying layer of the  $s_1$ ,  $s_2$ , and  $s_3$  stacking configurations is an identical operator where  $j$  is an even number (2, 4, 6... and so on), where an example is given by  $\theta_2 \cdot X_{c,t,1} = \theta_4 \cdot X_{c,t,1} = X_{c,t,1}$ . If we look at Figure 6.7's illustration, we can see how to change the interface forms of each combined type of the bilayer. However, Figure 6.7 (a), (b), and (c) merely demonstrate the similarity of the four interface atoms (the stacking configurations); nevertheless, the system's entire atomic compositions (used in the computation as POSCAR) are different. Namely, it would not notify us of the connection between the different combined types of the corresponding stacking configuration. For this reason, we can only conclude that the structural transformations with  $i = n+3$  and  $j = n+2$  as shown in Figure 6.8, where  $n$  is an integer and  $X_{c,t,sb}$  is any structural form, alternatively control the symmetry for the structural transformation in these hexagonal structures.

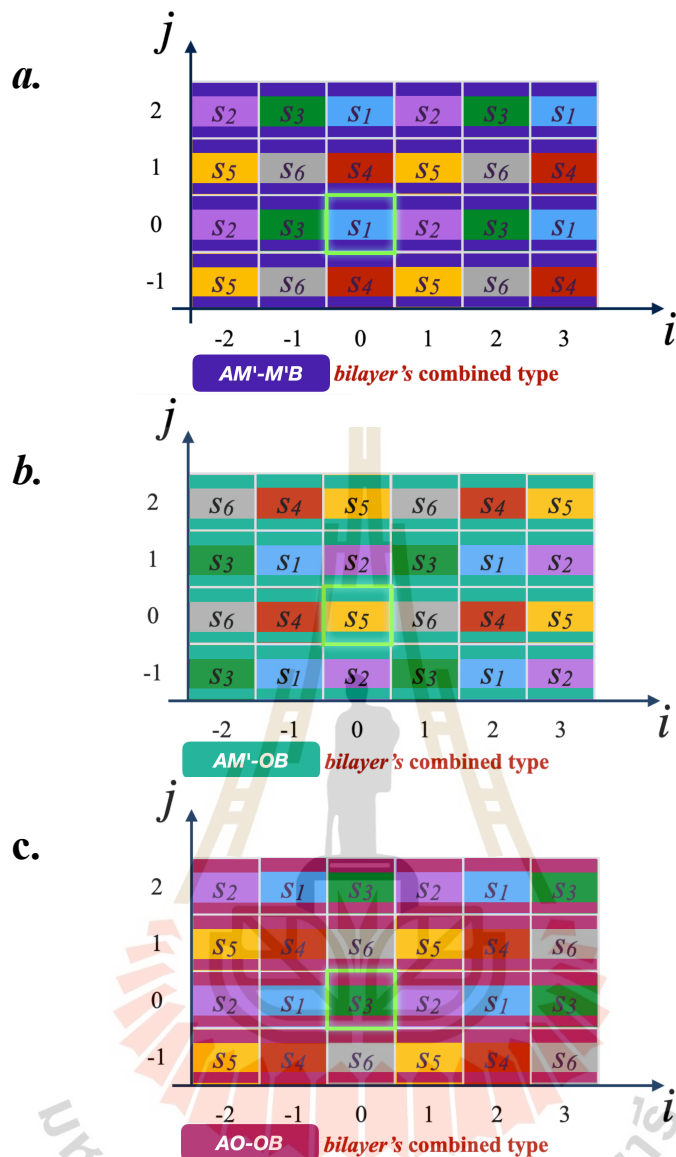


Figure 6.7 Simply implication for bilayer's stacking configuration transformation of (a)  $AM'-M'B$ , (b)  $AM'-OB$ , and (c)  $AO-OB$  bilayer's combined types where light green border corresponds to the relative translation of  $(0, 0)$  coordinate of Figure 6.2.

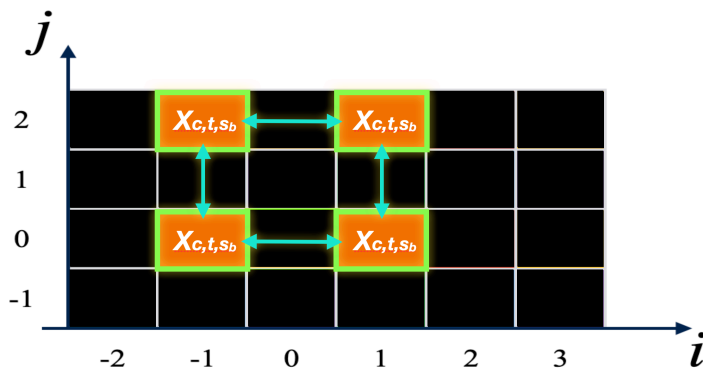


Figure 6.8 The symmetric structural transformations with  $i = n+3$  and  $j = n+2$ .

### 6.3 Formation and binding energies

To study the stability of the bilayer that is constructed by two bare-pristine layers and the  $T$  surface functional groups, the formation energy of the functional groups ( $E_f$ ) is a property used to quantify the adsorption stability of the specific functional groups on each structure. The formation energy may be defined as the required energy to separate the  $T$  functional group from the  $M_2CT_2$  bilayer, which is given by

$$E_f^{bilayer-M_2CT_2} = E^{bilayer-M_2CT_2} - 2E^{M_2C} - 4\frac{E^{T_x}}{x} \quad 6.9$$

where  $E^{bilayer-M_2CT_2}$ ,  $E^{M_2C}$ , and  $E^{T_x}$  are total energies of the  $M_2CT_2$  bilayer,  $M_2C$ , and  $T_x$  (in this work  $T_x$  is  $O_2$  or  $F_2$ ), respectively, obtained from the DFT calculations. Additionally, since ten numbers of the  $c$ , ten numbers of the  $t$ , and six numbers of the  $s$  are employed in the calculations, exactly 600 estimations for the formation energy are performed showing in Figure 6.9. Violet, dark blue, blue, cyan, green, light green, yellow, orange, red, and pink colors have been used to symbolize  $M'M'-M'O$ ,  $M'M'-OM'$ ,  $OM'-M'O$ ,  $OM'-OM'$ ,  $M'O-OM'$ ,  $M'M'-OO$ ,  $OM'-OO$ ,  $M'O-OO$ , and  $OO-OO$  combination types, respectively. Besides, the shading of the color of any layer-layer combination type in the plot indicates the stacking configurations, with most of the configurations consisting of the most energetically favorable classifications represented by darkened shading and the least energetically favorable types represented by lighter shading. We do, however, shift the energy scale in the  $y$ -axis to facilitate analysis, as shown in Figure 6.10. By doing this, in each compound, the structure consisting of the lowest formation energy must be shifted to 0 eV.

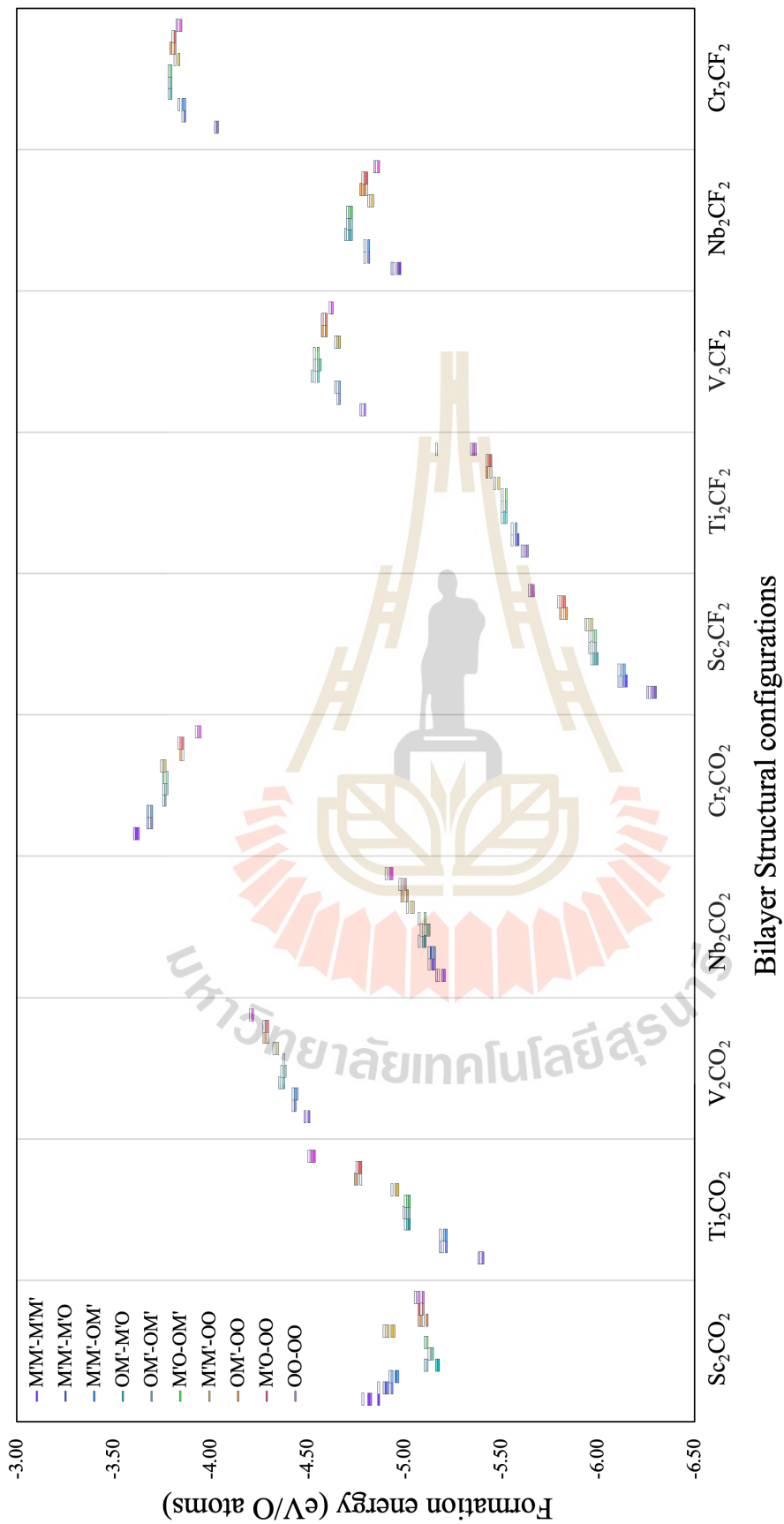


**Figure 6.9** Global estimation on the formation energy for the  $M'M'-M'O$ ,  $M'M'-O'M'$ ,  $O'M'-M'O$ ,  $O'M'-O'M'$ ,  $M'O-O'M'$ ,  $M'M'-O'O$ ,  $O'M'-O'O$ ,  $M'O-O'O$ ,  $O'O-O'O$ , and  $O'O-O'O$  combination types (violet, dark blue, cyan, blue, light green, green, yellow, orange, red, and pink colors, respectively), while the shading of the color of any layer-layer combination type in the plot indicates the various stacking configurations.

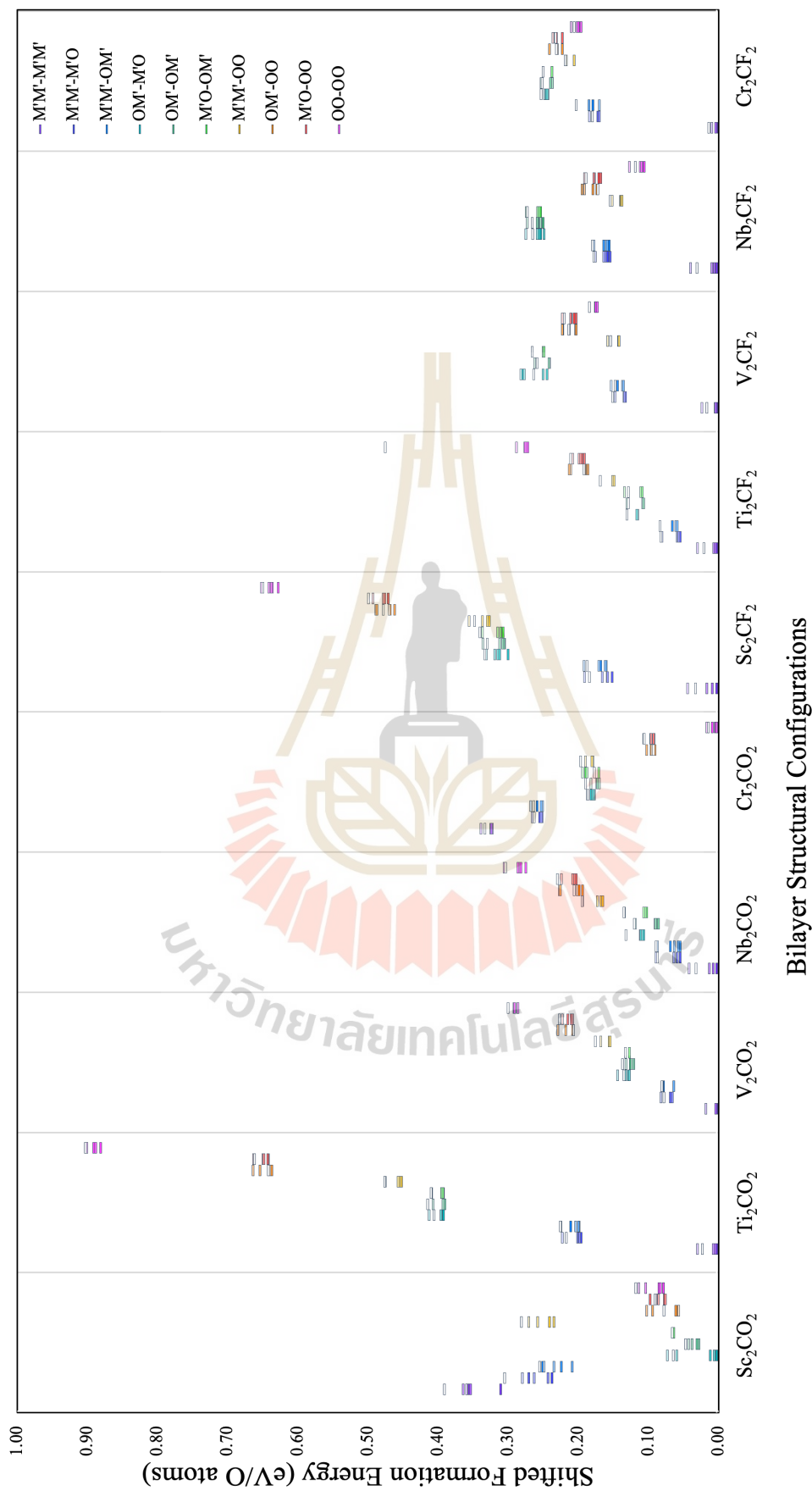


**Figure 6.10** Shifting of the global estimation on the formation energy where the lowest total energy in each compound had been shifted

**Table 6.2** Lowest formation energy of the bilayer structural configurations in each compound.

Compounds of the bilayer (“c”)	Bilayer’s Combined type (“t”)	Stacking configuration (“s”)	Formation energy (eV)
Sc <sub>2</sub> CO <sub>2</sub>	OM'-M'O	s <sub>1</sub>	-5.177
Ti <sub>2</sub> CO <sub>2</sub>	M'M'-M'M'	s <sub>1</sub>	-5.415
V <sub>2</sub> CO <sub>2</sub>	M'M'-M'M'	s <sub>1</sub>	-4.506
Nb <sub>2</sub> CO <sub>2</sub>	M'M'-M'M'	s <sub>1</sub>	-5.211
Cr <sub>2</sub> CO <sub>2</sub>	OO-OO	s <sub>5</sub>	-3.946
Sc <sub>2</sub> CF <sub>2</sub>	M'M'-M'M'	s <sub>1</sub>	-6.296
Ti <sub>2</sub> CF <sub>2</sub>	M'M'-M'M'	s <sub>1</sub>	-5.638
V <sub>2</sub> CF <sub>2</sub>	M'M'-M'M'	s <sub>1</sub>	-4.804
Nb <sub>2</sub> CF <sub>2</sub>	M'M'-M'M'	s <sub>1</sub>	-4.976
Cr <sub>2</sub> CF <sub>2</sub>	M'M'-M'M'	s <sub>1</sub>	-4.038

According to our finding, the Ti<sub>2</sub>CO<sub>2</sub> performs the lowest energy among the M<sub>2</sub>CO<sub>2</sub>, while the Sc<sub>2</sub>CO<sub>2</sub> has the lowest energy among the M<sub>2</sub>CF<sub>2</sub>. In addition, we include the computed information of the estimated formation energy for every compound in Table 6.2. The lowest formation energy of Sc<sub>2</sub>CO<sub>2</sub>, Ti<sub>2</sub>CO<sub>2</sub>, V<sub>2</sub>CO<sub>2</sub>, Nb<sub>2</sub>CO<sub>2</sub>, Cr<sub>2</sub>CO<sub>2</sub>, Sc<sub>2</sub>CF<sub>2</sub>, Ti<sub>2</sub>CF<sub>2</sub>, V<sub>2</sub>CF<sub>2</sub>, Nb<sub>2</sub>CF<sub>2</sub>, and Cr<sub>2</sub>CO<sub>2</sub> may be achieved, respectively, by -5.177, -5.415, -4.506, -5.211, -3.946, -6.296, -5.638, -4.804, -4.976, and -4.038 eV. All of those consist of the s<sub>1</sub> stacking configuration with M'M'-M'M' combined type except the Cr<sub>2</sub>CO<sub>2</sub> and Sc<sub>2</sub>CO<sub>2</sub>, which acquire the s<sub>1</sub> stacking configuration with OM'-M'O and the s<sub>1</sub> stacking configuration with OO-OO. The scope of energy between the lowest and highest is not greater than 0.4 eV and has a trend to decrease as the M (numbers of valence electrons) increases. However, two of them, including Ti<sub>2</sub>CO<sub>2</sub> and Sc<sub>2</sub>CF<sub>2</sub>, exhibit a large difference in energy (0.9 and 0.7 eV) that interestingly corresponds to the neutral charge for both compounds. According to our finding, there is a specific

pattern in the apparent formation energy for the different bilayer combination types, which are divided into 4 groups of features. For the lowest energy trend, these features mostly imply the  $M'M'-M'M'$  forms. The first feature represents the ordering energy trend from highest to lowest as corresponded to the  $M'M'-M'M'$  to  $OO-OO$  combination types, where this group includes  $Ti_2CO_2$ ,  $V_2CO_2$ ,  $Nb_2CO_2$ ,  $Sc_2CF_2$ , and  $Ti_2CF_2$ . The  $Cr_2CO_2$  shows the second feature, which is the opposite trend from the first feature.  $V_2CF_2$ ,  $Nb_2CF_2$  and  $Cr_2CF_2$  compounds exhibit similar trend and will be classified as the third feature. We can see that the  $M'M'-M'M'$  have the lowest energy, but the  $OM'-M'O$ ,  $OM'-OM'$ , and  $M'O-OM'$  seem to have the highest energy. In contrast to the third feature, the  $Sc_2CO_2$  compound's structure consists of  $OM'-M'O$ ,  $OM'-OM'$ , and  $M'O-OM'$ , having the lowest energy, while the  $M'M'-M'M'$ , having the highest energy, is arranged in the fourth feature.

In the formation energy trend for the bilayer's stacking configurations, interestingly, it is slightly altered as its configuration (2<sup>nd</sup> atomic order of the interface's composition) changes. When all the combined types of  $M_2CT_2$  bilayers are considered, the energy characteristics of the stacking configurations seem to follow an identical pattern. The  $s_1$  configuration emerges as the majority configuration, as shown in the plot, which may be depicted by the color's darkened shading. In addition, the  $s_4$ , which corresponds to the bilayer's overlying layer operated by the rotation vector of  $\pi/3$  radians of the  $s_1$  configuration, displays the second most favored configuration. We observed that the  $s_1$  appears to contribute to about 50 percent of the favored structure across all computations, whereas the  $s_4$  contributes to about 40 percent. Additionally,  $s_5$ ,  $s_2$ ,  $s_3$ , and  $s_6$  represent the high probability sequence of the formation energy from lower to higher. If we compared the tendency between the bilayer's combined type and the stacking configurations, the formation energy is changed more when we transform the combination type of the bilayer than when we transform the stacking configuration in a single compound. We may claim that the estimation of the formation energy has been influenced by the change in the combined type of the bilayer over the stacking configurations.

## 6.4 Discussion

The stability and structural characterization of the  $M_2CT_2$  bilayer were discussed in this section. Each bilayer compound's structural forms might be classified into two categories: combined types and stacking configurations which consisted of ten and six numbers, respectively. This proposed a way to understand the interrelationships between the structural arrangements in the  $M_2CT_2$  MXenes. The bilayer's interface consisted of 3 different groups of the combined types of  $AO-M'B$ ,  $AM'-M'B$ , and  $AO-OB$ , which consisted of exactly 18 stacking configurations and might be reduced to exactly 6 specific forms. We demonstrated that the specified translation or rotation vectors can turn the  $s_1$ ,  $s_2$ ,  $s_3$ ,  $s_4$ ,  $s_5$ , and  $s_6$  stacking configurations into one another. Furthermore, using the DFT calculation, which provided exactly 600 different structural computations, the global evaluated formation energy for every prospective structure was obtained. The research confirmed that the  $M'M'-M'M'$  bilayer's combined type tends to display the lowest formation energy, while the  $s_1$  indicated the most preferred among all varieties of the stacking configuration. As a result, the finding would be chosen for the subsequent section.

## CHAPTER VII

### STUDIES OF LI-ION AND CO-INTERCALATIONS IN MXENES

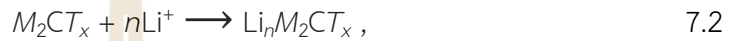
The study of Li-ion applications is presented in this chapter, which covers adsorption energy, voltage calculation, specific capacitance, and ionic mobility for both monolayer and bilayer  $M_2CT_2$  MXenes. Since Ti-transition metal based MXenes and the O functional group have attracted widespread attention, this chapter concentrates on the  $Ti_2CO_2$  compound as the computation framework. Initially, the adsorption energy, open circuit voltage (OCV) calculations, and specific capacitance for Li-ion storage in the  $Ti_2CO_2$  monolayer are presented, followed by a study of Li-ion ionic mobility along the monolayer and bilayer using structures chosen from prior structural relaxation. Moreover, the diffusion rate, which indicates the ability of atoms to diffuse into the bilayer MXenes, and the selectivity, which is defined as the relative of the diffusion rate, have been calculated by using the Arrhenius equation. Furthermore, choosing metals for co-intercalation in the bilayer  $Ti_2CO_2$  has been studied to investigate the length widened by intercalation. Consequently, the essential to the development of the MXenes bilayer's LIB properties has been discovered.

## 7.1 Adsorption energy and voltage calculation for the Li-ions reaction.

Calculating the adsorption energy,  $E_{ad}$ , which is directly proportional to the open circuit voltage (OCV), may be used to investigate an ion binding on the material (Meng *et al.*, 2017). The OCV estimation is given by

$$OCV \approx -\frac{\Delta E_{ad}}{n} \quad 7.1$$

where  $n$  is the number of adatoms inserted in the  $M_2CT_x$  MXenes. By utilizing the following reaction to calculate the OCV,



the corresponding  $E_{ad}$  involved in the adsorption process is defined as

$$E_{ad} = E_{Li_nM_2CT_x} - (nE_{Li} + E_{M_2CT_x}) \quad 7.3$$

where  $E_{Li_nM_2CT_x}$  is the total energy of the composite system with  $n$  numbers of the Li atoms adsorbed in the unit cell of  $M_2CT_x$ ;  $E_{Li}$  is the total energy of a single Li adatom; and  $E_{M_2CT_x}$  is the total energy of isolated  $M_2CT_x$ . It is reasonable to conclude that the large positive OCV implies energetically efficient adsorption. The reaction below would be implemented to obtain the OCV in the secondary layer of Li-adsorption, where  $n_1$  is the total number of Li atoms prior to insertion and  $n_2$  is the total number of Li atoms after insertion into the  $Li_{n_1}M_2CT_x$ .



$$OCV \approx -\frac{\left[ E_{Li_{n_2}M_2CT_x} - E_{Li_{n_1}M_2CT_x} - (n_2 - n_1)E_{Li} \right]}{n_2 - n_1} \quad 7.5$$

### 7.1.1 Results of the adsorption energy and the OCV calculations for Li-ions adsorption of the monolayer $Ti_2CO_2$

The OCV and adsorption energy of Li-ion calculations are evaluated for Li-ion adsorption into the  $M'M'$  structure of monolayer  $Ti_2CO_2$ . Figure 7.1 (a) depicts the possible first layer adsorption sites for Li adatoms on the surface of monolayer  $Ti_2CO_2$ , including at  $M_{ad1}$ ,  $C_{ad1}$  and  $O_{ad1}$  adsorption sites. The initial Li adatom is probably to be attracted on the  $M_{ad1}$ , and  $C_{ad1}$  adsorption sites. Due to the Li-adsorption energies on the  $M_{ad1}$  and  $C_{ad1}$  sites being -1.23 eV and -1.56 eV, respectively, the Li adatom

prefers the  $C_{ad1}$  site over the  $M_{ad1}$  site. Furthermore, by utilizing the  $C_{ad1}$  adsorption site as the first layer for the Li adatom, Figure 7.1(b) depicts the second layer for the sites of the Li adatom, including  $M_{ad2}$  and  $O_{ad2}$  adsorption sites. Therefore, the  $O_{ad2}$  site, which corresponds to an adsorption energy of around -0.03 eV, is selected as the Li adatom favorable site, as indicated in Table 7.1. Figure 7.2 shows the schematics of OCV calculations for the 1<sup>st</sup> and 2<sup>nd</sup> layers of Li-ion adsorptions of up to three adatoms into the monolayer  $Ti_2CO_2$ . Finally, the OCV and adsorption energy for the Li-ion adsorption, with the storage of three Li atoms in the monolayer  $Ti_2CO_2$ , are summarized in Figure 7.3.

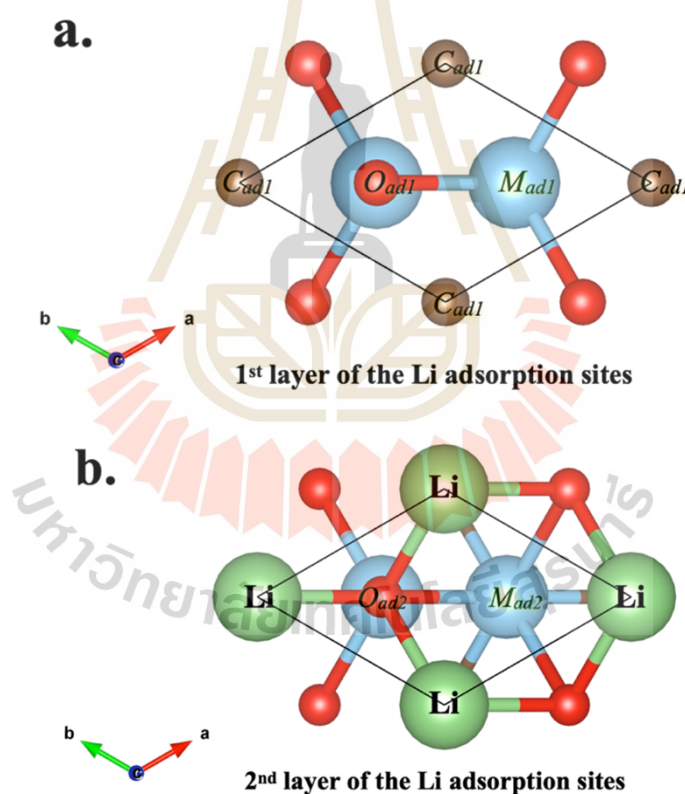


**Figure 7.1** indicate the top views of (a) Li adsorption site for the 1<sup>st</sup> layer and (b) Li adsorption site for the 2<sup>nd</sup> layer of the monolayer  $Ti_2CO_2$ .

**Table 7.1** The total energy and adsorption energy of the Li adsorption in the various sites for two Li adsorption layers.

Adsorption layer	Li adsorption sites	Total Energy (eV)	Adsorption energy (eV)
1 <sup>st</sup> layer	$C_{ad1}$	-48.53	-1.56
	$M_{ad1}$	-48.19	-1.23
	$O_{ad1}$	> -48.19	> -1.23
2 <sup>nd</sup> layer	$C_{ad2}$	-	-
	$O_{ad2}$	-53.84	-0.03
	$M_{ad2}$	-52.91	0.90

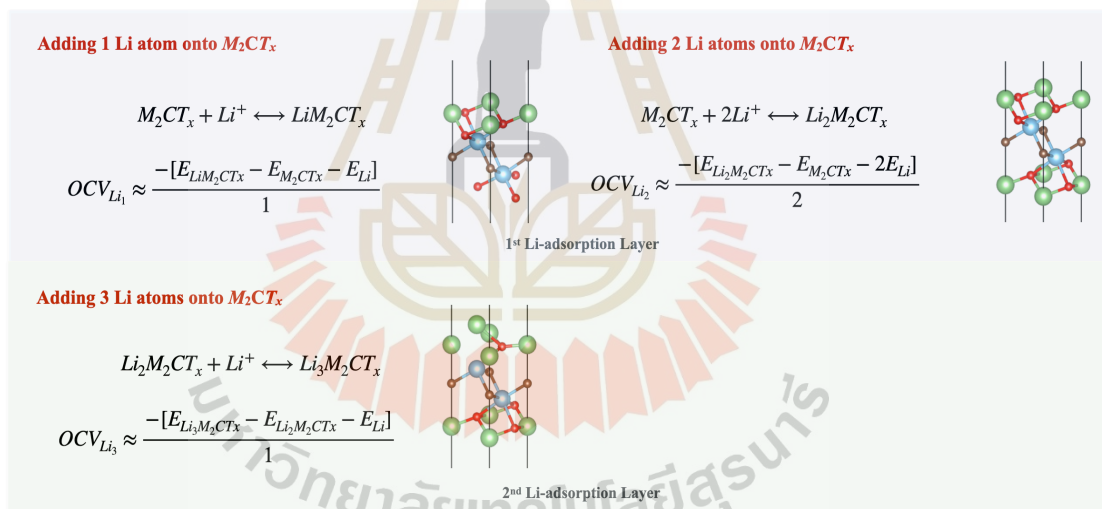


**Figure 7.2** The schematics of the OCV calculations for the first and second layers of Li-ion adsorptions in the monolayer  $Ti_2CO_2$

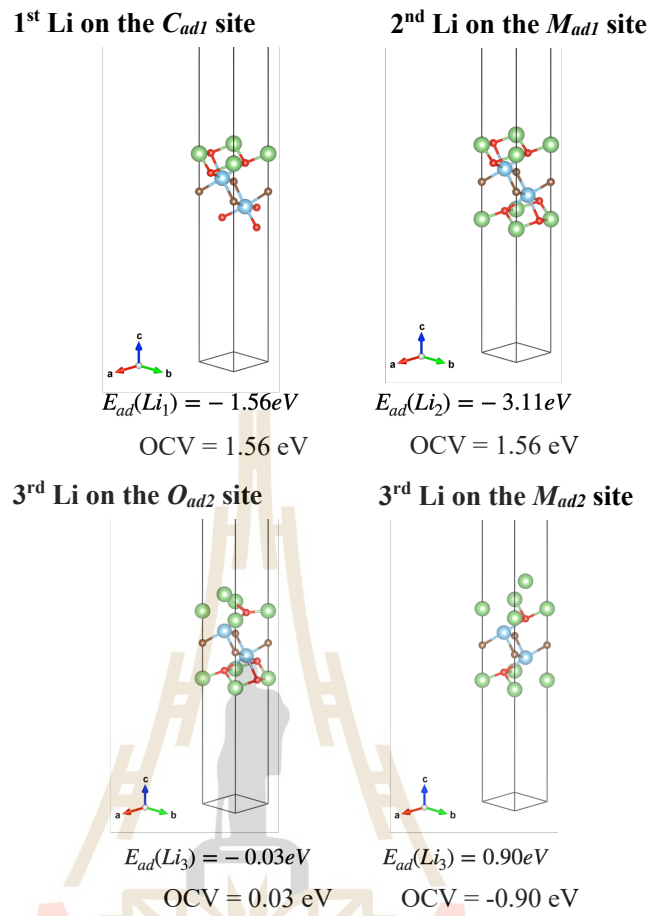


**Figure 7.3** The OCV and adsorption energy for Li-ions adsorption in the monolayer  $Ti_2CO_2$ .

### 7.1.2 Specific capacitance for Li-ions storage on Ti<sub>2</sub>CO<sub>2</sub>

The ability of a compound to store adatoms is referred to as its capacitance. At a given voltage, a material with a high capacitance may store more ions than one with a low capacitance. Gravimetric capacitance, which is the ratio of the system's Li-ions to the compound's mass, is included in the theoretical specific capacitance. The highest number of Li-ions adsorbed on the material with an adsorption energy and an OCV less than zero is referred to as the maximum value of the Li-ion adsorbed atoms. The gravimetric capacitance ( $C_g$ ) can be calculated by

$$C_g = \frac{nF}{M_{MXene} + nM_{Li}} \quad 7.6$$

Where  $M_{MXene}$  is the mass of the compound,  $M_{Li}$  is the mass of Li,  $n$  is the number of adsorbed Li atoms, and  $F$  is the Faraday's constant which equal to 96,485 C/mol. The computations of Li-ion storage on monolayer Ti<sub>2</sub>CO<sub>2</sub> were performed using 1, 2, and 3 atoms for Li-ions adsorbed on the unit cell, respectively, with gravimetric capacitances of 183, 349, and 500 mAh·g<sup>-1</sup>. Our result, referring to Li-ion storage for 2 atoms per unit cell of the monolayer Ti<sub>2</sub>CO<sub>2</sub>, is comparable to the publication by Eames and Islam and Xie et al., which details computation findings of around 350–383 mAh·g<sup>-1</sup> (Eames and Islam, 2014; Xie *et al.*, 2014).

**Table 7.2** Correlation of Specific capacitance, numbers of the Li adatom, and the open circuit voltage.

Number of Li adatom	OCV (eV)	Specific capacitance (mAh·g <sup>-1</sup> )
1	1.56	183
2	1.56	349
3	-0.03	500

## 7.2 Diffusion properties of Li-ion and metals co-intercalation of bilayer MXenes

The diffusion properties in this work consist of the diffusion barrier, the diffusion rate, and the relative diffusion rate (selectivity) for the Li-ion adsorption into the monolayer and the bilayer  $\text{Ti}_2\text{CO}_2$  MXenes. The static potential energy surface (SPES) and the climbing image nudged elastic band (CI-NEB) are used to explore diffusion barriers. Particularly, both methods are applied to the monolayer framework. According to the previous section, the  $M'M'-M'M'$  combination structure with the  $s_1$  stacking configuration is the most energetically favorable bilayer structure. It is chosen for studying Li-ion mobility as the intercalation framework for the  $\text{Ti}_2\text{CO}_2$  bilayer in the following subsection. The diffusion energy along two high-symmetric diffusion paths inside the  $\text{Ti}_2\text{CO}_2$  bilayer, including paths I and II, is analyzed. The total energy of distinct interlayer-spacings, later referred to as  $d$ -spacings, is used to identify the diffusion barrier for the bilayer  $\text{Ti}_2\text{CO}_2$  MXenes. Moreover, the diffusion rate of various  $d$ -spacings and the selectivity as a function of temperatures over the equilibrium state of Li atom intercalation at 50 K are also included where the final part presents the interlayer spacing related with metal intercalations with their selectivity over similar condition. In addition, the diffusion rate of various  $d$ -spacings and selectivity as a function of temperatures over the equilibrium state of Li atom intercalation at 50 K are included. The final part discusses the expansion of interlayer spacing associated with metal co-intercalations, as well as their selectivity over comparable situations.

### 7.2.1 Li-ion mobility for MXenes monolayers

By performing DFT calculations from VASP, SPES and CI-NEB methods, the diffusion barrier of the Li-ion in the material is obtained. The SPES method, that has been extensively used (Ashton *et al.*, 2016), is applied to single-point calculations for a Li atom at the surface of the monolayer MXenes. The supercell system has been used in the simulation to avoid an interaction of Li atoms in the periodic system. The  $\Gamma$ -centered Monkhorst-Pack  $k$ -mesh of  $2 \times 2 \times 1$  is performed for the BZ integrations in the  $3 \times 3 \times 1$  supercell computations, in which the vdW interactions are also

considered in the calculation. To evaluate the SPES diffusion barrier, we first split the grids along the diffusion path, then insert the Li-ions in those sites above the monolayer that are held fixed in x and y coordinates. After structural relaxation, their total energy is acquired. The SPES method is used when we want to obtain the equilibrium state total energy at the considered Li atom site. The difference in total energy between each site and the most energetically favorable site of the Li adsorbed atom across the diffusion path in the monolayer is described as the relative diffusion energy. Hence, the diffusion barrier will be specified as the Li site with the highest relative energy along transition path.

Figure 7.4 shows the diffusion path of the Li-ion moving along the surface of the  $\text{Ti}_2\text{CO}_2$  monolayer from the  $m_i$  to the  $m_t$  and, subsequently, to the  $m_i$  adsorption sites, where the  $m_i$  and  $m_t$  adsorption sites may refer to the initial state and transition state, respectively. It should be noted that the  $m_i$  and  $m_t$  adsorption sites may correlate to the  $C_{ad1}$  and  $M_{ad1}$  sites, respectively, in Figure 7.1 (a). The diffusion barrier is represented as a function of the relative energy variation as a function of diffusion distance, approximately eight translation steps, as illustrated in Figure 7.5 while the calculation information is included in Table 7.3. The computed diffusion barrier for the SPES and CI-NEB approaches is 0.223 eV and 0.215 eV, respectively, where the transition state is the  $m_t$  site implying at 0 Å of the diffusion coordinates in Figure 7.5. Moreover, the results reveal that both methods have identical phenomenological features, so we will choose one of the methods for the subsequent simulation. Our calculation value of around 0.2 eV is consistent with the literature from Zhang et al., which reports that the delaminated  $\text{Ti}_2\text{CO}_2$  system ( $d\text{-Ti}_2\text{CO}_2$ ) has a value of roughly 0.18 eV at the corresponding transition state location (Zhang *et al.*, 2017).

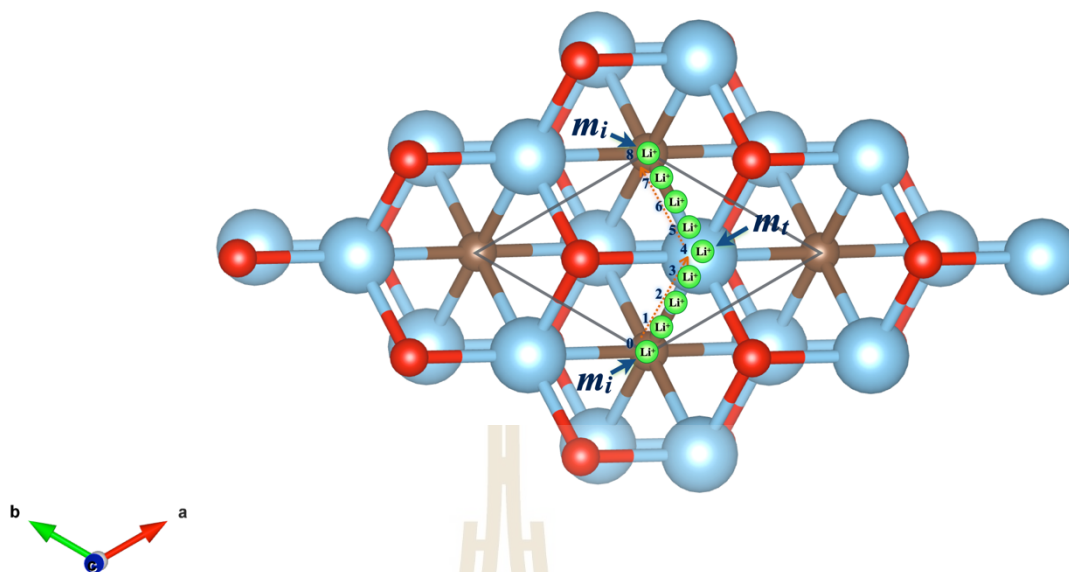


Figure 7.4 The Li atom moves from the  $m_i$  to the  $m_t$  and then to the  $m_i$  adsorption sites on the  $\text{Ti}_2\text{CO}_2$  monolayer's surface.

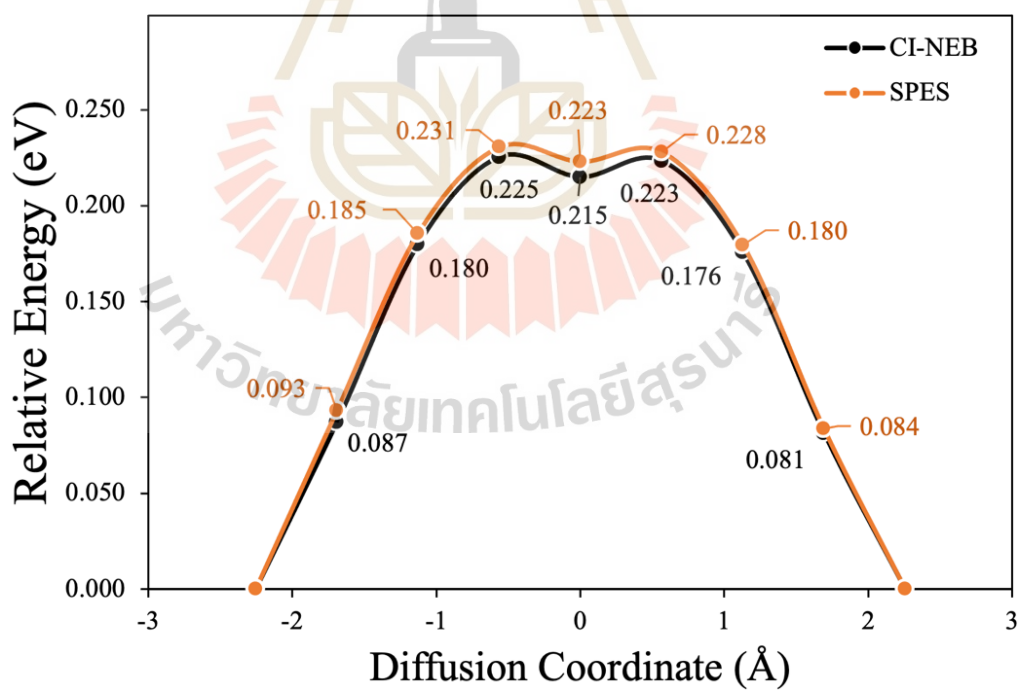


Figure 7.5 The relative energy along the diffusion path corresponds with Figure 7.4.

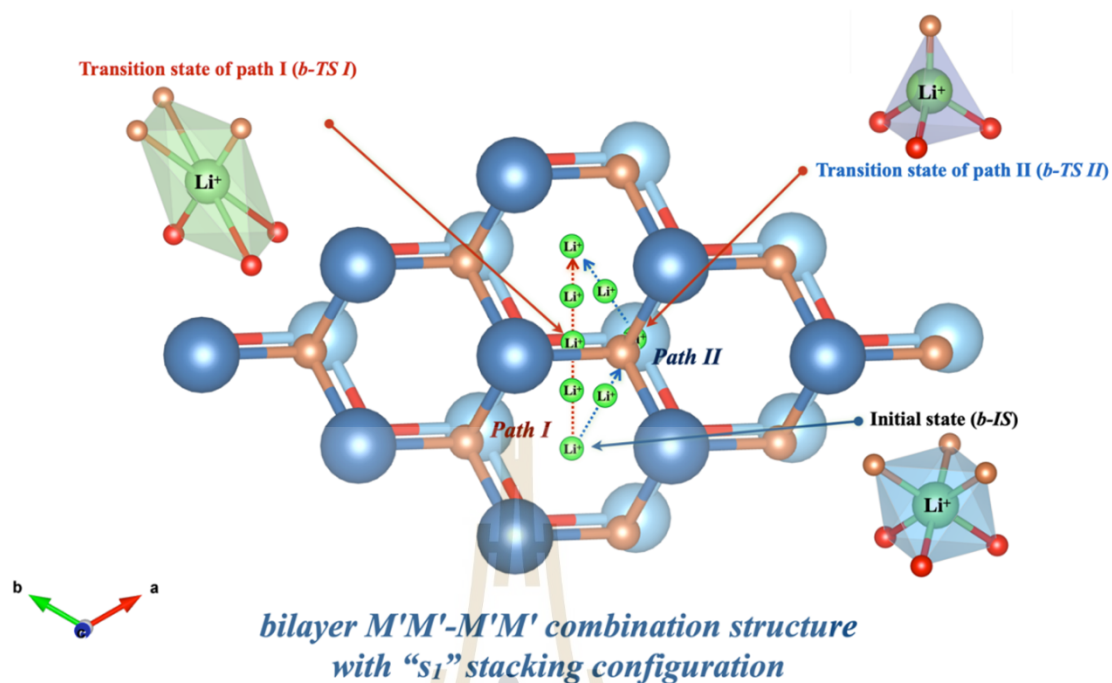
**Table 7.3** the relative energy and x, y coordinates

Steps	Diffusion coordinate (Å)	Total energy (eV)		Relative energy (eV)	
		SPES	CI-NEB	SPES	NEB
0 (initial)	-2.26	-410.698	-410.698	0.000	0.000
1	-1.69	-410.605	-410.611	0.093	0.089
2	-1.13	-410.513	-410.518	0.185	0.181
3	-0.56	-410.468	-410.473	0.231	0.227
4	0.00	-410.475	-410.483	0.223	0.223
5	0.56	-410.470	-410.475	0.228	0.227
6	1.13	-410.519	-410.523	0.180	0.181
7	1.69	-410.615	-410.617	0.084	0.089
8	2.26	-410.698	-410.698	0.000	0.000



## 7.2.2 Li-ions intercalated bilayer MXenes

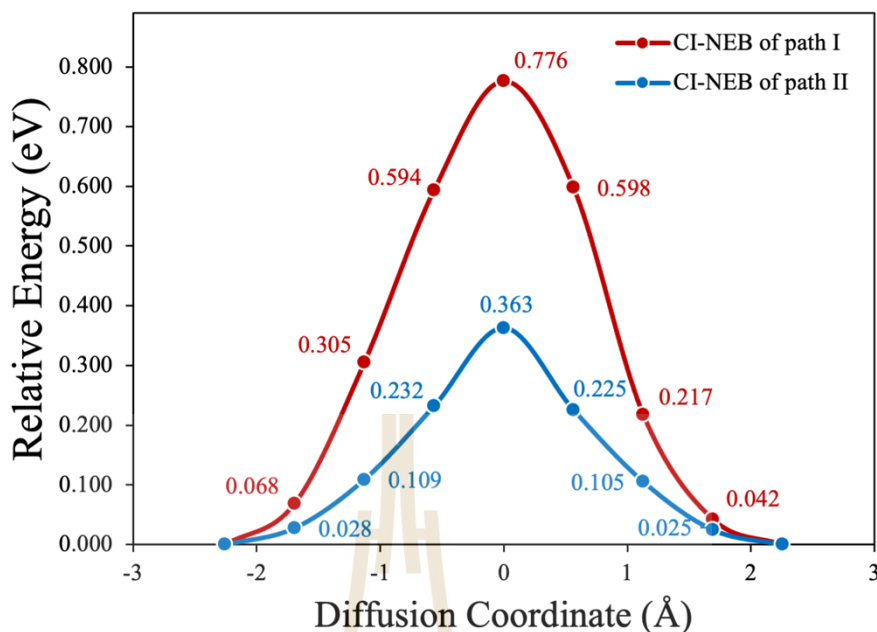
To evaluate the Li atom diffusion behavior inside the interlayer of the bilayer MXenes, the CI-NEB method and the SPES are priority used in the study. This presents the Li-ion diffusion paths for the  $M'M'-M'M'$  combination structure with the  $s_1$  stacking configuration of the  $Ti_2CO_2$  bilayer. The  $2 \times 2 \times 1$  supercell is appropriate for the bilayer calculation because it reduces computation costs while maintaining the distance between Li atoms. Moreover, the BZ integrations for the  $\Gamma$ -centered Monkhorst-Pack k-mesh of  $3 \times 3 \times 1$  are used. Unlike the monolayer, the diffusion paths for the bilayer have been partitioned into two high-symmetry routes: transition path I and path II, as shown in Figure 7.6, where the only second order of obstacle atom near the Li atom in the interface is shown. The  $b-TS I$  and  $b-TS II$  sites are the transition states of the diffusion path of path I and path II, respectively, as indicated by red arrows pointing in Figure 7.6. In addition, the energetically favorable adsorption location for the Li atom inside the bilayer  $Ti_2CO_2$  is identified as the bilayer initial state ( $b-IS$ ). The CI-NEB method is used to identify the relative diffusion energy as a function of the diffusion coordinate of the Li-ion for both diffusion paths, as illustrated in Figure 7.7, where Table 7.4 contains the calculation information. As a result, the computed diffusion barrier for the CI-NEB methods is 0.776 eV and 0.363 eV at the  $b-TS I$  and  $b-TS II$  transition state sites, respectively.



**Figure 7.6** The  $b$ -TS I (left red arrow) and  $b$ -TS II (right red arrow) sites are represented as the bilayer  $\text{Ti}_2\text{CO}_2$  transition states for the diffusion path of path I and path II, respectively, while the  $b$ -IS site is indicated by a dark blue arrow.

**Table 7.4** The relative diffusion energy as a function of diffusion coordinate of the transition path I and II for the  $\text{Ti}_2\text{CO}_2$  bilayer.

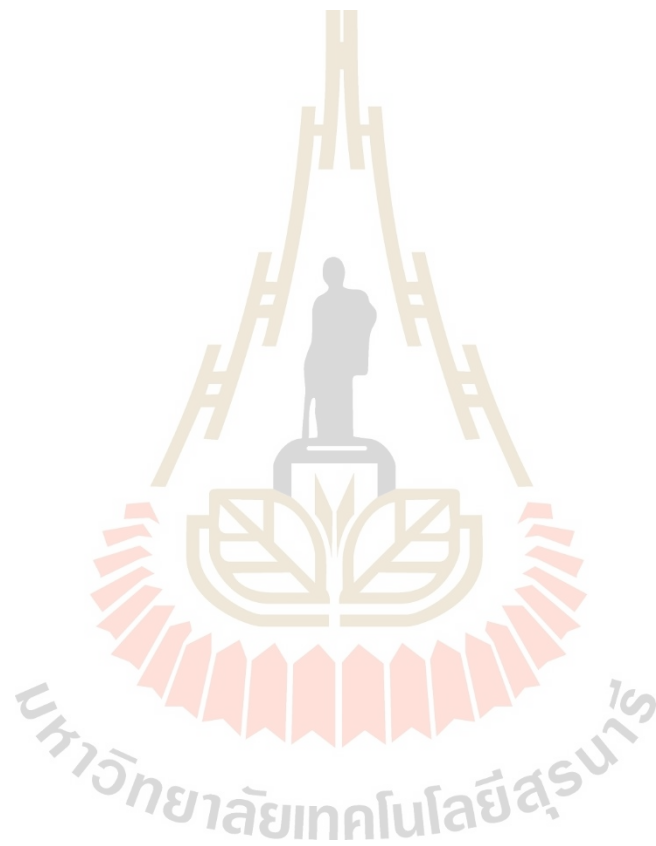
Steps	Diffusion coordinate (Å)	Total energy (eV)		Relative energy (eV)	
		Path I	Path II	Path I	Path II
0 (initial)	-2.26	-367.323	-367.323	0.000	0.000
1	-1.69	-367.255	-367.295	0.068	0.028
2	-1.13	-367.018	-367.214	0.305	0.109
3	-0.56	-366.730	-367.091	0.594	0.232
4	0.00	-366.547	-366.960	0.776	0.363
5	0.56	-366.725	-367.098	0.598	0.225
6	1.13	-367.106	-367.218	0.217	0.105
7	1.69	-367.281	-367.298	0.042	0.025
8	2.26	-367.323	-367.323	0.000	0.000



**Figure 7.7** Relative diffusion energy (eV) as a function of diffusion coordinate (Å) for the diffusion path I and path II (red and blue lines, respectively) simulated by CI-NEB method.

Furthermore, the framework for depicting the relative total energy for the *b-IS*, *b-TS I*, and *b-TS II* transition sites as a function of distinct interlayer-spacings, later referred to as *d*-spacing, is presented in Figure 7.8 by using the SPES method. This study seeks to find out how *d*-spacings affect the diffusion barriers in bilayer MXenes. In addition, the *b-IS* transition site for Li-ion is set for the reference energy, which is plotted as 0 eV in Figure 7.8. The distance in the *z*-coordinate between the overlaying and underlying functional groups (using oxygen atoms for this framework) that are far from or do not interact with the Li atoms of the interface surface, would be used to determine the *d*-spacing value. In practice, the interlayer is kept constant in the direction of the *c*-axis by anchoring the furthest Ti atoms from the Li-ion of each bilayer to preserve the *d*-spacing during computation. Besides, we provide a plot of the distance in *z*-coordinate between the Li atom and both layers for the *b-IS*, *b-TS I*, and *b-TS II* Li's transition sites, as shown in Figure 7.10. The green slope line in Figure 7.10 show the center distance between the overlaying and underlying layers that increases as the *d*-spacing rises. The horizontal lines represent the distance between the Li atom

and the monolayers for three different sites that correspond with the  $b-IS$ ,  $b-TS I$ , and  $b-TS II$  (gray, red, and blue lines, respectively). In addition, Table 7.5 includes the diffusion barriers calculated information according to the variation of energy as a function of interlayer spacing with two diffusion paths, as presented in Figure 7.9.



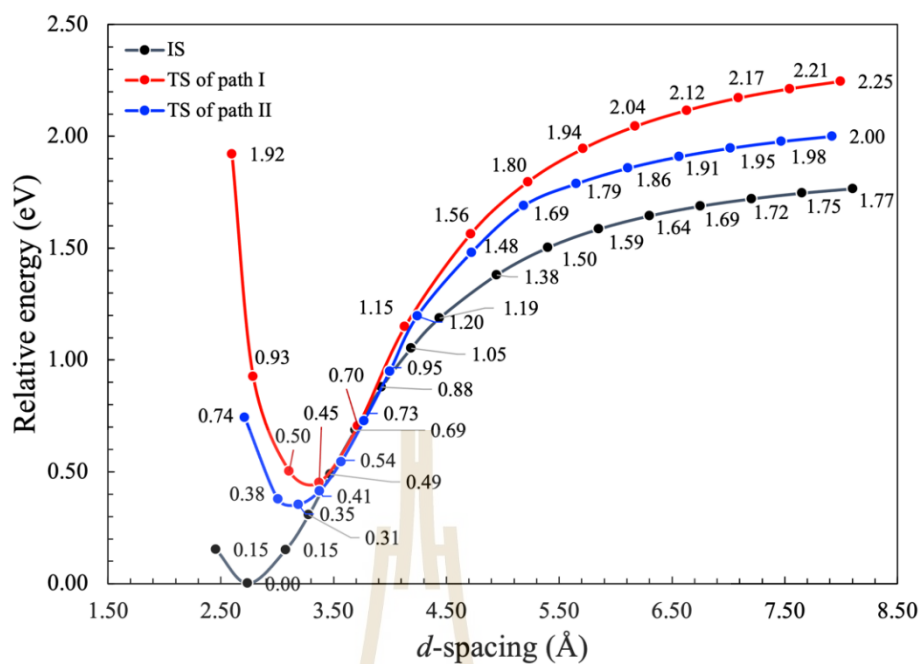


Figure 7.8 Relative energy of *b-IS*, *b-TS I*, and *b-TS II* Li's adsorption sites as a function of *d*-spacing (black, red, and blue lines, respectively).

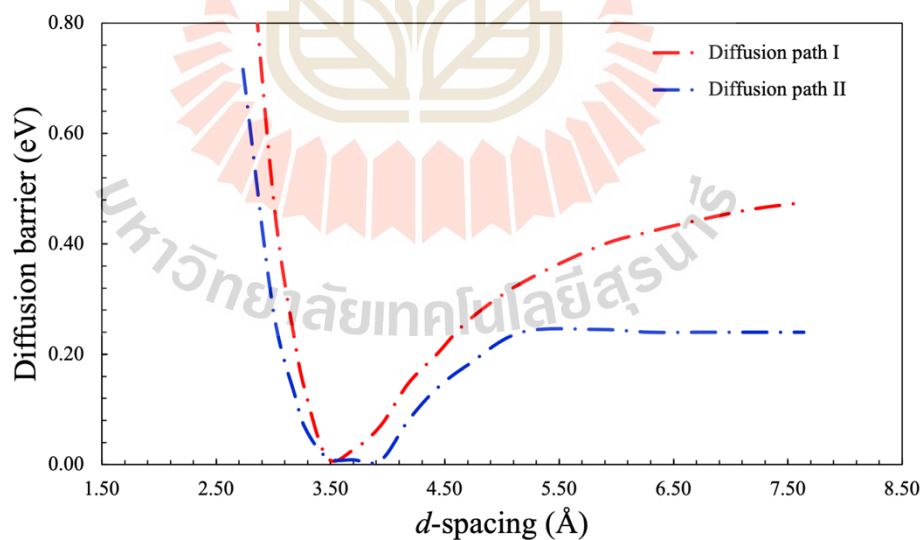
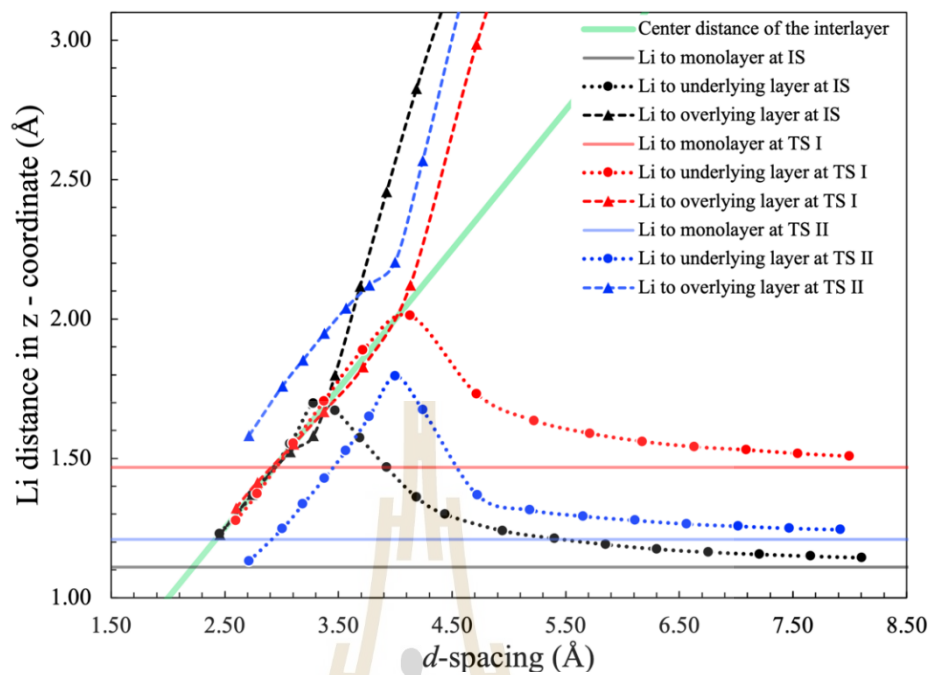


Figure 7.9 Relative diffusion barrier achieved by the differential energy between the transition state and the initial state at the same *d*-spacing for the diffusion path I and path II.



**Figure 7.10** The z-coordinate distance from the Li atom to both the underlying and overlying layers of *b-IS*, *b-TS I*, and *b-TS II* Li's adsorption sites as a function of the *d*-spacing.

**Table 7.5** Diffusion barrier information as a function of  $d$ -spacing along diffusion path I and path II.

$d$ -spacing (Å)	Diffusion barrier (eV)	
	Diffusion path I	Diffusion path II
2.74	1.107	0.716
3.00	0.485	0.280
3.19	0.222	0.125
3.28	0.133	0.066
3.47	0.013	0.013
3.70	0.027	0.009
3.94	0.071	0.008
4.18	0.147	0.080
4.43	0.200	0.138
4.71	0.262	0.182
5.17	0.329	0.240
5.85	0.396	0.245
6.29	0.422	0.240
6.74	0.444	0.240
7.19	0.463	0.240
7.64	0.475	0.240

Figure 7.8 present the equilibrium state of the Li-ion insertion at a  $d$ -spacing of 2.74 Å for the  $b$ -IS site while those for the  $b$ -TS I and  $b$ -TS II sites have  $d$ -spacings of 3.14 and 3.27 Å, respectively. If we assume that it has enough time to let the interlayer move to the proper state during the Li-ion diffusion, the energy from the equilibrium states of both Li atom transition states and the Li atom's initial state position is sufficient to generate the diffusion barrier. As a result, the diffusion barrier can be calculated as 0.44 and 0.35 eV for the transition paths I and II, respectively. However, since the distances between the two layers might practically move slower than the mobility of lithium ions, we therefore assume that the diffusion barrier, as shown in Figure 7.9, can be generated from the differential energy of the SPES method between the transition state and the initial state at the same  $d$ -spacing as in Figure 7.8. Thus, according to this approach for the  $b$ -TS I and  $b$ -TS II transition sites, the diffusion barriers were 1.02 eV and 0.68 eV (corresponding to  $d$ -spacings of 2.74 Å from the Li's equilibrium adsorption for the  $b$ -IS site), which were much more comparable with the CI-NEB method calculation (0.78 eV and 0.36 eV) than the previous method (0.44 eV and 0.35 eV). The diffusion barrier agrees well with Ashton *et al.*, who report the diffusion barrier for an identical diffusion path of the path I that yields 0.91 eV and 0.63 eV, respectively, for the SPES and CI-NEB methods (Ashton *et al.*, 2016). However, since the Li-atom is kept fixed at the center between two layers, they revealed that the diffusion barrier at the identical transition path II yields a higher diffusion barrier than that at the transition path I. In contrast, the Li-O bonding adopts a tetrahedral form and has a lower diffusion barrier than the transition path I if the Li-atom is not fixed as the center, which is consistent with our findings. Figure 7.8. also shows that when the  $d$ -spacing surpasses 5.50 Å, total energy increases significantly, and the diffusion barrier at the  $b$ -TS II transition site (0.24 eV) is essentially equal to that of the monolayer at an equivalent Li-adsorption site (0.22 eV).

We also provide a plot of the distance in the  $z$ -coordinate between the Li atom and both layers for the  $b$ -IS,  $b$ -TS I, and  $b$ -TS II Li's transition sites, as shown in Figure 7.10. The green slope line in Figure 7.10 shows the center distance between the overlying and underlying layers, which increases as a function of  $d$ -spacing. The horizontal lines represent the distance between the Li atom and the monolayers for

three different sites that correspond with the *b-IS*, *b-TS I*, and *b-TS II* (gray, red, and blue lines, respectively). According to our findings, the Li-O bonding forms a tetrahedral structure at the *b-TS II*.

It is interesting to note that the total energy at the *b-IS*, *b-TS I*, and *b-TS II* of the Li-transition sites exhibits similar ascending features, whereas the trend of these positions obviously overlaps with each other in the *d*-spacing range between 3.40 Å and 4.10 Å, indicating a near-zero diffusion barrier in this region. The near-zero diffusion barrier may be achieved for the following reasons: Firstly, the Li atom prefers to reside close to both layers, which is evident by the total energy for the equilibrium state in Figure 7.8 being lower as the Li atom is located at the center site and interacts equivalently with both the overlying and underlying layers as indicated in Figure 7.10. The Li atom at the *b-TS I* site is off center in the *z*-coordinate into one of the layers when the *d*-spacing reaches about 4.20 Å, with the same feature as the *b-TS II*, where the Li atom's center at the *b-TS II* represents the tetrahedral shape. The Li atom at the *b-IS* site (around the *d*-spacing of 3.40 Å), on the other hand, arrives off center before the *b-TS I* and *b-TS II* sites, resulting in a shorter duration of the evenly interact distance between the Li atom and both the overlying and underlying layers. Consequently, despite the equilibrium state at the *b-IS* site having the deepest energy, its energy increases faster than that for the *b-TS I* and *b-TS II* sites, appearing in energy overlap at around 3.40 to 4.10 eV in the *d*-spacing zone. The results show that it is important to examine the co-intercalations that will be valuable for extending the interlayer spacing.

### 7.2.3 Diffusion rate and Selectivity of Li-ions intercalated bilayer MXenes

The diffusion rate, or reaction rate, indicates the ability of atoms to diffuse into the electrodes of a variety of substances, which can reflect how quickly a battery can be charged. The diffusion rate can be estimated by using Arrhenius equation which is given by

$$k = A_0 e^{-E_b/k_B T}, \quad 7.7$$

where  $k$  is diffusion rate,  $A_0$  is diffusion pre-factor, which is constant obtaining from the experiment,  $k_B$  is the Boltzmann constant,  $E_b$  is the diffusion barrier, and  $T$  is temperature. According to the Arrhenius equation, the diffusion rate of the Li atom passing through the interlayer is a function of the diffusion barrier. As a result, the selectivity for Li-ion diffusion as a function of temperature is defined as the relative of the diffusion rate at a considered condition to the reference diffusion rate ( $k^*$ ) at 50 K. In addition, the reference diffusion rate is referred to the rate of the Li atom diffusion along the transition path II into the  $\text{Ti}_2\text{CO}_2$  bilayer by using the  $d$ -spacing of 2.74 Å ( $d'$ ), which corresponds to the optimized structure for Li insertion at the  $b$ - $1S$  site. Thus, the selectivity ( $S$ ) is given by

$$S = \frac{k_{d,T}}{k_{d',T=50K}^*} = \frac{A_0 e^{-E_b(d)/k_B T}}{A_0^* e^{-E_b(d')/50 \cdot k_B}}, \quad 7.8$$

where  $k_{d,T}$  is the diffusion rate of the identical  $d$ -spacing for the given  $T$  temperature,  $A_0$  is diffusion pre-factor,  $A_0^*$  is diffusion pre-factor of the reference diffusion rate,  $k_B$  is the Boltzmann constant, and  $E_b$  is the diffusion barrier. We know that the term of diffusion pre-factor of  $A_0 / A_0^*$  is constant for every simulation, but we don't know the exact values for a particular system. The selectivity can be quantified by arbitrarily defining the diffusion pre-factor as equal to 1. By using equation 7.8, we may primarily obtain the general features of the relative diffusion rate of the materials. Figure 7.11 shows the general characteristic of the relative diffusion rate calculated as a function of temperature, where the diffusion barrier of 0.74 eV, which corresponds to the  $d$ -spacing of 2.74 Å was used.

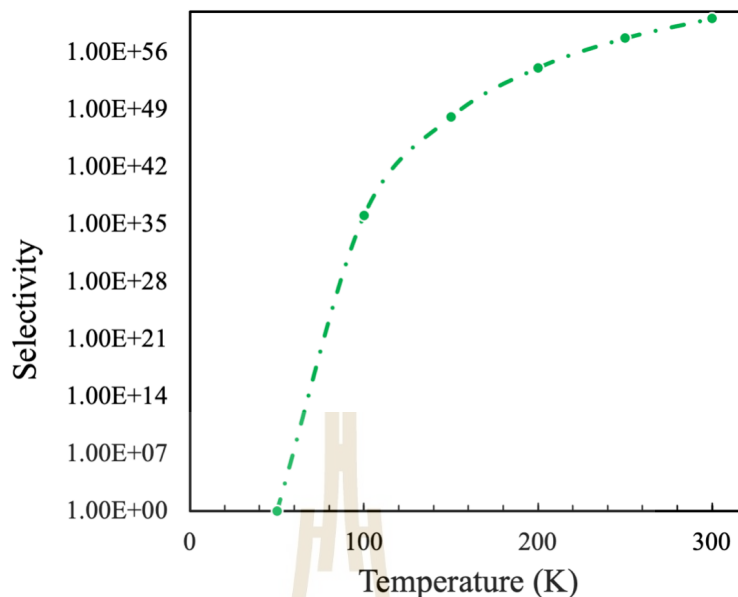


**Figure 7.11** The general characteristic of the relative diffusion rate as a function of temperature.

Furthermore, the calculated diffusion barrier and the selectivity (using transition Path II) of Li atom as a chosen temperature, including 50 K, 100 K, 200 K, and 300 K, are shown in Figures 7.12(a) and (b), respectively, in which the calculated information is listed in Table 7.6. The selectivity is shown to be greatly enhanced for all examined temperatures, reaching approximately 72 orders of magnitude when the  $d$ -spacing is below 3.50 Å. The feature is present at various temperatures simultaneously; however, it tends to be substantially amplified at low temperatures compared to high temperatures. We also found that the selectivity become constant as the  $d$ -spacing is above 5.50 Å, where the selectivity is obtained by 48, 60, 66, and 68 orders of magnitude for the temperature of 50 K, 100 K, 200 K and 300 K, respectively. Interestingly, the selectivity around the  $d$ -spacing range between 3.50 and 4.10 is relatively unchanged throughout the changes in temperature, allowing it to be used even at very low temperatures while preserving great performance for the diffusion characteristics.

**Table 7.6** The relationship between the diffusion barriers and the selectivity of various temperatures, including 50 K, 100 K, 200 K, and 300 K, as a function of the  $d$ -spacing.

$d$ -spacing (Å)	Diffusion barrier (eV)	Selectivity of Li-ion over equilibrium $d$ -spacing at T = 50 K			
		50 K	100 K	200 K	300 K
2.74	0.716	1.00	$1.22 \times 10^{36}$	$1.34 \times 10^{54}$	$1.39 \times 10^{60}$
3.00	0.280	$8.85 \times 10^{43}$	$1.14 \times 10^{58}$	$1.30 \times 10^{65}$	$2.92 \times 10^{67}$
3.19	0.125	$3.72 \times 10^{59}$	$7.41 \times 10^{65}$	$1.05 \times 10^{69}$	$1.17 \times 10^{70}$
3.28	0.066	$3.29 \times 10^{65}$	$6.97 \times 10^{68}$	$3.21 \times 10^{70}$	$1.15 \times 10^{71}$
3.47	0.013	$7.23 \times 10^{70}$	$3.27 \times 10^{71}$	$6.95 \times 10^{71}$	$8.94 \times 10^{71}$
3.70	0.009	$1.83 \times 10^{71}$	$5.20 \times 10^{71}$	$8.77 \times 10^{71}$	$1.04 \times 10^{72}$
3.94	0.008	$2.31 \times 10^{71}$	$5.84 \times 10^{71}$	$9.29 \times 10^{71}$	$1.08 \times 10^{72}$
4.18	0.080	$1.28 \times 10^{64}$	$1.37 \times 10^{68}$	$1.43 \times 10^{70}$	$6.70 \times 10^{70}$
4.43	0.138	$1.82 \times 10^{58}$	$1.64 \times 10^{65}$	$4.92 \times 10^{68}$	$7.10 \times 10^{69}$
4.71	0.182	$6.68 \times 10^{53}$	$9.94 \times 10^{62}$	$3.83 \times 10^{67}$	$1.30 \times 10^{69}$
5.17	0.240	$9.52 \times 10^{47}$	$1.19 \times 10^{60}$	$1.32 \times 10^{66}$	$1.37 \times 10^{68}$
5.85	0.245	$2.98 \times 10^{47}$	$6.64 \times 10^{59}$	$9.91 \times 10^{65}$	$1.13 \times 10^{68}$
6.29	0.240	$9.52 \times 10^{47}$	$1.19 \times 10^{60}$	$1.32 \times 10^{66}$	$1.37 \times 10^{68}$
6.74	0.240	$9.52 \times 10^{47}$	$1.19 \times 10^{60}$	$1.32 \times 10^{66}$	$1.37 \times 10^{68}$
7.19	0.240	$9.52 \times 10^{47}$	$1.19 \times 10^{60}$	$1.32 \times 10^{66}$	$1.37 \times 10^{68}$
7.64	0.240	$9.52 \times 10^{47}$	$1.19 \times 10^{60}$	$1.32 \times 10^{66}$	$1.37 \times 10^{68}$

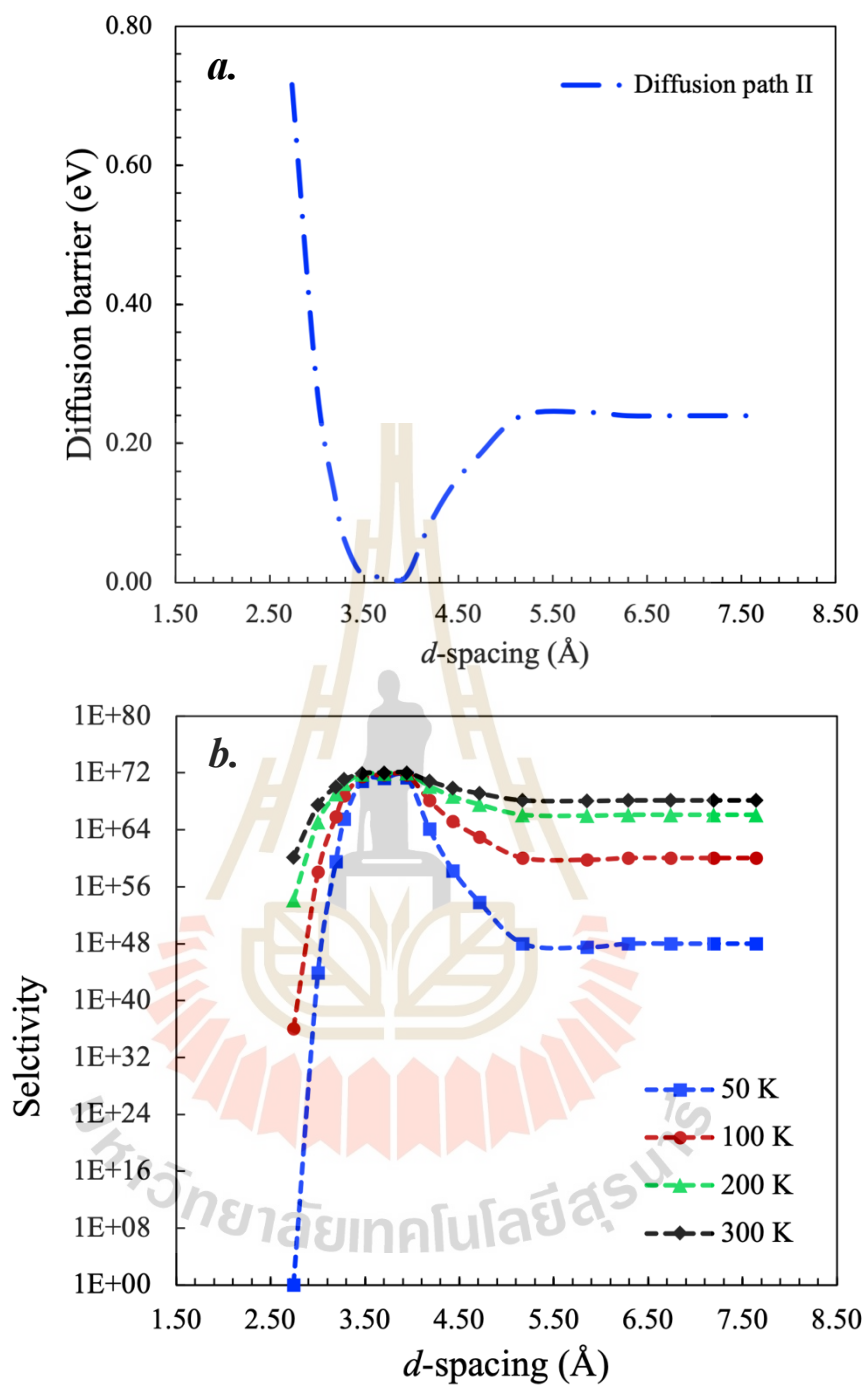


**Figure 7.12** The relation between (a) the diffusion barrier (eV) of diffusion path II and (b) the selectivity of Li-ion diffusion over the Li-adsorption site equilibrium state at 50 K in the bilayer as a function of  $d$ -spacing (Å).

### 7.2.4 Interlayer spacing induced by Co-intercalations of Li-ion in bilayer

#### Ti<sub>2</sub>CO<sub>2</sub>

The alkali metal intercalations, including Be, Mg, Ca, Na, and K alkali metals, as well as S atom intercalations, are addressed in the simulations. Therefore, the co-intercalation atoms are fully doped into the interlayer of the M'M'-M'M' combination structure with the s1 stacking configuration of the Ti<sub>2</sub>CO<sub>2</sub> bilayer (the X<sub>1,1,1</sub> model), approximately 10 percent doping (one atom in the unit cell). There are several positions to adsorb the considered co-intercalation atom; for this reason, one site that is energetically favorable among all the sites is chosen. Figure 7.13 includes the wider spacing induced by the co-intercalations, indicated in color lines with the plot of the diffusion barrier for diffusion paths I and II. In addition, light blue, yellow, green, violet, dark blue, and pink lines indicate the Be, Mg, Ca, Na, K, and S intercalations, respectively, which have the correspond value of interlayer spacing of 1.97, 2.33, 2.93, 2.99, 3.84, and 4.17 Å. We can assume that the K and S intercalation can enhance the interlayer spacing between approximately 3.40 Å and 4.10 Å in the near-zero energy barrier zone of the Li-ion diffusion.

Furthermore, the diffusion rate (and selectivity) of Li atom to that of the co-intercalation atom, including S and K, inserting into the X<sub>1,1,1</sub> model are compared. Like the previous result for the sake of simplicity, we also assumed the pre-factor as the similar values for all types of atomic diffusion. The comparison of the selectivity for the Li atom and the co-intercalation diffusion is also set relative to the  $k_{d, T=50K}^*$  value (equivalent to the previous result), which is examined by using equation 7.8 equations 2 and 3. In the ideal condition with maximize the capacitance of the Li atoms, we reduce the co-intercalation concentration by using a single atom of S and K for the 2x2x1 supercells, which can achieve around 2.5 percent doping. We discovered that fully doped K atoms cause a significant contraction of the interlayer spacing (around 3.84 Å with the 10 percent doping), which can rise to around 4.10 Å with the 2.5 percent doping. In addition, the *d*-spacing is increased from the fully doped of S atoms, about 4.20, to around 5.40 Å. From equation 2, since the rate of ionic diffusion inside the materials is diffusion barrier-dependent, the diffusion barriers of the Li atom along two diffusion paths (Path I and Path II) at the specific bilayer's *d*-spacing of 4.10 Å (for K co-

intercalation) and 5.40 Å (for S co-intercalation) were selected. As a results, Figures 7.14(a) and 7.14 (b) depict the temperature-dependent selectivity of the Li atom with K and S co-intercalations, respectively. The calculations used the diffusion barriers of the K co-intercalation atom's diffusion paths I and II of 0.550 and 0.542 eV, respectively, whereas the Li atom's diffusion barriers with equivalent  $d$ -spacing are 0.109 and 0.042 eV, respectively. The diffusion barrier of the S co-intercalation atom along diffusion paths I and II is 0.101 and 0.033 eV, respectively, while the diffusion barrier of the Li atom with the same  $d$ -spacing is 0.353 and 0.245 eV. Additionally, Table 7.7 contains the diffusion barrier used to compute the selectivity of the Li and K co-intercalation diffusion, while Table 7.8 shows the calculated information of the diffusion barrier and selectivity for the Li and S co-intercalation diffusion.

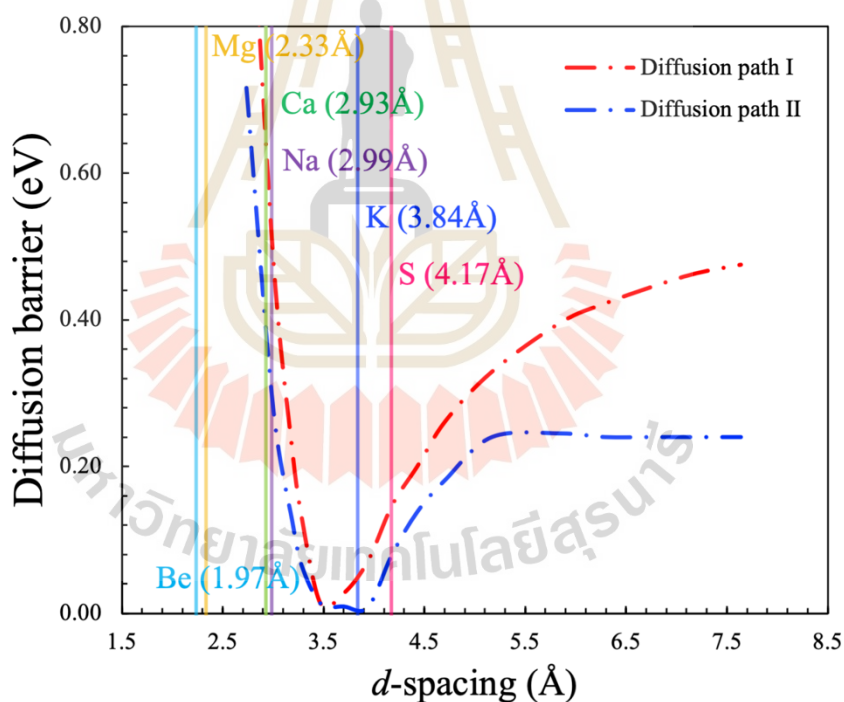


**Figure 7.13** The interlayer spacing induced by the various types of intercalations with the diffusion barrier of the diffusion path I and path II

**Table 7.7** Calculated diffusion barrier and Selectivity of Li and K co-intercalation atoms in bilayer  $Ti_2CO_2$ .

Type of diffusion atom	Diffusion barrier (eV)	Selectivity over temperatures						
		50 K	100 K	150 K	200 K	250 K	300 K	
Li	Diffusion path I	0.109	$1.53 \times 10^{61}$	$4.75 \times 10^{66}$	$3.22 \times 10^{68}$	$2.65 \times 10^{69}$	$9.39 \times 10^{69}$	$2.18 \times 10^{70}$
	Diffusion path II	0.042	$8.64 \times 10^{67}$	$1.13 \times 10^{70}$	$5.74 \times 10^{70}$	$1.29 \times 10^{71}$	$2.11 \times 10^{71}$	$2.91 \times 10^{71}$
K	Diffusion path I	0.550	$5.41 \times 10^{16}$	$2.83 \times 10^{44}$	$4.91 \times 10^{53}$	$2.05 \times 10^{58}$	$1.21 \times 10^{61}$	$8.52 \times 10^{62}$
	Diffusion path II	0.542	$3.43 \times 10^{17}$	$7.13 \times 10^{44}$	$9.09 \times 10^{53}$	$3.25 \times 10^{58}$	$1.75 \times 10^{61}$	$1.16 \times 10^{63}$

**Table 7.8** Calculated diffusion barrier and Selectivity of Li and S co-intercalation atoms in bilayer  $Ti_2CO_2$ .

Type of diffusion atom	Diffusion barrier (eV)	Selectivity over temperatures						
		50 K	100 K	150 K	200 K	250 K	300 K	
Li	Diffusion path I	0.353	$3.88 \times 10^{36}$	$2.40 \times 10^{54}$	$2.04 \times 10^{60}$	$1.88 \times 10^{63}$	$1.13 \times 10^{65}$	$1.74 \times 10^{66}$
	Diffusion path II	0.245	$2.99 \times 10^{47}$	$6.65 \times 10^{59}$	$8.68 \times 10^{63}$	$9.92 \times 10^{65}$	$1.70 \times 10^{67}$	$1.13 \times 10^{68}$
S	Diffusion path I	0.101	$9.65 \times 10^{61}$	$1.19 \times 10^{67}$	$5.96 \times 10^{68}$	$4.20 \times 10^{69}$	$1.36 \times 10^{70}$	$2.97 \times 10^{70}$
	Diffusion path II	0.033	$6.68 \times 10^{68}$	$3.14 \times 10^{70}$	$1.13 \times 10^{71}$	$2.16 \times 10^{71}$	$3.17 \times 10^{71}$	$4.10 \times 10^{71}$

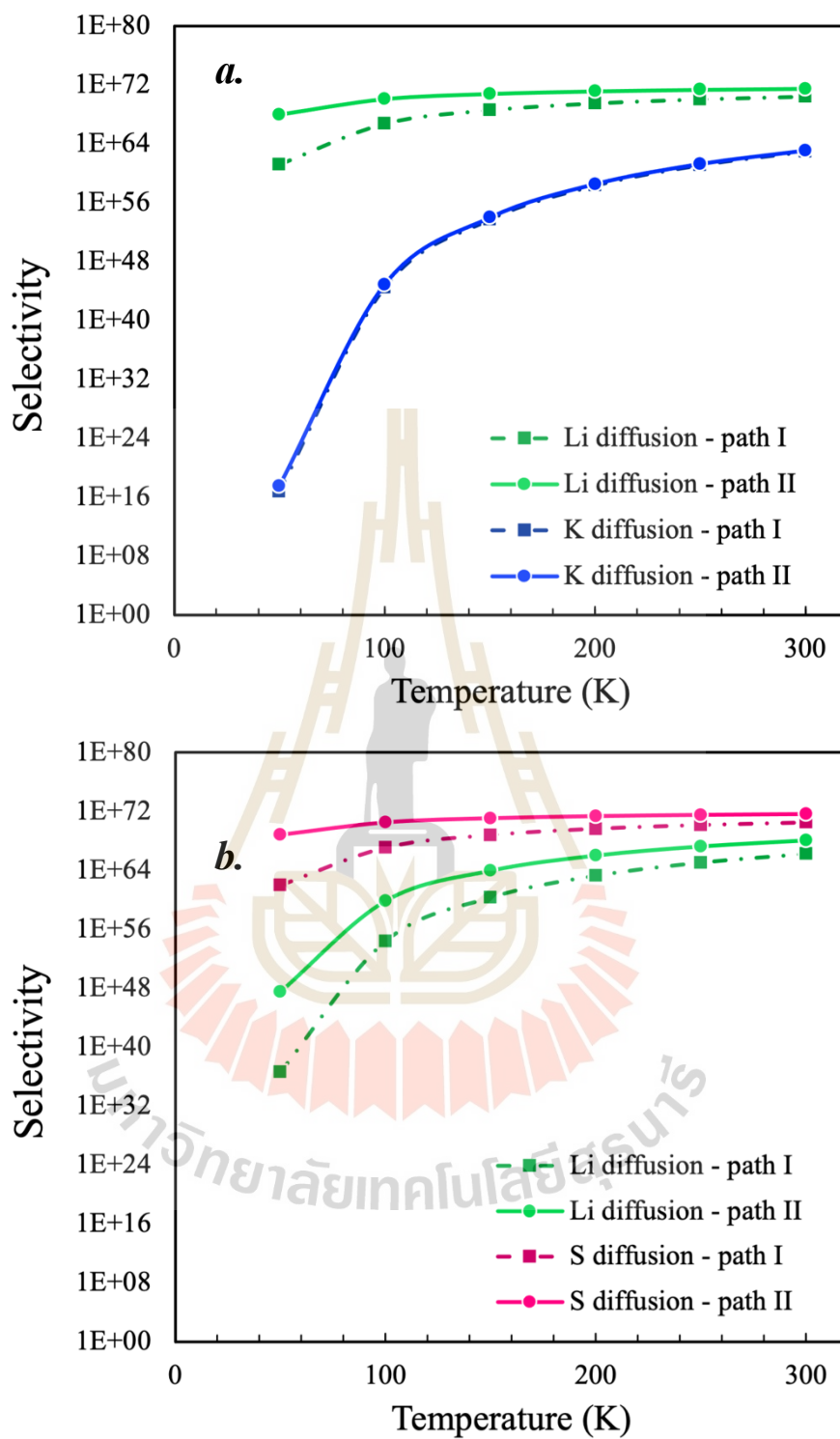


Figure 7.14 Selectivity of Li and the co-intercalation of (a) K atom and (b) S atom as a function of the temperatures.

At 50 K, the selectivity of Li ( $k_{d=4.10\text{\AA},T=50\text{K}}^{\text{Li}}/k^*$ ) and K ( $k_{d=4.10\text{\AA},T=50\text{K}}^{\text{K}}/k^*$ ) is over  $10^{61}$  and  $10^{16}$ , respectively, indicating an extremely high selectivity for Li in the interlayer spacing of around 4.10 Å, as shown in Figure 7.14(a). Additionally, the selectivity of the diffusion path II for the Li diffusion is around  $10^7$  orders of magnitude higher than that of the path I, whereas those for the K diffusion are roughly equal for both paths. As the temperature rises, the selectivity of the K ( $k_{d=4.10\text{\AA},T}^{\text{K}}/k^*$ ) increases faster than that of the Li ( $k_{d=4.10\text{\AA},T}^{\text{Li}}/k^*$ ). For a temperature of 300 K, our findings show that the selectivity of the Li ( $k_{d=4.10\text{\AA},T=300\text{K}}^{\text{Li}}/k^*$ ) is approximately  $10^8$  times higher than the selectivity of the K ( $k_{d=4.10\text{\AA},T=300\text{K}}^{\text{K}}/k^*$ ). According to the results, K co-intercalation not only promotes interlayer spacing along the length of the ultra-low diffusion barrier of the Li atom, but it also remains stationary during Li diffusion. However, Figure 7.14(b) shows that at 50 K, the selectivity of Li ( $k_{d=5.40\text{\AA},T=50\text{K}}^{\text{Li}}/k^*$ ) and S ( $k_{d=5.40\text{\AA},T=50\text{K}}^{\text{S}}/k^*$ ) is approximately  $10^{36}$  and  $10^{62}$  for diffusion path I, respectively, and  $10^{47}$  and  $10^{68}$  for diffusion path II. The S atom has a diffusion rate that is approximately 4–8 orders of magnitude greater than Li diffusion for each path at 300 K, indicating that S atom co-intercalation may not be proposed as the co-intercalation.

### 7.3 Discussion

Firstly, the  $M/M'$  model of  $\text{Ti}_2\text{CO}_2$  monolayer's adsorption energy, voltage calculations, and specific capacitance were performed. It is revealed that the highly probability for the adsorption coordinate of  $C_{ad1}$  and  $O_{ad2}$  is, respectively, the adsorption site for the 1<sup>st</sup> and 2<sup>nd</sup> Li-adsorption layer. The computations give an evaluated value of up to 500 mAh·g<sup>-1</sup> for the gravimetric capacitances, which corresponds to the OCV of 0.03 Volt (3 Li adatoms onto the unit cell). Furthermore, the framework for the LIB investigation of the  $\text{Ti}_2\text{CO}_2$  bilayer with the combined type of the  $M/M'-M/M'$  and the bilayer's  $s_1$  stacking configuration is described. We have provided the Li diffusion properties by using the static potential energy (SPES) and the climbing image nudged elastic band (CI-NEB) methods. For the SPES and CI-NEB methods, the calculated diffusion barriers are 0.223 eV and 0.215 eV, respectively. In the subsequence study, we chose the SPES method to simulate the trend for diffusion

barrier as the interlayer spacing changes. It turns out that we can get ultra-low diffusion barrier for the Li atom by using interlayer spacings between 0.34 and 4.10. The ultra-high Li-ion mobility inside the bilayer of the  $\text{Ti}_2\text{CO}_2$  structure, with a specific distance of the expanded interlayer spacing, is higher than that on the monolayer as presented in the literature. As a result, it is assumed that two of the  $\text{Ti}_2\text{CO}_2$  layers in the bilayer disregard the Li atom at the bilayer interface when the interlayer distance is appropriate. Besides this, we tested the interlayer length for the co-intercalation into the  $\text{Ti}_2\text{CO}_2$  bilayer where the Be, Mg, Ca, Na, K, Ca, and S had been chosen as the co-intercalation atoms. The interlayer spacing of the  $\text{Ti}_2\text{CO}_2$  bilayer can be adjusted to around 0.37 due to the K co-intercalation, enabling the ultra-low diffusion barrier. Our investigations are further expanded to the aspects of selectivity and diffusion rate, which can provide information about our potential in comparison to an experiment. Consequently, we determined that K co-intercalation is a promising candidate for enhancing the Li-ion diffusion characteristics because it promotes interlayer spacing into a length with an ultra-low diffusion barrier and would remain stationary throughout Li diffusion. Therefore, potassium co-intercalation may be used to improve the LIB application.



## CHAPTER VIII

### CONCLUSIONS AND FUTURE DIRECTION

#### 8.1 Conclusion

Thus far, this thesis has covered many aspects of the Ph.D. research. The entire study has been addressed, including the structural characteristics, electrical properties, applications for Li-ion batteries, and the selectivity of the Li-ion and the co-intercalation diffusion for the MXenes monolayer and bilayer. Firstly, we discovered that, despite having a similar structure,  $M_2CT_2$  exhibits different properties in different compounds in their family, such as the transition from semiconducting to conducting by changing the  $T$  and  $M$  elements. Likewise, the varied composition of the  $T$  inside the same compound's component may similarly display distinct electrical characteristics. For instance, various  $Sc_2CO_2$  monolayer structural models, such as the  $M'O$ ,  $OO$ , and  $MO$  models, display multiple band gaps, and some of which, such as the  $M'M'$ ,  $MM$ , and  $MM'$  models, show conducting behavior. In terms of structural stability, it can be assumed that the ionic states of the transition metals will have a significant impact on the relative structural stabilities of the  $M_2CT_2$  compounds. These have obviously been discovered based on estimates of formation energy and oxidation state. The most stable among  $M_2CO_2$  and  $M_2CF_2$  molecules are those with a balanced charge state, such as  $Ti_2CO_2$  and  $Sc_2CF_2$ . The types of structural models characterized by surface functional group compositions were given secondary precedence for stability, and the formation energy calculation reveals that the  $M'M'$  model has the highest stability among the monolayer models. Additionally, the majority of the  $M'M'$ ,  $M'O$ , and  $OO$  models for the  $M_2CT_2$  MXenes, respectively, reveal the most preferred structure according to the evaluation of the formation energy.

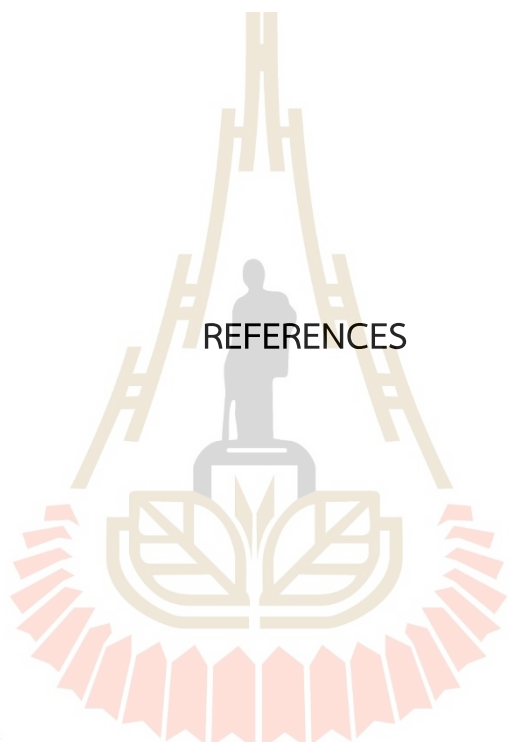
In the subsequent section, the characterization of the bilayer structures and their stability have been presented. Our discovery is a significant issue because of the bilayer's interface of the 3 different types for the combination types ( $AO-M'B$ ,  $AM'-M'B$ , and  $AO-OB$ ) which consist of exactly 18 forms of the stacking configurations

can be reduced to just 6 forms. We also infer that the stacking configurations can be transformed into one another by the given translation or rotation vectors. Furthermore, we use the DFT calculation to perform formation energy for every prospective structure. As a result, there is a distinct pattern in the apparent formation energy of the various bilayer's combined types for each compound. Our results demonstrate that as we switch the bilayer's combined type into other forms in each compound, the formation energy is shifted greater than that of the stacking configurations. However, the energy characteristic of the stacking configurations almost appears to be a particular pattern that identifies the  $s_1$  emerging as the most preferred configuration among all the combined types of the  $M_2CT_2$  bilayers. This study will draw attention to the fact that the properties of the  $M_2CT_2$  MXenes multilayer can be manipulated by regulating the structural arrangements in addition to the monolayer.

In the final part of the calculation, the framework for the LIB study of the  $Ti_2CO_2$  bilayer with the  $s_1$  stacking configuration of the  $M'M'-M'M'$  bilayer's combined type is explored. We used both the CI-NEB and SPES methods to simulate the diffusion barrier for the transition paths I and II. As a result, the computed diffusion barrier for the CI-NEB methods is 0.776 eV and 0.363 eV, for the transition paths I and II, respectively. The SPES approach is subsequently used to simulate the trend of the diffusion barrier for those two transition parts as a function of interlayer spacing ( $d$ -spacing). We discovered that interlayer spacings ranging from 0.34 Å to 4.10 Å allow us to achieve ultra-low diffusion barrier characteristics for the Li-ion mobility. Accordingly, the Li atom is interpreted as being neglected by both  $Ti_2CO_2$  layers at the bilayer interface when the interlayer distance is suitable. Interestingly, the potassium co-intercalation offers the opportunity to alter the  $Ti_2CO_2$  bilayer's interlayer spacing to about 0.37 Å, covering the ultra-low diffusion barrier characteristic and maintaining its position during Li diffusion. For this reason, in terms of enhancing the charging rate in the LIB application, potassium co-intercalation may be suggested.

## 8.2 Future direction

As previously mentioned, the  $M_2XT_2$  ( $M$  is Sc, Ti, V, Nb, and Cr;  $X$  is C;  $T$  is O and F) is one of the MXenes families ( $M_{n+1}C_nT_{n+1}$  where  $M$  is Sc, Ti, V, Nb, and Cr;  $X$  is C and N;  $T$  is O and F) used in the DFT calculations on the structural and electronic characteristics. Future study would have to include broadening the DTF calculations to analyze the electrical characteristics of the different  $n$  values ( $n > 1$ ) of the  $M_{n+1}C_nT_{n+1}$  compounds. Furthermore, in the investigation of LIB applications, only the bilayer of the  $Ti_2CO_2$  molecule with the most favored structure—the  $s_1$  stacking configuration of the  $M'M'-M'M'$  bilayer combination type—is used. We have given some interesting preliminary results on the  $Ti_2CO_2$  bilayer. One of the attractive issues might be the ultra-high Li-ion mobility inside the layered structure with a specific distance of expanding the interlayer spacing (higher than that on the monolayer) by utilizing the proper co-intercalation. However, an insightful explanation of our findings is still lacking. Thus, more DFT studies and more analysis methods to understand the electronic structure for the ultra-high Li-ion's mobility characteristic of the MXenes system will be very interesting topic. On the other hand, research into the diffusion properties of substances with favorable structures deviating from the simulation, such as  $Sc_2CO_2$  and  $Cr_2CO_2$ , is waiting to be simulated. In particular, the equilibrium structures for the compounds  $Sc_2CO_2$  and  $Cr_2CO_2$  are, respectively, the  $s_1$  stacking configuration of the  $OM'-M'O$  bilayer's combined type and the  $s_5$  stacking configuration of the  $OO-OO$  bilayer's combined type. Finally, the framework we have provided may be expanded to include additional alkali ion batteries, such Na and K ion batteries. That would also be a vast feature of future research.



REFERENCES

มหาวิทยาลัยเทคโนโลยีสุรนารี

## REFERENCES

- Alhabeab, M., Maleski, K., Anasori, B., Lelyukh, P., Clark, L., Sin, S. and Gogotsi, Y. (2017). Guidelines for Synthesis and Processing of Two-Dimensional Titanium Carbide ( $\text{Ti}_3\text{C}_2\text{Tx}$  MXene). *Chemistry of Materials* 29: 7633.
- Anasori, B., Lukatskaya, M. R. and Gogotsi, Y. (2017). 2D metal carbides and nitrides (MXenes) for energy storage. *Nature Reviews Materials* 2.
- Anasori, B., Xie, Y., Beidaghi, M., Lu, J., Hosler, B. C., Hultman, L., Kent, P. R. C., Gogotsi, Y. and Barsoum, M. W. (2015). Two-Dimensional, Ordered, Double Transition Metals Carbides (MXenes). *ACS Nano* 9: 9507.
- Ashton, M., Hennig, R. G. and Sinnott, S. B. (2016). Computational characterization of lightweight multilayer MXene Li-ion battery anodes. *Applied Physics Letters* 108: 023901.
- Bai, Y., Zhou, K., Srikanth, N., Pang, J. H. L., He, X. and Wang, R. (2016). Dependence of elastic and optical properties on surface terminated groups in two-dimensional MXene monolayers: a first-principles study. *RSC Advances* 6: 35731.
- Barsoum, M. W. and Radovic, M. (2011). Elastic and Mechanical Properties of the MAX Phases. *Annual Review of Materials Research* 41: 195.
- Becke, A. D. (1988). Density-functional exchange-energy approximation with correct asymptotic behavior. *Physical Review A* 38: 3098.
- Becke, A. D. (1993). A new mixing of Hartree-Fock and local density-functional theories. *The Journal of Chemical Physics* 98: 1372.
- Bertolazzi, S., Brivio, J. and Kis, A. (2011). Stretching and Breaking of Ultrathin  $\text{MoS}_2$ . *ACS Nano* 5: 9703.
- Birch, F. (1947). Finite Elastic Strain of Cubic Crystals. *Physical Review* 71: 809.
- Bloch, F. (1929). ber die Quantenmechanik der Elektronen in Kristallgittern. *Zeitschrift fr Physik* 52: 555.
- Blöchl, P. E. (1994). Projector augmented-wave method. *Physical Review B* 50: 17953.

- Blöchl, P. E., Jepsen, O. and Andersen, O. K. (1994). Improved tetrahedron method for Brillouin-zone integrations. *Physical Review B* 49: 16223.
- Born, M. and Oppenheimer, R. (1927). Zur Quantentheorie der Molekeln. *Annalen der Physik* 389: 457.
- Calais, J.-L. (1993). Density-functional theory of atoms and molecules. R.G. Parr and W. Yang, Oxford University Press, New York, Oxford, 1989. IX + 333 pp. Price £45.00.
- International Journal of Quantum Chemistry* 47: 101.
- Ceperley, D. M. and Alder, B. J. (1980). Ground State of the Electron Gas by a Stochastic Method. *Physical Review Letters* 45: 566.
- Chang, C.-H., Fan, X., Lin, S.-H. and Kuo, J.-L. (2013). Orbital analysis of electronic structure and phonon dispersion in MoS<sub>2</sub>, MoSe<sub>2</sub>, WS<sub>2</sub>, and WSe<sub>2</sub> monolayers under strain. *Physical Review B* 88.
- Desai, S. B., Seol, G., Kang, J. S., Fang, H., Battaglia, C., Kapadia, R., Ager, J. W., Guo, J. and Javey, A. (2014). Strain-induced indirect to direct bandgap transition in multilayer WSe<sub>2</sub>. *Nano Lett* 14: 4592.
- Dirac, P. A. M. and Fowler, R. H. (1926). On the theory of quantum mechanics. *Proceedings of the Royal Society of London. Series A, Containing Papers of a Mathematical and Physical Character* 112: 661.
- Eames, C. and Islam, M. S. (2014). Ion Intercalation into Two-Dimensional Transition-Metal Carbides: Global Screening for New High-Capacity Battery Materials. *Journal of the American Chemical Society* 136: 16270.
- Eknapakul, T., King, P. D. C., Asakawa, M., Buaphet, P., He, R. H., Mo, S. K., Takagi, H., Shen, K. M., Baumberger, F., Sasagawa, T., Jungthawan, S. and Meevasana, W. (2014). Electronic Structure of a Quasi-Freestanding MoS<sub>2</sub> Monolayer. *Nano Letters* 14: 1312.
- Fan, X., Chang, C. H., Zheng, W. T., Kuo, J.-L. and Singh, D. J. (2015). The Electronic Properties of Single-Layer and Multilayer MoS<sub>2</sub> under High Pressure. *The Journal of Physical Chemistry C* 119: 10189.
- Fu, Z., Wang, N., Legut, D., Si, C., Zhang, Q., Du, S., Germann, T. C., Francisco, J. S. and Zhang, R. (2019). Rational Design of Flexible Two-Dimensional MXenes with Multiple Functionalities. *Chemical Reviews* 119: 11980.

- Geim, A. K. and Novoselov, K. S. (2007). The rise of graphene. *Nature Materials* 6: 183.
- Ghidiu, M., Lukatskaya, M. R., Zhao, M.-Q., Gogotsi, Y. and Barsoum, M. W. (2014). Conductive two-dimensional titanium carbide 'clay' with high volumetric capacitance. *Nature* 516: 78.
- Ghidiu, M., Naguib, M., Shi, C., Mashtalir, O., Pan, L. M., Zhang, B., Yang, J., Gogotsi, Y., Billinge, S. J. L. and Barsoum, M. W. (2014). Synthesis and characterization of two-dimensional Nb<sub>4</sub>C<sub>3</sub> (MXene). *Chemical Communications* 50: 9517.
- Grimme, S. (2006). Semiempirical GGA-type density functional constructed with a long-range dispersion correction. *J Comput Chem* 27: 1787.
- Grimme, S., Antony, J., Ehrlich, S. and Krieg, H. (2010). A consistent and accurate ab initio parametrization of density functional dispersion correction (DFT-D) for the 94 elements H-Pu. *The Journal of Chemical Physics* 132: 154104.
- Guo, J., Sun, Y., Liu, B., Zhang, Q. and Peng, Q. (2017). Two-dimensional scandium-based carbides (MXene): Band gap modulation and optical properties. *Journal of Alloys and Compounds* 712: 752.
- Guo, Z., Zhou, J., Si, C. and Sun, Z. (2015). Flexible two-dimensional Tin+1C<sub>n</sub> (n = 1, 2 and 3) and their functionalized MXenes predicted by density functional theories. *Physical Chemistry Chemical Physics* 17: 15348.
- Hafner, J. (2008). Ab-initio simulations of materials using VASP: Density-functional theory and beyond. *J Comput Chem* 29: 2044.
- Halim, J., Lukatskaya, M. R., Cook, K. M., Lu, J., Smith, C. R., Näslund, L.-Å., May, S. J., Hultman, L., Gogotsi, Y., Eklund, P. and Barsoum, M. W. (2014). Transparent Conductive Two-Dimensional Titanium Carbide Epitaxial Thin Films. *Chemistry of Materials* 26: 2374.
- Heine, V. (1970) The Pseudopotential Concept. In *Solid State Physics, Vol. 24 (Eds, Ehrenreich, H., Seitz, F. and Turnbull, D.) Academic Press, pp. 1.*
- Hohenberg, P. and Kohn, W. (1964). Inhomogeneous Electron Gas. *Physical Review* 136: B864.
- Hope, M. A., Forse, A. C., Griffith, K. J., Lukatskaya, M. R., Ghidiu, M., Gogotsi, Y. and Grey, C. P. (2016). NMR reveals the surface functionalisation of Ti<sub>3</sub>C<sub>2</sub> MXene. *Physical Chemistry Chemical Physics* 18: 5099.

- Hu, J., Xu, B., Ouyang, C., Yang, S. A. and Yao, Y. (2014). Investigations on V2C and V2CX2 (X = F, OH) Monolayer as a Promising Anode Material for Li Ion Batteries from First-Principles Calculations. *The Journal of Physical Chemistry C* 118: 24274.
- Jindata, W., Hantanasirisakul, K., Eknapakul, T., Denlinger, J. D., Sangphet, S., Chaiyachad, S., Jaisuk, C., Rasritat, A., Sawasdee, T., Nakajima, H., Rattanachata, A., Fongkaew, I., Limpijumnong, S., Gogotsi, Y. and Meevasana, W. (2021). Spectroscopic signature of negative electronic compressibility from the Ti core-level of titanium carbonitride MXene. *Applied Physics Reviews* 8: 021401.
- Jing, Y., Zhou, Z., Cabrera, C. R. and Chen, Z. (2013). Metallic VS<sub>2</sub> Monolayer: A Promising 2D Anode Material for Lithium Ion Batteries. *The Journal of Physical Chemistry C* 117: 25409.
- Karlsson, L. H., Birch, J., Halim, J., Barsoum, M. W. and Persson, P. O. Å. (2015). Atomically Resolved Structural and Chemical Investigation of Single MXene Sheets. *Nano Letters* 15: 4955.
- Khazaei, M., Arai, M., Sasaki, T., Chung, C.-Y., Venkataramanan, N. S., Estili, M., Sakka, Y. and Kawazoe, Y. (2013). Novel Electronic and Magnetic Properties of Two-Dimensional Transition Metal Carbides and Nitrides. *Advanced Functional Materials* 23: 2185.
- Khazaei, M., Arai, M., Sasaki, T., Estili, M. and Sakka, Y. (2014). Two-dimensional molybdenum carbides: potential thermoelectric materials of the MXene family. *Physical Chemistry Chemical Physics* 16: 7841.
- Khazaei, M., Ranjbar, A., Arai, M., Sasaki, T. and Yunoki, S. (2017). Electronic properties and applications of MXenes: a theoretical review. *Journal of Materials Chemistry C* 5: 2488.
- Kittel, C. (1982). Introduction to Solid State Physics. United State of America: IncCambridge University.
- Kohn, W. and Sham, L. J. (1965). Self-Consistent Equations Including Exchange and Correlation Effects. *Physical Review* 140: A1133.
- Kresse, G. and Hafner, J. (1993). Ab initio molecular dynamics for liquid metals. *Physical Review B* 47: 558.

- Kresse, G. and Joubert, D. (1999). From ultrasoft pseudopotentials to the projector augmented-wave method. *Physical Review B* 59: 1758.
- Kuc, A., Zibouche, N. and Heine, T. (2011). Influence of quantum confinement on the electronic structure of the transition metal sulfide TS<sub>2</sub>. *Physical Review B* 83: 245213.
- Lashgari, H., Abolhassani, M. R., Boochani, A., Elahi, S. M. and Khodadadi, J. (2014). Electronic and optical properties of 2D graphene-like compounds titanium carbides and nitrides: DFT calculations. *Solid State Communications* 195: 61.
- Lee, Y., Cho, S. B. and Chung, Y.-C. (2014). Tunable Indirect to Direct Band Gap Transition of Monolayer Sc<sub>2</sub>CO<sub>2</sub> by the Strain Effect. *ACS Applied Materials & Interfaces* 6: 14724.
- Li, P., Zhu, J., Handoko, A. D., Zhang, R., Wang, H., Legut, D., Wen, X., Fu, Z., Seh, Z. W. and Zhang, Q. (2018). High-throughput theoretical optimization of the hydrogen evolution reaction on MXenes by transition metal modification. *Journal of Materials Chemistry A* 6: 4271.
- Lukatskaya, M. R., Kota, S., Lin, Z., Zhao, M.-Q., Shpigel, N., Levi, M. D., Halim, J., Taberna, P.-L., Barsoum, M. W., Simon, P. and Gogotsi, Y. (2017). Ultra-high-rate pseudocapacitive energy storage in two-dimensional transition metal carbides. *Nature Energy* 2.
- Lukatskaya, M. R., Mashtalir, O., Ren, C. E., Dall'Agnese, Y., Rozier, P., Taberna, P. L., Naguib, M., Simon, P., Barsoum, M. W. and Gogotsi, Y. (2013). Cation intercalation and high volumetric capacitance of two-dimensional titanium carbide. *Science* 341: 1502.
- Luo, J., Zhang, W., Yuan, H., Jin, C., Zhang, L., Huang, H., Liang, C., Xia, Y., Zhang, J., Gan, Y. and Tao, X. (2017). Pillared Structure Design of MXene with Ultralarge Interlayer Spacing for High-Performance Lithium-Ion Capacitors. *ACS Nano* 11: 2459.
- Mak, K. F., Lee, C., Hone, J., Shan, J. and Heinz, T. F. (2010). Atomically thin MoS<sub>2</sub>: a new direct-gap semiconductor. *Phys Rev Lett* 105: 136805.
- Martin, R. M. (2004). *Electronic Structure: Basic Theory and Practical Methods*. Cambridge: Cambridge University Press.

- Mashtalir, O., Lukatskaya, M. R., Zhao, M.-Q., Barsoum, M. W. and Gogotsi, Y. (2015). Amine-Assisted Delamination of Nb<sub>2</sub>C MXene for Li-Ion Energy Storage Devices. *Advanced Materials* 27: 3501.
- Mashtalir, O., Naguib, M., Mochalin, V. N., Dall'Agnese, Y., Heon, M., Barsoum, M. W. and Gogotsi, Y. (2013). Intercalation and delamination of layered carbides and carbonitrides. *Nature Communications* 4: 1716.
- Meng, Q., Hu, A., Zhi, C. and Fan, J. (2017). Theoretical prediction of MXene-like structured Ti<sub>3</sub>C<sub>4</sub> as a high capacity electrode material for Na ion batteries. *Physical Chemistry Chemical Physics* 19: 29106.
- Miao, N., Zhou, J., Sa, B., Xu, B. and Sun, Z. (2017). Few-layer arsenic trichalcogenides: Emerging two-dimensional semiconductors with tunable indirect-direct bandgaps. *Journal of Alloys and Compounds* 699: 554.
- Murnaghan, F. D. (1944). The Compressibility of Media under Extreme Pressures. *Proceedings of the National Academy of Sciences* 30: 244.
- Naguib, M., Come, J., Dyatkin, B., Presser, V., Taberna, P.-L., Simon, P., Barsoum, M. W. and Gogotsi, Y. (2012). MXene: a promising transition metal carbide anode for lithium-ion batteries. *Electrochemistry Communications* 16: 61.
- Naguib, M., Halim, J., Lu, J., Cook, K. M., Hultman, L., Gogotsi, Y. and Barsoum, M. W. (2013). New Two-Dimensional Niobium and Vanadium Carbides as Promising Materials for Li-Ion Batteries. *Journal of the American Chemical Society* 135: 15966.
- Naguib, M., Kurtoglu, M., Presser, V., Lu, J., Niu, J., Heon, M., Hultman, L., Gogotsi, Y. and Barsoum, M. W. (2011). Two-Dimensional Nanocrystals Produced by Exfoliation of Ti<sub>3</sub>AlC<sub>2</sub>. *Advanced Materials* 23: 4248.
- Naguib, M., Mashtalir, O., Carle, J., Presser, V., Lu, J., Hultman, L., Gogotsi, Y. and Barsoum, M. W. (2012). Two-Dimensional Transition Metal Carbides. *ACS Nano* 6: 1322.
- Naguib, M., Mochalin, V. N., Barsoum, M. W. and Gogotsi, Y. (2014). 25th Anniversary Article: MXenes: A New Family of Two-Dimensional Materials. *Advanced Materials* 26: 992.

- Naguib, M., Unocic, R. R., Armstrong, B. L. and Nanda, J. (2015). Large-scale delamination of multi-layers transition metal carbides and carbonitrides “MXenes”. *Dalton Transactions* 44: 9353.
- Novoselov, K. S., Geim, A. K., Morozov, S. V., Jiang, D., Zhang, Y., Dubonos, S. V., Grigorieva, I. V. and Firsov, A. A. (2004). Electric Field Effect in Atomically Thin Carbon Films. *Science* 306: 666.
- Novoselov, K. S., Jiang, D., Schedin, F., Booth, T. J., Khotkevich, V. V., Morozov, S. V. and Geim, A. K. (2005). Two-dimensional atomic crystals. *Proc Natl Acad Sci U S A* 102: 10451.
- Pauli, W. (1925). Über den Zusammenhang des Abschlusses der Elektronengruppen im Atom mit der Komplexstruktur der Spektren. *Zeitschrift für Physik* 31: 765.
- Peelaers, H. and Van de Walle, C. G. (2012). Effects of strain on band structure and effective masses in MoS<sub>2</sub>. *Physical Review B* 86.
- Peng, J., Chen, X., Ong, W.-J., Zhao, X. and Li, N. (2019). Surface and Heterointerface Engineering of 2D MXenes and Their Nanocomposites: Insights into Electro- and Photocatalysis. *Chem* 5: 18.
- Perdew, J. P., Burke, K. and Ernzerhof, M. (1996). Generalized Gradient Approximation Made Simple. *Physical Review Letters* 77: 3865.
- Perdew, J. P., Burke, K. and Ernzerhof, M. (1996). Generalized Gradient Approximation Made Simple. *Phys Rev Lett* 77: 3865.
- Perdew, J. P., Chevary, J. A., Vosko, S. H., Jackson, K. A., Pederson, M. R., Singh, D. J. and Fiolhais, C. (1992). Atoms, molecules, solids, and surfaces: Applications of the generalized gradient approximation for exchange and correlation. *Physical Review B* 46: 6671.
- Persson, I., Näslund, L.-Å., Halim, J., Barsoum, M. W., Darakchieva, V., Palisaitis, J., Rosen, J. and Persson, P. O. Å. (2017). On the organization and thermal behavior of functional groups on Ti<sub>3</sub>C<sub>2</sub> MXene surfaces in vacuum. *2D Materials* 5: 015002.
- Persson, I., Näslund, L.-Å., Halim, J., Barsoum, M. W., Darakchieva, V., Palisaitis, J., Rosen, J. and Persson, P. O. Å. (2017). On the organization and thermal behavior of functional groups on Ti<sub>3</sub>C<sub>2</sub> MXene surfaces in vacuum. *2D Materials* 5.
- Quester, W. (2006) Source [On-line] Available:

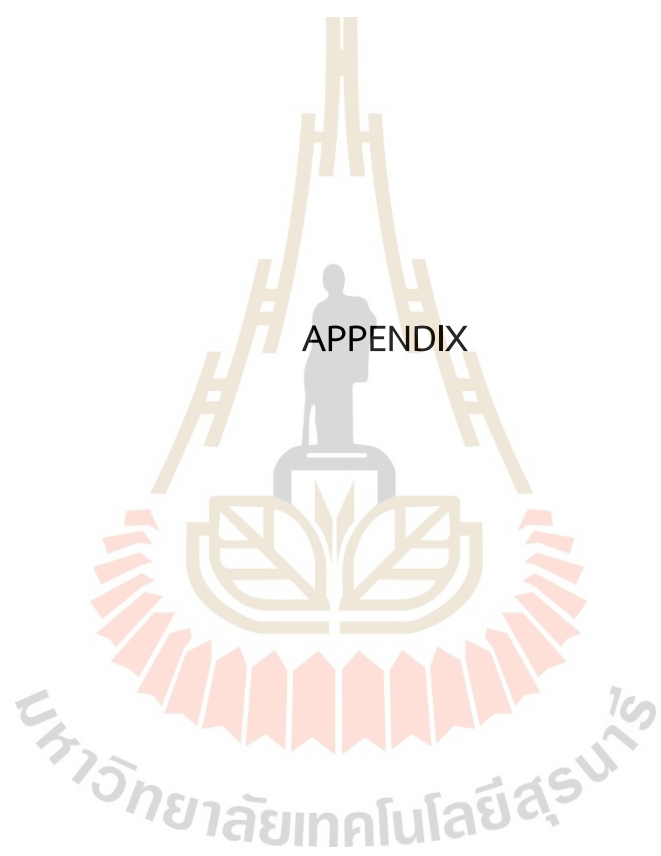
[https://en.wikipedia.org/wiki/Pseudopotential#/media/File:Sketch\\_Pseudopotentials.png](https://en.wikipedia.org/wiki/Pseudopotential#/media/File:Sketch_Pseudopotentials.png).

- Sakurai, J. J. (1994). Modern quantum mechanics (rev. ed.). *Addison-Wesley*.
- Schedin, F., Geim, A. K., Morozov, S. V., Hill, E. W., Blake, P., Katsnelson, M. I. and Novoselov, K. S. (2007). Detection of individual gas molecules adsorbed on graphene. *Nature Materials* 6: 652.
- Schrödinger, E. (1926). An Undulatory Theory of the Mechanics of Atoms and Molecules. *Physical Review* 28: 1049.
- Srivastava, P., Mishra, A., Mizuseki, H., Lee, K.-R. and Singh, A. K. (2016). Mechanistic Insight into the Chemical Exfoliation and Functionalization of Ti<sub>3</sub>C<sub>2</sub> MXene. *ACS Applied Materials & Interfaces* 8: 24256.
- Su, X., Zhang, R., Guo, C., Zheng, J. and Ren, Z. (2014). Band engineering of dichalcogenide MX<sub>2</sub> nanosheets (M = Mo, W and X = S, Se) by out-of-plane pressure. *Physics Letters A* 378: 745.
- Sun, S., Liao, C., Hafez, A. M., Zhu, H. and Wu, S. (2018). Two-dimensional MXenes for energy storage. *Chemical Engineering Journal* 338: 27.
- Tang, Q., Zhou, Z. and Shen, P. (2012). Are MXenes Promising Anode Materials for Li Ion Batteries? Computational Studies on Electronic Properties and Li Storage Capability of Ti<sub>3</sub>C<sub>2</sub> and Ti<sub>3</sub>C<sub>2</sub>X<sub>2</sub> (X = F, OH) Monolayer. *Journal of the American Chemical Society* 134: 16909.
- Tao, Q., Dahlqvist, M., Lu, J., Kota, S., Meshkian, R., Halim, J., Palisaitis, J., Hultman, L., Barsoum, M. W., Persson, P. O. Å. and Rosen, J. (2017). Two-dimensional Mo<sub>1.33</sub>C MXene with divacancy ordering prepared from parent 3D laminate with in-plane chemical ordering. *Nature Communications* 8: 14949.
- Van de Walle, C. G. and Neugebauer, J. (2004). First-principles calculations for defects and impurities: Applications to III-nitrides. *Journal of Applied Physics* 95: 3851.
- Vinet, P., Rose, J. H., Ferrante, J. and Smith, J. R. (1989). Universal features of the equation of state of solids. *Journal of Physics: Condensed Matter* 1: 1941.
- Vinet, P., Smith, J. R., Ferrante, J. and Rose, J. H. (1987). Temperature effects on the universal equation of state of solids. *Physical Review B* 35: 1945.

- Wang, H.-W., Naguib, M., Page, K., Wesolowski, D. J. and Gogotsi, Y. (2016). Resolving the Structure of  $Ti_3C_2Tx$  MXenes through Multilevel Structural Modeling of the Atomic Pair Distribution Function. *Chemistry of Materials* 28: 349.
- Wang, Q. H., Kalantar-Zadeh, K., Kis, A., Coleman, J. N. and Strano, M. S. (2012). Electronics and optoelectronics of two-dimensional transition metal dichalcogenides. *Nature Nanotechnology* 7: 699.
- Wang, X., Shen, X., Gao, Y., Wang, Z., Yu, R. and Chen, L. (2015). Atomic-Scale Recognition of Surface Structure and Intercalation Mechanism of  $Ti_3C_2X$ . *Journal of the American Chemical Society* 137: 2715.
- Wigner, E. (1934). On the Interaction of Electrons in Metals. *Physical Review* 46: 1002.
- Xie, Y., Naguib, M., Mochalin, V. N., Barsoum, M. W., Gogotsi, Y., Yu, X., Nam, K.-W., Yang, X.-Q., Kolesnikov, A. I. and Kent, P. R. C. (2014). Role of Surface Structure on Li-Ion Energy Storage Capacity of Two-Dimensional Transition-Metal Carbides. *Journal of the American Chemical Society* 136: 6385.
- Yarifard, M., Davoodi, J. and Rafii-Tabar, H. (2016). In-plane thermal conductivity of graphene nanomesh: A molecular dynamics study. *Computational Materials Science* 111: 247.
- Yoo, E., Kim, J., Hosono, E., Zhou, H.-s., Kudo, T. and Honma, I. (2008). Large Reversible Li Storage of Graphene Nanosheet Families for Use in Rechargeable Lithium Ion Batteries. *Nano Letters* 8: 2277.
- Zhang, H., Fu, Z., Zhang, R., Zhang, Q., Tian, H., Legut, D., Germann, T. C., Guo, Y., Du, S. and Francisco, J. S. (2017). Designing flexible 2D transition metal carbides with strain-controllable lithium storage. *Proceedings of the National Academy of Sciences* 114: E11082.
- Zhang, X., Ma, Z., Zhao, X., Tang, Q. and Zhou, Z. (2015). Computational studies on structural and electronic properties of functionalized MXene monolayers and nanotubes. *Journal of Materials Chemistry A* 3: 4960.
- Zhao, P., Desai, S., Tosun, M., Roy, T., Fang, H., Sachid, A., Amani, M., Hu, C. and Javey, A. (2015) 2D layered materials: From materials properties to device applications. *In 2015 IEEE International Electron Devices Meeting (IEDM)*, pp. 27.3.1.

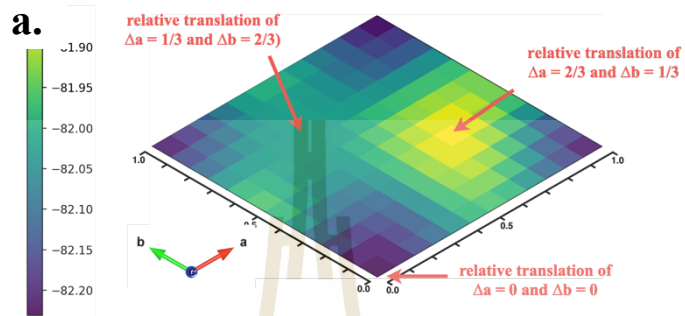
Zhao, S., Kang, W. and Xue, J. (2014). Manipulation of electronic and magnetic properties of M<sub>2</sub>C (M = Hf, Nb, Sc, Ta, Ti, V, Zr) monolayer by applying mechanical strains. *Applied Physics Letters* 104: 133106.



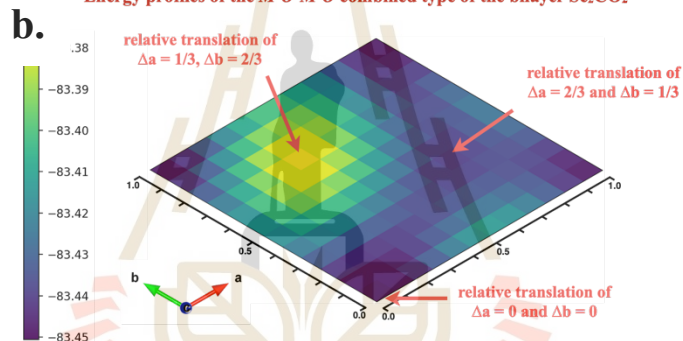


APPENDIX  
SUPPLEMENTARY INFORMATION

Energy profiles of the  $M'M'-M'M'$  combined type of the bilayer  $\text{Sc}_2\text{CO}_2$



Energy profiles of the  $M'O-M'O$  combined type of the bilayer  $\text{Sc}_2\text{CO}_2$



Energy profiles of the  $OO-OO$  combined type of the bilayer  $\text{Sc}_2\text{CO}_2$

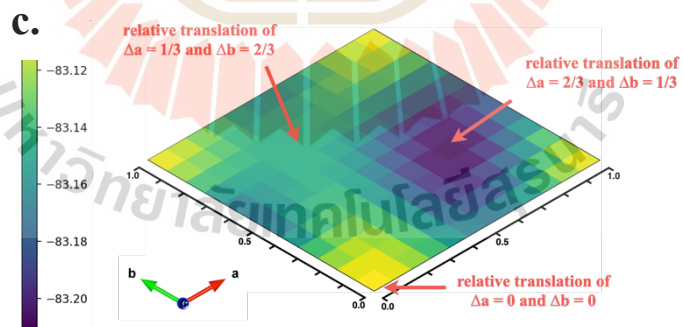
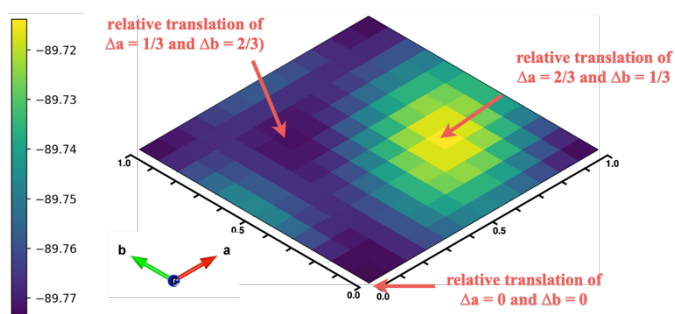
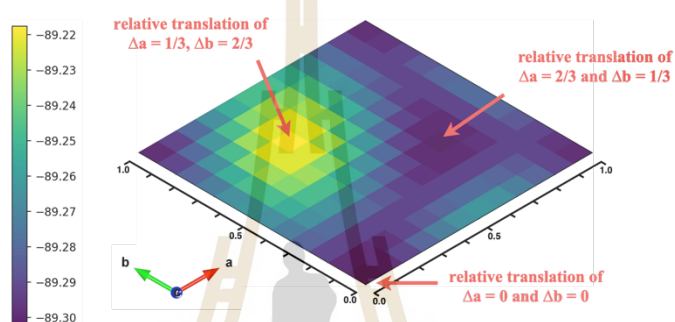


Figure S1 Energy profiles of the displacing top-layer along the fixed bottom-layer for the stacking configurations (a)  $M'M'-M'M'$ , (b)  $M'O-M'O$ , and (c)  $OO-OO$  of the  $\text{Sc}_2\text{CO}_2$  bilayer.

**a.** Energy profiles of the  $M'M'-M'M'$  combined type of the bilayer  $V_2CO_2$



**b.** Energy profiles of the  $M'O-M'O$  combined type of the bilayer  $V_2CO_2$



Energy profiles of the  $OO-OO$  combined type of the bilayer  $V_2CO_2$

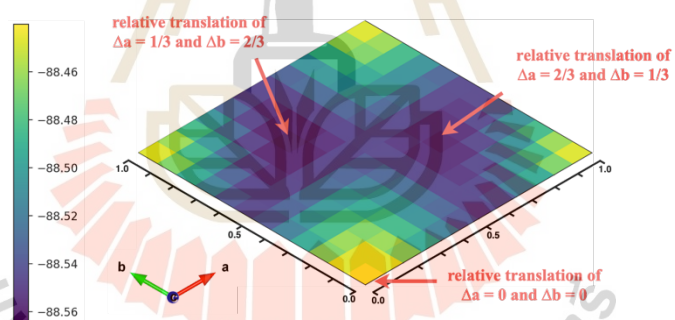


**Figure S2** Energy profiles of the displacing top-layer along the fixed bottom-layer for the stacking configurations (a)  $M'M'-M'M'$ , (b)  $M'O-M'O$ , and (c)  $OO-OO$  of the  $V_2CO_2$  bilayer.

## First Principles Study of Electronic Properties of $M_2CT_2$ ( $M = \text{Sc, Ti, V, Nb, Cr}$ and $T = \text{O, F}$ ) Transition Metal Carbides

Tanawat Sawasdee<sup>a,\*</sup>, Sirichok Jungthawan<sup>a, b, c</sup>

<sup>a</sup>School of Physics, Institute of Science, Suranaree University of Technology, Nakhon Ratchasima 30000, Thailand

<sup>b</sup>Center of Excellence in Advanced Functional Materials, Suranaree University of Technology, Nakhon Ratchasima, 30000, Thailand

<sup>c</sup>Thailand Center of Excellence in Physics, Ministry of Higher Education, Science, Research and Innovation, 328 Si Ayutthaya Road, Bangkok, 10400, Thailand

\*Corresponding Author's E-mail: swsdee5@gmail.com

### Abstract

Transition metal carbides have been widely studied in both theoretical and experimental research. It is well known that these materials have layered structure, excellent adsorption-desorption behavior and exhibit high electrical capacity. Normally, during synthesis, the layers are covered by surface functional groups such as O and F. However, the favorable adsorption site on the  $M_2CT_2$  (where  $M = \text{Sc, Ti, V, Nb, Cr}$  and  $T = \text{O, F}$ ) surface is still unclear. In this work, the structural and electronic properties of the  $M_2CT_2$  have been investigated by using first-principles calculations. There are three possible adsorbed sites of the  $T$  atom on each surface of  $M_2C$ -monolayer so called  $M$ ,  $M'$  and  $O$  sites, where the  $M$ ,  $M'$  and  $O$  site represent position that  $T$  atom is located above the  $M$  atom, hollow site, and the  $C$  atom, respectively. The adsorption site of the  $T$  atom on the surfaces, density of state (DOS), formation energy, and structural parameters for all configurations are discussed. In addition, six combinations of the adsorption sites based on the structural symmetry are introduced. It is found that the symmetric combination of the  $M'$  above and below  $M_2C$  layer, so called symmetric  $MM'$  model, tends to reduce the formation energy whereas the bond length between O- and F-M atom is comparable to their compound forms. The calculated DOS shows that the states of O  $2p$  and M  $3d$  orbitals of the  $MM'$  model have a tendency of the highly occupied states in lower energy region than the other models. This indicates that the formation energy of the  $MM'$  model is favorable among the studied configurations of the  $M_2CT_2$  compound.

**Keywords:** Density functional theory; 2D materials; Transition metal carbides

### Computational resources

- a. High Performance Computer Cluster (2.2 GHz, 504 CPUs), operating on Rocks Cluster, at SLRI
- b. Institute of Science (IOS) High-performance computer (HPC) at SUT
- c. Vienna *Ab-initio* Simulation Package (VASP) for first principles calculations at SUT and SLRI

### Locations of Research

- a. School of Physics, Institute of Science, Suranaree University of Technology, Nakhon Ratchasima, Thailand.
- b. Synchrotron Light Research Institute (SLRI), Nakhon Ratchasima, Thailand.



## CURRICULUM VITAE

NAME Mr. Tanawat Sawasdee  
PLACE OF BIRTH Mukdahan, Thailand  
PERSONAL ADDRESS 8/3 Khumsaithong vittaya Rd., Muang District,  
Mukdahan 49000, Thailand  
Mobile. +669 2949 6591  
E-MAIL [swsdee5@gmail.com](mailto:swsdee5@gmail.com)

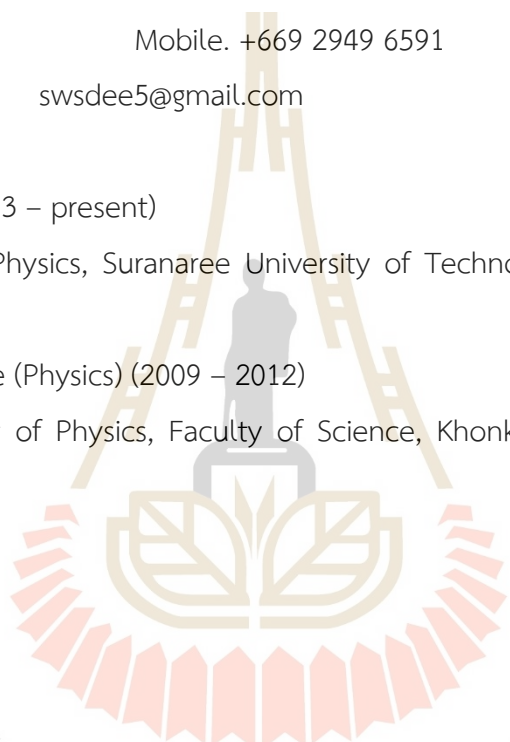
### EDUCATIONS

PhD candidate (2013 – present)

School of Physics, Suranaree University of Technology, Nakhon Ratchasima,  
Thailand.

Bachelor of Science (Physics) (2009 – 2012)

Department of Physics, Faculty of Science, Khonkaen University, Khonkaen,  
Thailand.



มหาวิทยาลัยเทคโนโลยีสุรนารี